THE UNIVERSITY *of* EDINBURGH

MERGING, SPREADING AND JUMPING NANODROPLETS

Sree Hari Perumanath Dharmapalan

Doctor of Philosophy

THE UNIVERSITY OF EDINBURGH

17 March 2020

Dedicated to Jason M. Reese

Lay Summary

Tiny ripples exist on any liquid surface, but we cannot see them with our naked eyes. These ripples, or waves, are 1 million times smaller than the width of a human hair and arise due to the constant bombarding of molecules with each other. The most advanced experimental techniques are still not able to resolve these molecular waves, which is why this thesis uses very detailed molecular simulations to study them and understand their impact on a few engineering flow problems. In particular, this thesis focuses on the influence of these waves when nanoscale droplets (a) merge with each other, (b) spread on a surface and (c) merge and lift-off from a surface. Merger and spreading of droplets are ubiquitous in our daily lives: mixing of sauces during cooking, spreading of cleaning liquids on various surfaces, merging of ink droplets inside printers and spreading of the resulting coloured ink on papers. Formation of clouds and rain also relies on droplets forming and merging. Molecular simulations in this thesis show, for the first time, that during droplet merging, these tiny waves reach out across these droplets to initiate the first contact between them. Right after this, the surfaces of the droplets get stuck onto each other and continue to merge in a newly discovered behaviour that is best explained like how one zips both sides of a jacket after putting it on. This will go on along with a few other well-known processes, which will later lead to the complete merger of the droplets. A similar 'zipping' process is also observed when a droplet impacts and spreads on a surface. However, on repelling surfaces, droplets will avoid spreading and adopt a perfectly spherical shape, just like rain droplets that rest on a lotus leaf. When two such neighbouring droplets merge, the final droplet will spontaneously lift-off from the surface. This jumping process requires no external intervention and can be used to self-activate cleaning on surfaces, transfer heat in cooling devices and has the potential to inhibit ice formation. In this thesis, these tiny ripples on nanodroplet surfaces have also shown that they can enable the lift off of the smallest possible droplets from a surface at various speeds. Moreover, the drag caused from the nanodroplets' surroundings as they merge and lift-off is found to behave in an unusual way. Such improved understanding about these processes at a fundamental molecular level will enable us to design next-generation nano/micro devices and understand processes that manipulate and leverage droplets in various engineering applications.

Abstract

Droplet-based systems appear in various aspects of our daily lives: in understanding the process of atmospheric storm cloud formation – involving very large length and time scales; in determining the shelf life of emulsion-based products such as mayonnaise – involving intermediate scales; and in design and optimization of next-generation micro/nano-fluidic devices such as nanopipe cooling materials – operating at much smaller scales. There are clear differences in the dominant physics that underpins their functioning, when these systems scale from macro to nano. As a result, many of the experimental observations at micro/nano-scales are often counter-intuitive and fascinating. Some such examples relevant to future nano-engineered technologies include: order of magnitudes higher water flow rate through nanotubes than predicted by traditional theories, passive water droplet transport to hotter regions on a heated surface and faster evaporation rates from nanoscale menisci. In this thesis, unconventionally large and computationally expensive molecular dynamics simulations are used to study problems involving nanodroplets, which have a wide range of engineering applications. The novelty in this work includes: (a) the investigation of previously unexplored realms of nanoscale interfacial fluid flows using high-fidelity molecular simulations and (b) uncovering the theoretical and fundamental explanation of how molecular motion affects the nanodroplet dynamics of three problems: merging, spreading and jumping nanodroplets.

In the first problem, coalescence of two water droplets is studied, focusing on the first contact and growth of the bridge that connects both droplets. Many mathematical models in the literature host a 'singularity' in the beginning of coalescence, where calculated quantities like velocity and pressure diverge at this point. Such singularities are unphysical, and what happens in reality is investigated in more detail in this thesis. The thermal motion of constituent molecules is found to have substantial impact not only in initiating coalescence, but also in developing the liquid bridge in the initial stages. For large droplets, a hydrodynamic instability develops owing to the attraction between confronting interfaces of the droplets as they approach each other. However, no evidence of such instability is observed at the nanoscale. Instead, the first contact happens because of the interfacial thermal fluctuations on droplets' surfaces meeting from opposite sides. Thereafter, coalescence proceeds in an observed 'thermal regime', where, as molecular simulations show, the bridge grows as a result of gradual cohesion of the confronting interfaces of the droplets due to collective molecular jumps. This continues until a 'thermal length scale' is achieved, which is found to scale as square-root of the size of the coalescing droplets. Only after these molecular-driven processes finish does the bridge evolve in the manner that we had previously understood.

The relevance of the observed molecular thermal motion on droplet-droplet interactions is

tested on droplet-surface interactions and found to extend also to these problems with small variations in the observed physics. When a liquid wets a solid surface, which is essential for applications in coating technologies, agriculture and printing, to name a few, a regime of contact line motion, which is very similar to the thermal regime in coalescence, is found to precede the contact line motion that we have traditional understood. The extent of this regime not only scales as square-root of the droplet size, but also depends on the attraction from the underlying wall. The dependence of this length scale on the equilibrium contact angle is explained based on the local profile of the droplet near the wall when the first contact happens. In this 'thermal-vdW regime', the interfacial molecules of the droplet get deposited directly on to the surface, before it gives way to the traditional picture of contact line motion, where the molecules at the three-phase-zone hop over the potential energy landscape above the wall atoms. The existence of this new regime of droplet wetting on atomically smooth surfaces is further validated by comparison of the contact line motion with what is described by the molecular kinetic theory, with which the late stage dynamics closely match.

The third problem combines the droplet-droplet and droplet-surface interactions and investigates the molecular physics of coalescence-induced jumping of nanodroplets from non-wetting surfaces, which is relevant for heat transfer and self-cleaning applications. Here, the effect of molecular thermal motion and ambient gas rarefaction on the jumping speed of a droplet is investigated. While the presence of an outer gas reduces the jumping speed by introducing an additional dissipation mechanism into the system, the interfacial thermal fluctuations make the jumping of nanodroplets a stochastic process. An analytical model of drag from outer gas is developed explaining the reduction of the jumping speed with respect to that in near-vacuum conditions. The thermal-capillary waves on the droplet surface renders the jumping speed to be statistically distributed with smaller droplets having wider and skewed distributions. It is shown that the jumping dynamics of nanodroplets is governed not just by Ohnesorge number as previously thought, but also by Knudsen number and thermal fluctuation number.

Despite their increased importance at the nanoscale, this is the first time that the effect of thermal capillary waves is properly quantified in studies concerning the dynamics of nanodroplets. Moreover, this thesis is intended to inspire the reader to look at many other traditional problems with singularities from a fundamental molecular perspective. It may be the case that the thermal regime of droplet coalescence and the thermal-vdW regime of droplet spreading are two special classes of a larger set of interface evolution dynamics and this requires further systematic molecular investigations and quantifications. Furthermore, the models developed in this thesis can be integrated in CFD simulations in the future as better initial/boundary conditions. Coupled with insights from the theoretical analyses presented throughout this thesis, the results can be used to study many natural systems and to predict performance characteristics of futuristic micro/nano-fluidic devices, which employ nanodroplets for heat-transfer and various other emerging technologies such as self-cleaning and anti-icing surfaces.

Acknowledgements

Firstly, I wish to thank my supervisor Dr Matthew K. Borg for providing me with constant motivation to improve my skill sets, valuable guidance to expand my knowledge base and for occasional laughter-filled chit-chats. Matthew has been a incredible mentor to me with abundant patience, especially in listening to stacks of my ideas and work plans.

I take this opportunity to thank late Prof Jason M. Reese for offering me this PhD studentship and inviting me to be a part of his research group at Edinburgh. Apart from numerous guidances that I have received from him – both academic and social, and invaluable opportunities to interact with countless experts in fluid dynamics, Jason will be remembered for his enthusiastic approach to life and, above all, his joviality.

I would like to thank Dr Rohit Pillai for taking over Jason's role as my second supervisor in a difficult time for all of us. I would also like to thank Dr Livio Gibelli, Dr James E. Sprittles, Dr Mykyta V. Chubynsky and Dr Ryan Enright for useful discussions.

I wish to thank other PhD students and post-doctoral fellows within our group for useful discussions, help and numerous chats over lunch. Particularly, I would like to thank Duncan, Jun, Wenjing and Jianfei for playing badminton with me every week.

Special thanks to my examiners Dr Paola Carbone and Dr Timm Krüger for their valuable time and detailed critique of my thesis, which has significantly helped improve this work.

Finally, I wish to thank my parents, sister, her husband and Sreekuttan & Malu for always being there for me. I wish to thank all my friends for making Edinburgh a home away from home for me. Thank you Parizad and Shivangi for all the silly talks, frequent cooking-together's, occasional drinks and night-outs, movie nights and for many leisurely trips to the Scottish highlands. This would not have been possible without you!

Sree Hari P. D.
Edinburgh, Scotland, UK
17 March 2020

Declaration

I declare that the thesis has been composed by myself and that the work has not been submitted for any other degree or professional qualification. I confirm that the work submitted is my own, except where work which has formed part of jointly-authored publications has been included. My contribution and those of the other authors to this work have been explicitly indicated below. I confirm that appropriate credit has been given within this thesis where reference has been made to the work of others.

The majority of the work presented in Chapter 3 is already published in *Physical Review Letters* as *Droplet coalescence is initiated by thermal motion* by *Perumanath, S.*,[1] *Borg, M. K.*,[2] *Chubynsky, M. V., Sprittles, J. E., and Reese, J. M.* This study was conceived by me and I carried out the simulation, majority of the analysis and drafting.

Sree Hari Perumanath Dharmapalan
17 March 2020

1. Student and the author of declaration
2. Supervisor

Contents

List of Figures

List of Symbols

x, y, z	positions
v	velocity
a	acceleration
t	time
t_0	time at which coalescence/spreading began
F, f	force
m	atomic mass
τ_v	viscous-capillary time scale
τ_i	inertial-capillary time scale
r_b	bridge radius during coalescence
R	coalescence radius of the droplet
h	half the distance between two far ends of the coalescing droplets
γ	liquid/vapour interfacial tension
γ_{sl}	solid/liquid interfacial tension
γ_{sv}	solid/vapour interfacial tension
ρ	density of the fluid
μ	fluid viscosity
C_i, C_i'	proportionality constant in the inertial regime
C_v	proportionality constant in the viscous regime
Re	Reynolds number
Oh	Ohnesorge number
A_H	Hamaker constant
Δ	gap width between approaching droplets
σ	length parameter in LJ potential
ε	energy parameter in LJ potential
r	distance between interacting atoms, contact line location (Chapter 4)
U, $\forall$	potential energy function
r_c	cut-off distance
d_{skin}	skin distance
N	total number of atoms, instantaneous number of interfacial molecules (Chapter 3)
T	absolute temperature
k_B	Boltzmann constant
r_c	cut-off distance
P, p_∞	pressure
$P_{N/T}$	normal/tangential stress tensor

V	volume
$L_{x/y/z}$	length of the simulation box in $x/y/z$ directions
D	diffusion coefficient
d_k	Coulomb cut-off above which PPPM method is used
n	number of neighbours
n_v	number density of the liquid
λ_T	coupling parameter for Berendsen thermostat
T_0	target temperature
τ_{xy}	shear stress on a plane normal to x in the y direction
θ_c	equilibrium contact angle
θ_d	(instantaneous) dynamic contact angle
V_r	relative velocity of approach of droplets
l_c	length scale within which coalescence can begin
l_T	thermal length scale
v_b	speed of bridge growth during coalescence
N_0	Initial number of interfacial molecules
A	surface area of a droplet
n_A	number of interfacial molecules per unit area
ΔZ	length of a bridge front
λ	mean-free-path of gas molecules, equilibrium jump distance (Chapter 4)
κ_0	equilibrium jump frequency
r_0	location of the projection of centre-of-mass of the droplet on the wall
V_{CL}	contact line velocity
H	half the distance between approaching interfaces
$\sigma_{\max}$	maximum growth rate of the available wave numbers
$y_{\min}$	location of the point closest to the wall among the equimolar points
l_γ	capillary length
U	inertial-capillary velocity scale
m_d	mass of a single droplet
W_{adh}	work of adhesion
W_{drag}	work done against drag force
c_p	specific heat capacity
Kn	Knudsen number
V_v	droplet jumping speed in vacuum
V_g	droplet jumping speed in the presence of a gas
T_v	overall temperature of the droplet in vacuum
T_g	overall temperature of the droplet in the presence of a gas
$q,\ \phi,\ \psi$	correction factors
β	thermal fluctuation number

Chapter 1

Introduction

Water vapour in the atmosphere condensing on microscopic dirt, salt or clay particles results in the formation of droplets that ultimately form a storm cloud. These droplets, which are in constant motion in the turbulent atmospheric air, bombard into each other before eventually showering on the earth below (Kovetz and Olund, 1969). This involves collision of droplets in intense vortical structures (Agasthya *et al.*, 2019); many of them leads to droplet coalescence. Such collision and coalescence processes are crucial to trigger rain, since small water nuclei in warm clouds must aggregate to a minimum size before gravity can bring them down.

Dynamical processes involving droplets find many other fascinating applications. Boreyko and Chen (2009) reported experimental observations of *coalescence-induced jumping* of water droplets from ultra-low adhesion surfaces. Droplets tend to retain spherical shape on such surfaces, and when they coalesce with their neighbours, the final droplet lifts-off without any external force. Insects like cicada use this mechanism to self-clean their wings (Wisdom *et al.*, 2013); the wings are composed of hierarchical structures equipping them with ultra-low adhesion properties. Geckos use this phenomenon to remove dew droplets from their skins (Watson *et al.*, 2011). This has inspired engineers to design similar surfaces, but for widely different applications (Boreyko *et al.*, 2011; Zhang *et al.*, 2013; Miljkovic *et al.*, 2013).

Droplet-surface interactions find numerous other interesting applications. For example, many insects use attachment pads to adhere to exceptionally smooth surfaces (Bohn and Federle, 2004; Qian and Gao, 2006). *Gromphadorhina portentosa*, commonly known as the Madagascan hissing cockroach, secrete a special fluid from the pre-tarsal glands near their feet, which spontaneously spreads on surfaces giving the insects firm adhesion as well as fair mobility (van Casteren and Codd, 2010).

Droplet dynamics dictate the working and performance of many other natural and industrial processes: spreading of pesticides on plant leaves (Xu *et al.*, 2011), mixing of medicines in pharmaceutics (Komatsu *et al.*, 1997), determining shelf life of emulsion-based products, such as mayonnaise (Kumar *et al.*, 1996), heat transfer applications (Rose, 1967; O'neill and Westwater, 1984), droplet transport (Zimmerli *et al.*, 2005; Qin *et al.*, 2011), anti-icing surfaces (Boreyko and Collier, 2013; Zhang *et al.*, 2013), thermal diodes (Boreyko *et al.*, 2011), metal nanoparticle formation (Boneberg *et al.*, 2008) and energy harvesting (Miljkovic *et al.*, 2014).

1.1 Background

Inspired from the vast number of natural and engineering applications of droplet-based systems in our daily lives, the theme of this thesis is on dynamical problems associated with droplet-droplet and droplet-surface interactions – particularly, droplet coalescence, spreading and jumping. The thesis primarily looks into these processes from a fundamental molecular perspective with the main aim to study the influence of molecular effects such as thermal motion on droplet dynamics and to observe and quantify how such nanoscale effects manifest themselves at much larger length scales. In the process, the influence of other non-continuum effects such as the atomic structure of solid substrate and extreme gas rarefaction are also investigated. While researchers have briefly studied some of these problems using different techniques, a full molecular picture of these processes is lacking in the literature. Nevertheless, before proceeding to the contribution of this thesis to the scientific literature, it is necessary to have a sense of where our current understanding stands today.

1.1.1 First contact between droplets during coalescence

In a system at a finite temperature, the constituent particles will always be in Brownian motion, with particles frequently bombarding with their neighbours. Due to this thermal agitation of the constituent molecules, any interface between two phases, be it solid/liquid, liquid/liquid, liquid/gas or solid/gas, will have a 'dynamic roughness' associated with it (v. Smoluchowski, 1908) and its characteristics will depend on temperature, interfacial tension, geometry and other system parameters (Rowlinson and Widom, 1982). Consequently, the shape of any interface is assumed to comprise a mean/nominal profile and a fluctuating part that arises due to thermal fluctuations — for example, a free droplet will have a spherical mean profile with fluctuations imposed on top of it.

A liquid/vapour interface resolved at a molecular scale will have molecules in a constant thermal motion, the speed of which is determined by the temperature of the system. At any instant, several molecules at the interface may have a non-zero component of their thermal velocity in the direction normal to the interface. As a result, these interfacial molecules will try to move away from the interface (see Fig. 1.1(a)). Since any deviation from the nominal profile will result in an increase in the interfacial area, the interfacial tension (γ) will act to bring these molecules back to their original location, thereby trying to reduce the overall exposed area (see Fig. 1.1(b)). The two processes of thermal jumps and interfacial tension pull-back occur at all interfacial locations, and are the underlying mechanisms that give interfaces their molecular roughness. Since the thermal energy of molecules is balanced by the capillary energy of the interface, these fluctuations are called *thermal capillary waves*, and they have been experimentally observed (Aarts *et al.*, 2004; Hennequin *et al.*, 2006).

Traditionally, the problem of droplet coalescence is approached as two different — and independent — sub-problems. In the first one, the mechanism of the establishment of the first

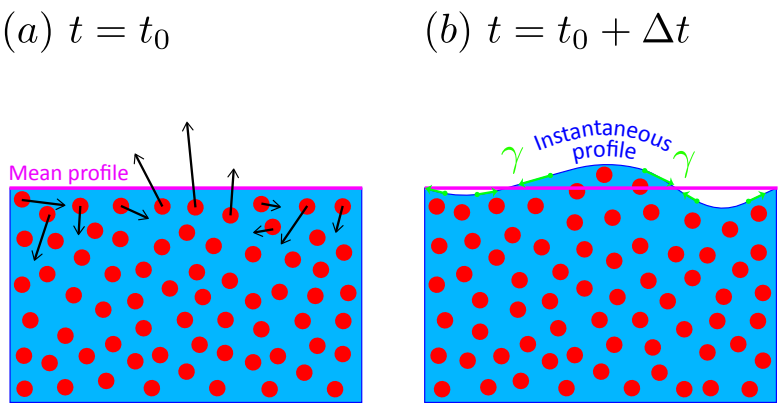

Figure 1.1: The mechanisms which generate interfacial thermal fluctuations. (a) Some molecules near the interface may have a component of their thermal velocities oriented normal to the mean profile. (b) interfacial tension (γ) tries to minimise the deviation of the instantaneous profile due to thermal fluctuations from the mean profile.

contact between the droplets is described by an interplay of (a) hydrodynamic drainage of the intervening fluid and (b) competitive action between surface thermal fluctuations and van der Waals interactions. In the second one, which studies the subsequent evolution of this connection between the droplets using traditional hydrodynamics, the influence of thermal fluctuations and van der Waals interactions are suddenly neglected.

When two droplets approach each other prior to coalescence, the intervening fluid between them will get displaced. This will continue until a thin film remains (see Fig. 1.2(a,b)), whose stability and life-time have been subjected to theoretical (Vrij, 1966; Vrij and Overbeek, 1968; Prevost and Gallez, 1986) and experimental studies (Chen *et al.*, 2004; Manor *et al.*, 2008; Vakarelski *et al.*, 2010; Chireux *et al.*, 2018). While the initial stages of fluid displacement only involve the hydrodynamic drainage, the effect of attraction/repulsion between confronting interfaces must be incorporated into the analysis as the thickness of the film approaches a few 100 nanometres or below; van der Waals attraction increases the drainage and double layer repulsion decreases it. Dominant repulsive interactions between confronting interfaces stabilizes the intervening film. During thinning, some films will reach a metastable state where opposing forces equilibrate. Instability only occurs when attractive interactions dominate.

Vrij (1966) studied the stability of a free, thin liquid film subjected to spontaneous fluctuations in its thickness. While fluctuations due to bending of the film as a whole is shown to be stabilizing under all conditions, instability can arise due to a competition between increases in the Gibbs free energy (G) (owing to increases in interfacial area) and changes in G (owing to thinning of the film). The drainage of the film during thinning is studied by assuming the intervening film is composed of a liquid of thickness-independent viscosity. If the surface perturbations are assumed to be composed of numerous Fourier modes, a critical wavelength

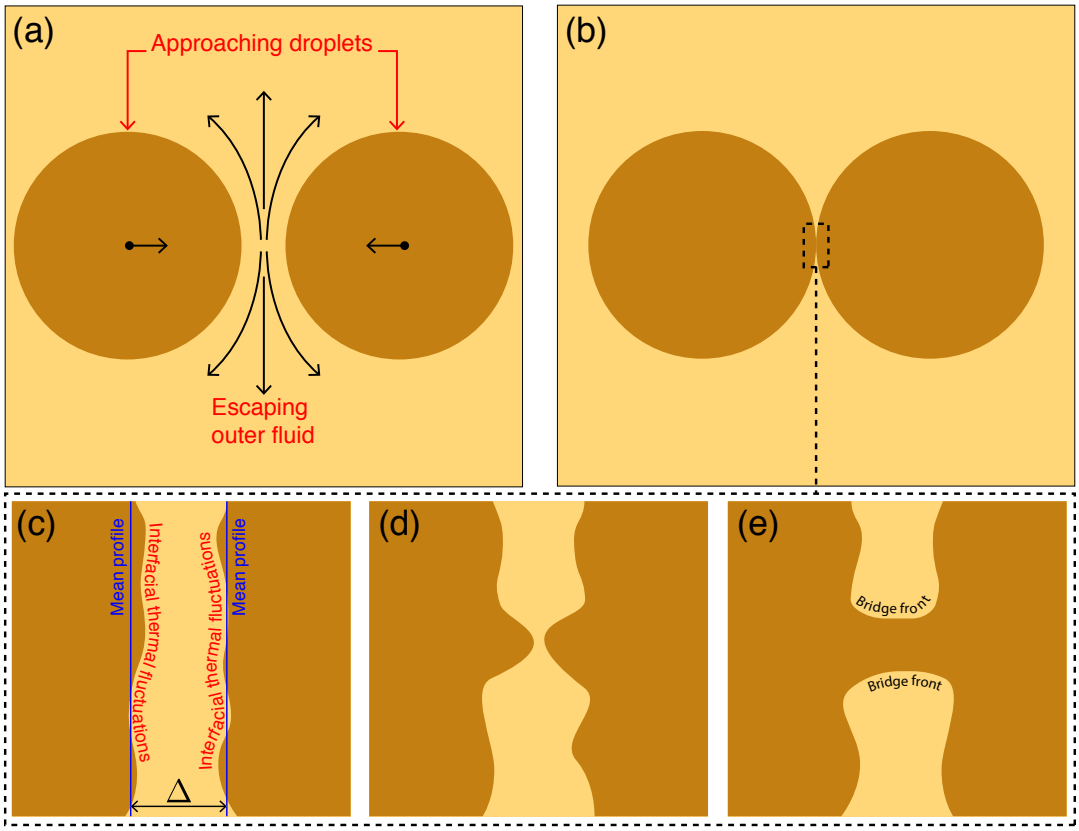

Figure 1.2: Schematic showing the approach and onset of coalescence of two droplets in an outer fluid. (a) As the droplets approach each other, the intervening fluid escapes from the gap between them. (b) The gap becomes very small. Depending on the speed of approach and the thermophysical properties of the fluids involved, there will be local deformations of the interfaces and the intervening gap size may remain constant (Δ) for a finite amount of time. (c) During this time, the interfacial thermal fluctuations on the droplet surface interact across the gap and the attraction will cause local 'bumps' to develop, as shown in (d), which grow exponentially in time. (e) The two bumps merge from opposite sides and results in the formation of the first contact between the droplets.

Λ_c can be derived as

$$\Lambda_c = \sqrt{\frac{-2\pi^2\gamma}{d^2G/d\Delta^2}}, \tag{1.1}$$

where Δ is the thickness of the intervening film. It can be shown that all Fourier modes with wavelengths $\Lambda > \Lambda_c$ will grow exponentially in time until the film ruptures (see Fig. 1.2(c,d,e)). Prevost and Gallez (1986) considered the non-linear effects on the stability of such films and found that non-linearities considerably accelerate the film rupture process.

Recent experiments have shown that the critical distance, $\Delta_{\min}$ below which the droplets spontaneously grow an 'irreversible capillary bridge' between their confronting interfaces follows a size-dependent scaling law (Chireux *et al.*, 2018). A dimensionless parameter $Ha \equiv 4A_H/3\pi\gamma R_{eq}^2$,

where $R_{eq} \equiv R_1 R_2/(R_1 + R_2)$, is defined to quantify the relative importance of attraction between interfaces over the capillary force (here, A_H is the Hamaker constant and R_1, R_2 are the radii of the two droplets). The non-dimensional critical distance $\Delta_{\min}/R_{eq}$ scales as $Ha^{1/3}$ for sub-micrometre droplets and $\Delta_{\min}/R_{eq} \sim Ha^{1/2}$ for larger droplets. Inevitably, the rupture of the intervening film results in establishing the first contact between the two bulks of the merging liquid.

1.1.2 Scaling laws for coalescence of liquid droplets

After a contact is established between the droplets (or a droplet and a planar interface as studied in Gillespie and Rideal (1956); Thoroddsen and Takehara (2000)), a capillary bridge connects both of them, which grows in time until both droplets merge to form a larger one. The speed at which droplets coalesce is determined by the growth dynamics of this bridge, which in turn depends on the interfacial tension, viscosities and densities of both coalescing and outer fluids. During electro-coalescence, where droplets coalesce in the presence of an external electric field, the growth dynamics of the bridge is affected by the electric field strength (Bird *et al.*, 2009; Ristenpart *et al.*, 2009). Traditional studies on droplet coalescence assume that the process is always driven by capillary force, and either viscous, inertial or both forces oppose it. While viscosity is thought to resist the capillary force in the beginning of the process – known as the *viscous regime*, inertia is expected to be the opposing force in the later stages – known as the *inertial regime*. A transition between these regimes occur when the strength of viscous and inertial forces are comparable. In what follows, this *time line* of droplet coalescence and different scaling laws derived to predict the bridge growth are discussed in detail.

One of the earliest and most commonly used studies describing the evolution of the capillary bridge is due to Hopper (1984), wherein he derived an analytical solution for the entire two-dimensional shape of coalescing cylindrical droplets as a function of time using conformal mapping techniques. The viscous-dominated coalescence of two identical cylinders in a passive outer gas (i.e. perfectly inviscid or absent) studied by Hopper (1984) is described by Stokes flow. Hopper's analysis provides an analytical solution to the non-dimensional bridge radius r_b/R and the height of the droplets h/R as a function of non-dimensional time (normalised by the viscous-capillary time scale $\tau_v \equiv \gamma R/\mu_l$, where μ_l is the liquid viscosity):

$$r_b/R = \sqrt{2}(1-m)(1+m^2)^{-1/2},\ h/R = \sqrt{2}(1+m)(1+m^2)^{-1/2}. \tag{1.2}$$

Here, m is a parameter that links t to r_b and h through a relationship:

$$t/\tau_v = \frac{\sqrt{2}\pi}{4}\int_{m^2}^{1}[\tau(1+\tau)^{1/2}K(\tau)]^{-1}d\tau,\ K(\tau) = \int_0^1[(1-x^2)(1-\tau x^2)]dx, \tag{1.3}$$

where τ and x are two arbitrary variables of integration. Figure 1.3 shows the bridge evolution as described by Eq. (1.2). It must be noted that the speed of bridge growth diverges as the 'time

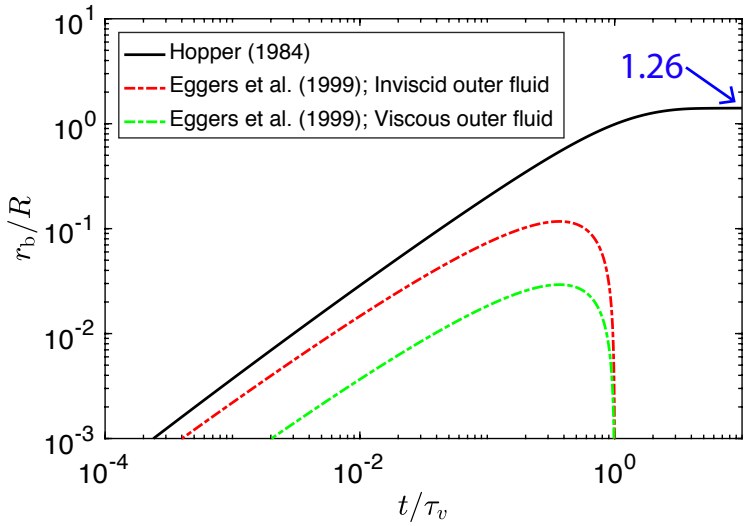

Figure 1.3: Bridge growth in time as described in Hopper (1984) and Eggers *et al.* (1999). A simple volume balance gives the radius of the final droplet to be $2^{1/3} \approx 1.26$ times the radii of the initial droplets. Hopper's solution shows that coalescence of two droplets of a highly viscous liquid continues 'smoothly' until the final droplet is formed. Eggers *et al.* (1999) derived analytical expressions for the bridge growth when outer fluid is viscous and inviscid. The time is normalised with the viscous-capillary time scale $\tau_v \equiv \gamma R/\mu_l$. In the cases where the outer fluid has non-zero viscosity, their equation is only expected to hold for $r_b/R < (\mu_g/\mu_l)^{2/3}$. For the inviscid case, its validity is restricted to $r_b/R < 0.03$.

since coalescence' approaches zero. Such divergences in the bridge growth are characteristic of many traditional models, since they predict singularities caused by infinite free-surface curvature at the bridge front when the droplets first meet. Hopper (1984) also provides a parametric form of the free-surface shape of the coalescing droplets that are used in many computational studies to generate an initial free-surface shape during coalescence (Sprittles and Shikhmurzaev, 2014a,b).

While Hopper's analytical solution deals with the case of inviscid outer fluid, Eggers *et al.* (1999) discuss coalescence of liquid droplets in an outer fluid of non-zero viscosity. Eggers *et al.* (1999) used Stokes flow to argue that droplet coalescence will always be viscous dominated in the initial stages. The driving capillary force is primarily attributed to the longitudinal curvature $1/\Delta$ (see Fig. 1.4(c)). Subsequently, the development of the bridge radius is shown to have a logarithmic dependence on time:

$$\frac{r_b}{R} = -C_v \frac{t}{\tau_v} \ln\left(\frac{t}{\tau_v}\right);\ C_v = \frac{\alpha - 1}{2\pi};\ \alpha = \begin{cases} 3, & \mu_g/\mu_l = 0, \\ 3/2, & \mu_g/\mu_l > 0. \end{cases} \tag{1.4}$$

It is interesting to note that the above equation is independent of the gas-to-liquid viscosity ratio, μ_g/μ_l, when $\mu_g/\mu_l > 0$. Eggers *et al.* (1999) also suggests that, in the cases where the

outer fluid has non-zero viscosity, their equation is only expected to hold for $r_b/R < (\mu_g/\mu_l)^{2/3}$. For the inviscid case, its validity is restricted to $r_b/R < 0.03$.

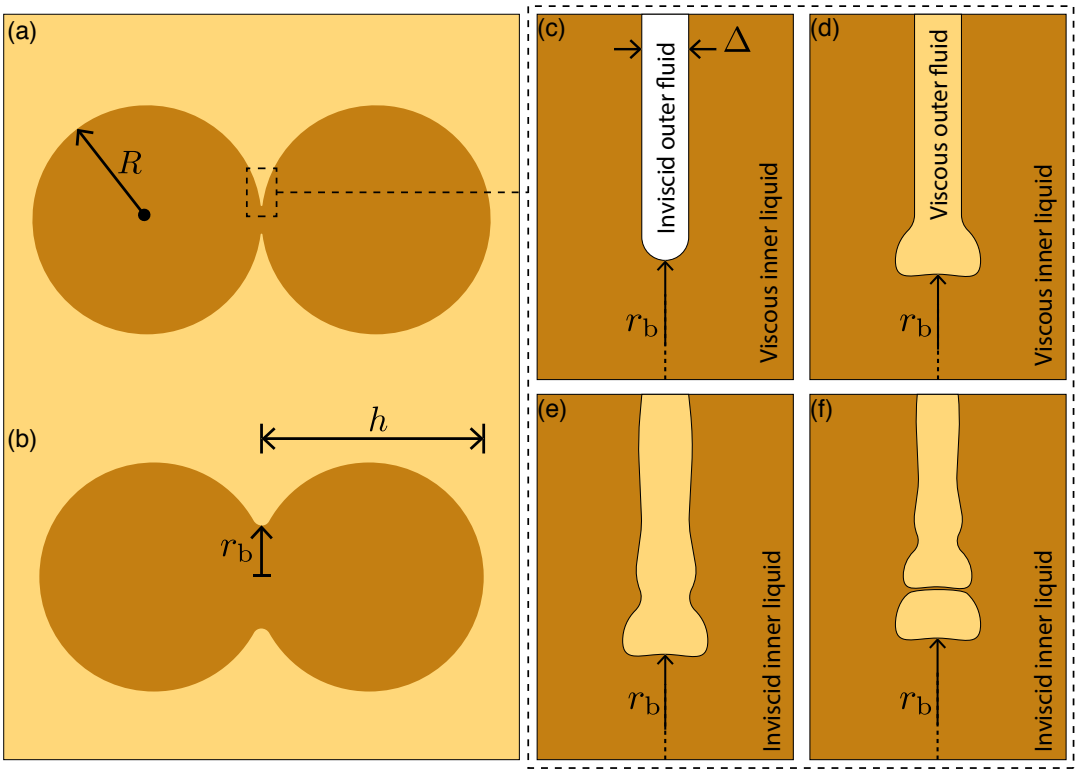

Figure 1.4: (a,b) Coalescence of two droplets of radii R and definitions of the bridge radius r_b and height h. Free-surface shape evolution in time as described in Eggers *et al.* (1999) (c,d) and in Duchemin *et al.* (2003) (e,f). (c) A passive outer fluid results in no bubble formation close to the bridge front. (d) When the outer fluid is viscous (no matter how small its viscosity is), a non-enclosed toroidal bubble is developed at the bridge front. (e) When two inviscid droplets coalesce, capillary waves are formed next to the bridge front that travel along the free-surface. (f) The first bubble becomes enclosed by the coalescing liquid at one point in time, which gives rise to the formation of a 'new bridge front' that advances forward.

Nevertheless, no experiments have observed the logarithmic growth of the bridge as described by Eq. (1.4). In the early stages of coalescence, a linear regime is often observed instead (Paulsen *et al.*, 2011; Burton and Taborek, 2007; Aarts *et al.*, 2005). The initial speed of the bridge growth in this regime is obtained by setting the capillary number to unity, which suggests $r_b \sim \gamma t/\mu$. Paulsen *et al.* (2012) classified this as an 'inertially-limited-viscous' regime and argued that it will always be the initial regime of droplet coalescence. However, Sprittles and Shikhmurzaev (2014b) constructed a phase diagram of droplet coalescence (Reynolds number based on droplets radii $\mathrm{Re}_R \equiv \rho_l \gamma R/\mu_l^2$ vs. r_b/R, where ρ_l is the coalescing liquid density) and showed that Hopper's solution best approximates the dynamics in the early stages of coalescence and argued that the inertially-limited-viscous regime is merely a characteristic of the global motion of the droplets. A 'transition regime' is also identified wherein both viscous

and inertial forces are relevant.

A particular characteristic of the free-surface shape that Eggers *et al.* (1999) observed in their simulations is the existence of non-enclosed toroidal bubbles (see Fig. 1.4(d)) next to the bridge front for the cases where the outer fluid has non-zero viscosity. Consequently, the gap width at the meniscus is much larger than that in the absence of an external fluid. The external fluid caught inside the bubble only escapes when $r_b/R > 0.1$. Although the majority of the analysis are performed for 2D parallel coalescing cylinders, Eggers *et al.* (1999) also established that the dynamics is asymptotically equivalent to the coalescence of 3D spherical droplets in the early stages. This was further validated in later experiments (Burton and Taborek, 2007). Prior to work presented in this thesis, traditional theories therefore suggest that droplet coalescence will always be viscous dominated in its initial stages.

The effects of viscosity diminishes as time proceeds and at one point the dynamics switches from Stokesian to Eulerian (Eggers *et al.*, 1999). At this 'crossover' point, the Reynolds number $\mathrm{Re} \equiv \rho_l \gamma r_b/\mu_l^2 \approx 1$, where the dominant length scale is assumed to be of size r_b and a velocity scale is assumed to be γ/μ. In other words, the crossover point is characterised by

$$r_b \approx l_v \equiv \frac{\mu_l^2}{\rho_l \gamma}, \tag{1.5}$$

where l_v is the 'viscous length scale'. This crossover can also be represented alternatively as

$$r_b/R \approx \mathrm{Oh}_l^2;\ \mathrm{Oh}_l \equiv \frac{\mu_l}{\sqrt{\rho_l \gamma R}}, \tag{1.6}$$

where Oh_l is the *Ohnesorge number* of the process based on liquid properties, which quantifies the relative magnitude of viscous force as opposed to inertial and surface tension forces.

Paulsen *et al.* (2011) subjected the above hypothesis to rigorous experimental validation and found that the crossover, in fact, happens when $r_b/R \approx \mathrm{Oh}_l$ and not when $r_b/R \approx \mathrm{Oh}_l^2$. They used a novel experimental technique, in which they passed an alternating current through slightly conducting droplets, giving them access to small length and time scales that were previously unexplored ($r_b \sim 1$ μm and $t \sim 10$ ns after the first contact). The glycerol content in the coalescing liquid, which is saturated with NaCl to make it electrically conductive, was varied in order to achieve variation in viscosity over two orders of magnitude. The crossover time is found to vary as μ_l^2 instead of μ_l^3, which would have been the case if the crossover had corresponded to $r_b/R \approx \mathrm{Oh}_l^2$. They identified that the length scale over which a dominant flow occurs is of the order of the gap width between the coalescing droplets, $\Delta = r_b^2/R$ and not r_b.

This crossover ends in an 'inertial regime', where inertial force is expected to oppose the driving surface tension force. Since the effects of viscosity are negligible, the far field conditions do not affect the dynamics of the bridge growth. Eggers *et al.* (1999) assumed that the driving capillary pressure is predominantly due to the sharp meniscus at the bridge front quantified by

γ/Δ. This capillary pressure must be balanced by the dynamic pressure at the bridge front $\rho_l v^2$, where $v = dr_b/dt$. Consequently,

$$\rho_l \left(\frac{dr_b}{dt}\right)^2 \sim \frac{\gamma R}{r_b^2}. \tag{1.7}$$

Integrating the above equation gives:

$$\frac{r_b}{R} = C_i \left(\frac{t}{\tau_i}\right)^{1/2}; \ \tau_i \equiv \left(\frac{\rho_l R^3}{\gamma}\right)^{1/2}, \tag{1.8}$$

where C_i is an unknown constant, expected to be $\mathcal{O}(1)$ and τ_i is the inertial-capillary time scale. The rate of bridge growth in the inertial regime scales as $t^{-1/2}$. Unlike for the viscous regime, the coupling between pressure and velocity requires the pre-factor C_i to be determined by alternative means (Sprittles and Shikhmurzaev, 2014a). Pothier and Lewis (2012) showed through molecular dynamics (MD) simulations of coalescing liquid metal droplets that the pre-factor C_i is not universal and it depends on system properties including initial radii of the droplets, viscosity and surface tension of coalescing liquid.

Duchemin *et al.* (2003) extended the study of Eggers *et al.* (1999) in the inertial regime and found that the coalescence of low-viscosity liquid droplets involves sequential entrapment of enclosed bubbles, whose evolution can be described by self-similar solutions. Predictions of their theoretical analysis were validated using high-precision boundary integral numerical simulations. They showed that enclosed toroidal bubbles (see Fig. 1.4 (e,f)) are formed at the bridge front as the confronting surfaces of the droplets reconnects in finite time, which in turn gives rise to the development of another open bubble in front of it, which will become enclosed later and so on. When averaged over many such discrete events, the $t^{1/2}$ scaling of the bridge front is recovered. Many numerical studies (Paulsen *et al.*, 2012; Sprittles and Shikhmurzaev, 2012; Duchemin *et al.*, 2003) including those employing molecular dynamics (Liang and Keblinski, 2015) and experiments (Paulsen *et al.*, 2012; Menchaca-Rocha *et al.*, 2001; Thoroddsen *et al.*, 2005; Eiswirth *et al.*, 2012) have observed this scaling of the bridge growth in the inertial regime. Although Duchemin *et al.* (2003) predicted the value of the pre-factor C_i to be 1.62, experimental observations measured it to be in the range of 1.03 – 1.29 (Wu *et al.*, 2004; Aarts *et al.*, 2005).

However, formation of toroidal bubbles and subsequent reconnections are not observed in experiments of coalescence of low-viscosity droplets even when using the high-resolution electrical method (Case, 2009; Case and Nagel, 2008). It is also possible that this behaviour occurs at a time scale that is much smaller than the time resolution of these experiments.

During the bridge growth in the inertial regime, if the gap width (Δ) remains constant,

$$\rho \left(\frac{dr_b}{dt}\right)^2 \sim \frac{\gamma}{\Delta}, \tag{1.9}$$

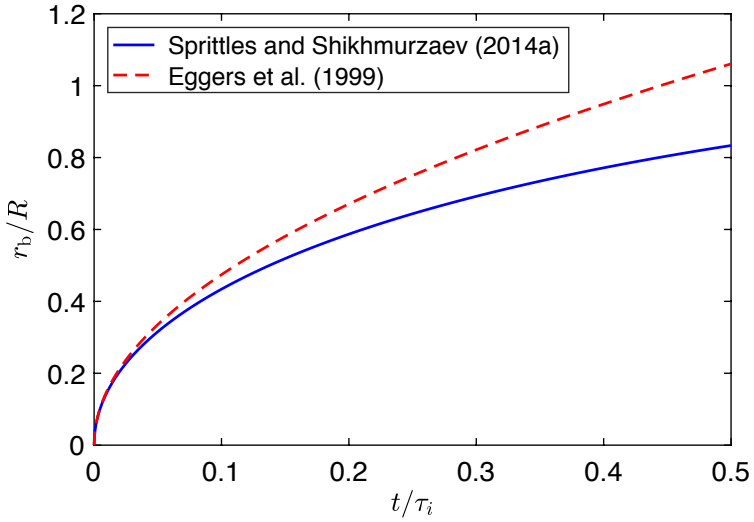

Figure 1.5: Bridge growth in inertial regime as described in Eggers *et al.* (1999) and Sprittles and Shikhmurzaev (2014a). Both curves are drawn with $C_i = 1.5$.

which results in the bridge radius to grow linearly in time:

$$r_b = C_i' \left(\frac{\gamma}{\rho \Delta} \right)^{1/2} t. \tag{1.10}$$

This scenario happens only during the coalescence of low-viscosity droplets. Case (2009) attributed this linear bridge growth in the inertial regime to the presence of surfactants on the droplet surfaces. Surfactants can prevent droplets from coalescing due to the resulting repulsion, causing the droplets to undergo slight flattening near the tip, which will keep Δ constant.

The scaling law in the inertial regime (Eqs. (1.8) and (1.10)) is derived by assuming that the driving capillary pressure is due to the longitudinal curvature of the free surface ($\sim 1/\Delta$); the opposing capillary pressure due to the azimuthal curvature ($1/r_b$) is neglected. For water droplets of $R \sim 1$ mm, which is the size that is usually studied in experiments, coalescence crosses over to inertial regime when $r_b/R \sim \mathrm{Oh}_l = \mathscr{O}(10^{-2})$. Even for droplets coalescing in microfluidic devices, where, say $R \sim 10$ μm, this crossover happens when $r_b/R \sim \mathscr{O}(10^{-1})$. In other words, for many of the applications that rely on the merger of low viscosity droplets, coalescence proceeds in the inertial regime for the majority of the dynamics. Therefore, determining the accurate scaling law for the bridge evolution is essential, when it comes to studying such processes that have numerous engineering applications.

For rectifying the shortcomings of the existing scaling laws in the intertial regime, Sprittles and Shikhmurzaev (2014a) included the contribution of capillary pressure due to the azimuthal curvature in their analysis and derived a new explicit analytical expression for the bridge front

propagation:

$$\bar{r}_b^3 + 3\bar{r}_b^2 + \frac{3C_i^2\bar{t}}{4}\left(\frac{3C_i^2\bar{t}}{4} - 4\right) = 0, \tag{1.11}$$

where $\bar{r}_b \equiv r_b/R$, $\bar{t} \equiv t/\tau_i$.

Eq. (1.11) is compared with Eq. (1.8) in Fig. 1.5. Since the bridge growth is opposed by azimuthal curvature, the speed is reduced to what is suggested by Sprittles and Shikhmurzaev (2014a) and has been shown to closely match with experiments. This indicates that the late stage dynamics is well understood in the literature, particularly because the length and time scales involved are easily accessible in experiments.

In summary, according to traditional hydrodynamics, droplet coalescence always begin in a viscous regime, which will later cross over to an inertial regime through a 'transition regime'. For high-viscosity droplets, it is not necessary for an inertial regime to be present towards the end. The motion in the viscous regime can be approximated by Stokes equations, i.e. by neglecting the inertial terms, and motion in the later inertial regime can be modelled using Euler's equations. In the transition regime, the full Navier-Stokes equations are essential for the accurate modelling of the coalescence process and so it may not be possible to obtain simple analytical solutions in the transition regime. More importantly, it must be noted that all traditional theories predict the existence of an unphysical mathematical singularity in the beginning of coalescence, where measurable quantities, like local velocity and pressure, diverge due to the infinite free-surface curvature when the droplets first meet. In numerical studies, this singularity is avoided by beginning the simulation with an arbitrarily small bridge existing between the droplets. This may have adverse effects on the accuracy of these simulations.

1.1.3 Contact line motion during wetting

The wetting of a solid by a liquid is ubiquitous in our daily lives: spreading of ink on papers inside printers, wetting of wall/canvas by paint, coating of specially treated surfaces in industries and spreading of pesticides on plant leaves. Owing to its numerous practical applications, dynamic wetting of a solid by a liquid has been a subject of many theoretical (Blake and Haynes, 1969; de Ruijter *et al.*, 1999; Blake and De Coninck, 2011), computational (Blake *et al.*, 1997; de Ruijter *et al.*, 1999; Bertrand *et al.*, 2009; Blake and De Coninck, 2011; Chen *et al.*, 2014; Lukyanov and Likhtman, 2016) and experimental work (Bird *et al.*, 2008; Winkels *et al.*, 2012; Duvivier *et al.*, 2013).

A droplet of a liquid, when placed slowly on a substrate, will spread on it depending on how well it interacts with the solid at a molecular scale. The spreading process is a consequence of the general tendency of any system to minimize its interfacial free energy. For quantifying the wetting properties of a liquid on a given solid substrate, an equilibrium contact angle (θ_c) is defined as the angle made by the liquid/liquid or liquid/vapour interface on the solid substrate, which is measured through the liquid of interest at the point where all three phases meet.

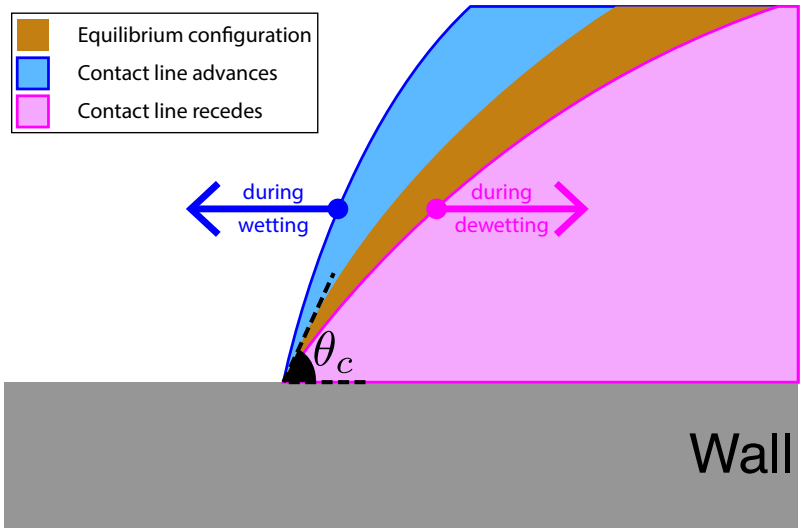

Figure 1.6: The figure illustrates the configurations of the liquid/vapour interface when it wets/dewets a solid. The contact angle associated with the wetting configuration is larger than that associated with the equilibrium configuration. The contact angle associated with the dewetting configuration is smaller than the former two.

Under equilibrium conditions, i.e. after the spreading has finished, the contact angle will have a minimum value. The equilibrium configuration of such a system can be classified as completely wetting ($\theta_c = 0^\circ$) or partially wetting ($\theta_c > 0^\circ$). A characteristic of the complete wetting is that a thin (~ 10 nm) *precursor* film advances ahead of the apparent contact line. In the partial wetting regime, if $\theta_c < 90^\circ$, the liquid is said to wet the substrate, and is non-wetting if $\theta_c > 90^\circ$.

Under many circumstances, it is imperative to know not just how well a liquid wets a solid, but also how fast it wets or dewets it. The speed at which it takes place is occasionally the controlling factor in process design. During wetting/dewetting, the instantaneous contact angle – otherwise known as the dynamic contact angle θ_d – is mostly of interest. The instantaneous contact angle measured when a liquid interface advances on a solid surface (i.e. during wetting) is known as the advancing contact angle ($\theta_d = \theta_a$), and the instantaneous contact angle measured when a liquid interface recedes on a solid surface (i.e. during dewetting) is known as the receding contact angle ($\theta_d = \theta_r$). Generally, liquids satisfy the relation: $\theta_a > \theta_c > \theta_r$, as shown in Fig. 1.6. Experimentally it is observed that the advancing contact angle increases with the wetting velocity, whereas the receding contact angle decreases with it. Determining the velocity dependence of the dynamic contact angle has been the main aim of many previous works and researchers have approached this problem from different perspectives.

The dynamics of the spreading process can also be studied by looking at the dependence of the contact radius of the wetted area on the solid as a function of time. An imaginary line, which demarcates the wetted region and the non-wetted region on the solid, termed as the *contact line* (CL), is often used to locate the extent of the wetted area during spreading. Although it is

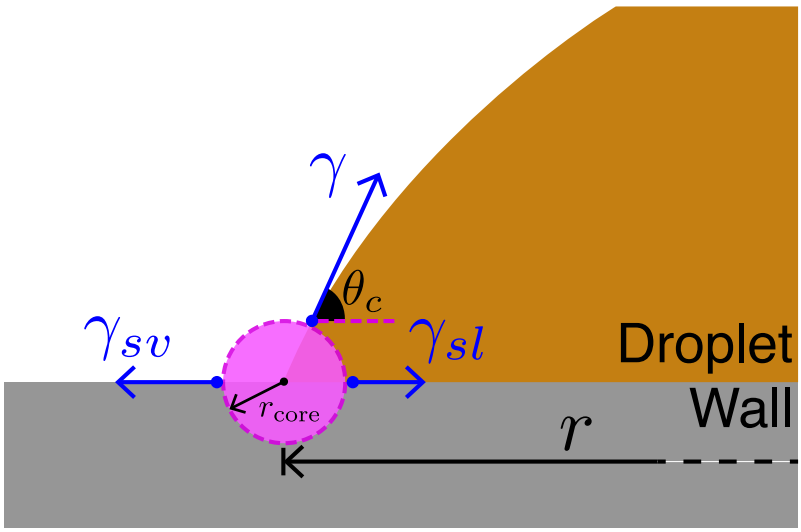

Figure 1.7: Definition of contact angle (θ_c) based on far-field interfacial energies per unit area. θ_c can be defined without having the knowledge of what happens in the core region. Here, γ_{sv}, γ_{sl} and γ are the solid-vapour, solid-liquid and liquid-vapour interfacial tensions, respectively and r is the contact radius at the base of the droplet.

traditionally considered as a line of infinitesimal thickness, theory (de Gennes, 1985) and many molecular dynamics simulations (Winkels *et al.*, 2012; Zhang *et al.*, 2017) have shown that it is a region of finite thickness, much like any interface between two phases. In fact, there exists a *core region* close to where the contact line is supposed to occur with a thickness of $r_{\text{core}} \sim \gamma/E$, where E is the Young's modulus of the substrate (see Fig. 1.7).

It is possible to write a relationship between the far-field (i.e. far from the core region) energy parameters (solid/liquid (γ_{sl}), solid/vapour (γ_{sv}) and liquid/vapour (γ) interfacial tensions) and the equilibrium contact angle (see Fig. 1.7):

$$\cos\theta_c = \frac{\gamma_{sv} - \gamma_{sl}}{\gamma}. \tag{1.12}$$

The above relation is the ubiquitous Young's equation. As the size of the spreading droplet is decreased, such as in nanodroplets, the *line tension* comes into play, which has an effect on the equilibrium contact angle. Line tension is assumed to arise due to the modification of the droplet profile close to the substrate owing to the intermolecular interactions between the spreading liquid and the substrate. Subsequently, a modified Young's equation has been suggested for nanodroplets:

$$\cos\theta_c = \frac{\gamma_{sv} - \gamma_{sl}}{\gamma} - \frac{T_L}{\gamma r}, \tag{1.13}$$

where T_L is the line tension and r is the contact line radius. It must be noted that for *large enough* droplets ($R \gg T_L/\gamma$), θ_c is independent of droplet size. In particular, numerical simulations often use cylindrical droplets ($r \to \infty$) to avoid the complications due to contact line tension.

In terms of contact radius of the droplet, Winkels *et al.* (2012) observed a wettability-independent spreading regime in the initial stages of spreading where $r \sim C\sqrt{t}$ on partially wetting surfaces. The pre-factor C is found to be dependent on θ_c. After this initial stage, Bird *et al.* (2008) observed that the spreading follows a power-law dependence on time such that $r \sim t^{\alpha}$, where the exponent α is dependent on θ_c.

During complete wetting, the initial dynamics is nearly identical to droplet coalescence with a film of the same liquid. This similarity arises due to the presence of precursor films that spread ahead of the apparent contact line (whose location is indicated by r) at a much faster rate, and so the droplet essentially spreads on a film of its own liquid. As discussed in the previous section, under such circumstances, the power-law describing the spreading dynamics depends on the force resisting the driving capillary force. When inertia opposes the motion, $r \sim \sqrt{t}$ and when viscosity opposes, $r \sim t$ with a weak logarithmic dependence on time. However, the late stage dynamics of complete wetting, i.e. after the droplet has achieved a spherical cap shape, the dynamics is governed by Tanner's law, where $r \sim t^{1/10}$. This extremely slow dynamics results from a balance of surface tension and viscous forces near the apparent contact line. It is worth noting that Tanner's law is a limiting case of a more general spreading behaviour, which arises when a viscous liquid spreads on its own film (Cormier *et al.*, 2012).

In general, the spreading of a droplet on a solid is associated with four dissipation mechanisms: (a) the viscous losses within the bulk of the spreading droplet (Φ_v), (b) losses in the precursor film in the case of complete wetting (Φ_f), (c) losses due to liquid slipping on the wall (Φ_s) and (d) losses in the core region due to the interface formation/disappearance as the contact line moves (Φ_c). While the final configuration of the system depends on the minimization of its free energy, the path along which it is achieved depends on the relative magnitudes of these dissipation mechanisms. Analysing various losses will give an understanding about the dependence of contact line velocity on the dynamic contact angle. While usual hydrodynamic theories can model the viscous losses in the system, a more detailed description of the contact line motion involving local effects are necessary to quantify, particularly, the fourth kind of dissipation.

Experiments of Dussan V. and Davis (1974) showed that the contact line motion results from a rolling type movement of the droplet surface close to the substrate that is reminiscent of the chain wheels of a caterpillar vehicle. A 'wedge' of liquid is assumed to roll over the underlying solid with constant contact line velocity (V_{CL}) and angle (θ_d). The hydrodynamics of such a scenario was first studied by Huh and Scriven (1971) using the lubrication approximation. They showed that the application of Navier-Stokes equations with the standard no-slip boundary condition leads to stress singularity around the contact line. This dissipation is quantified as

$$\Phi_v = \frac{3\mu V_{\mathrm{CL}}^2}{\theta_a} \ln\left(\frac{x_{max}}{x_{min}}\right). \tag{1.14}$$

The upper cut-off x_{max} is expected to be of the order of R. A non-zero value of x_{min} is required to avoid the divergence of this type of dissipation. Several other hydrodynamic models exist in the literature that emphasize this dissipation channel (Voinov, 1977; Cox, 1986).

If the contact line dissipation is neglected, $\Phi_f = SV_{\mathrm{CL}}$, where S is the spreading coefficient (de Gennes, 1985). Of course, this channel of dissipation need not be considered in the case of partial wetting. A straightforward way of quantifying Φ_s is to incorporate slip as a boundary condition in the standard hydrodynamic models of wetting. However, precise quantification of this channel of dissipation requires a molecular point of view of liquid slippage that incorporates density stratifications near the wall, which is usually neglected in traditional hydrodynamics.

Thompson and Robbins (1989) studied the Couette flow simulations of two immiscible liquids confined between solid walls using molecular dynamics and showed that the no-slip boundary condition breaks down within a few atomic thickness from the contact line. This suggests the corresponding break down of the usual hydrodynamic theory at atomic scales and requires a model that can incorporate molecular effects to quantify the last type of dissipation: Φ_c. Shikhmurzaev (1993, 1997) developed an innovative hydrodynamic framework that can incorporate the local effects near the core region. This model assumes that the material properties of the interface close to the core region is different from their equilibrium values due to an interface formation/disappearance process occurring as the contact line traverses the solid surface during wetting/dewetting. The dissipation in the core region is attributed to this interface formation/disappearance process. In this model, the dynamic contact angle emerges as a solution to the system of equations and it is not an imposed quantity as in other hydrodynamic models. However, some of the parameters involved still have to be determined from experimental data by curve fitting.

The molecular kinetic theory (MKT) of dynamic wetting (not to be confused with the kinetic theory of gases) developed by Blake and Haynes (1969) and later extended by Blake and De Coninck (2002) describes dynamic wetting as a stress-modified rate process. The contact line motion is described as a consequence of a large number of individual jumps of the molecules belonging to the liquid phase on top of the potential energy landscape formed by the substrate atoms (see Fig. 1.8). MKT describes Φ_c by assuming the existence of a *contact line friction* as the contact line moves over the substrate surface. Due to the thermal motion of the liquid molecules, coupled with the force which drives the wetting process, the liquid molecules traverse the energy landscape until an equilibrium configuration is achieved. Their motion is characterised by an average distance of jumps (λ) and the equilibrium frequency of such jumps (κ_0). Figure 1.9 schematically shows how the contact line advances due to several molecules at the three-phase-zone (TPZ) jumping over the sites of wall atoms and shows the definition of λ. This physical mechanism of contact line motion is the foundation of MKT.

Blake and Haynes (1969) assumed that the driving force during spreading is the out-of-balance

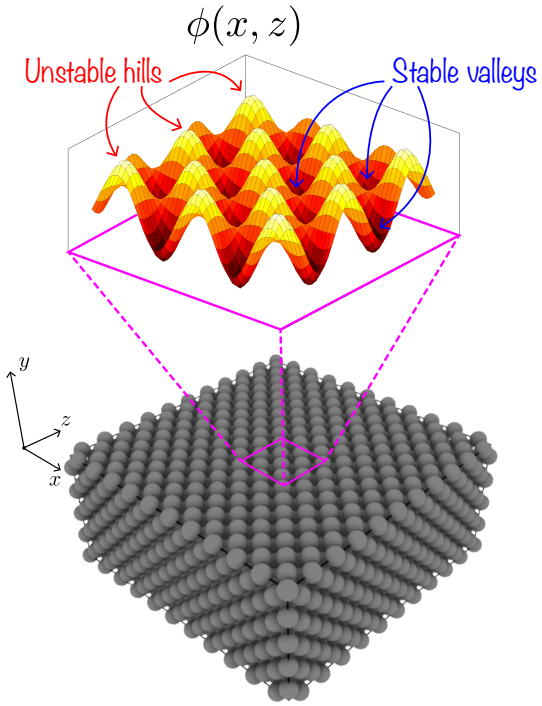

Figure 1.8: An illustration of the potential energy landscape on top of a substrate surface under equilibrium conditions. Unstable hills are located right on top of the wall atoms, while stable valleys are located in the 'adsorption sites' between wall atoms. Liquid molecules tend to spend more time in these sites while traversing the energy landscape during spreading. The local potential energy is evaluated by placing a single liquid molecule at a distance σ above the top wall layer and then calculated using the LJ potential (see Chapter 2).

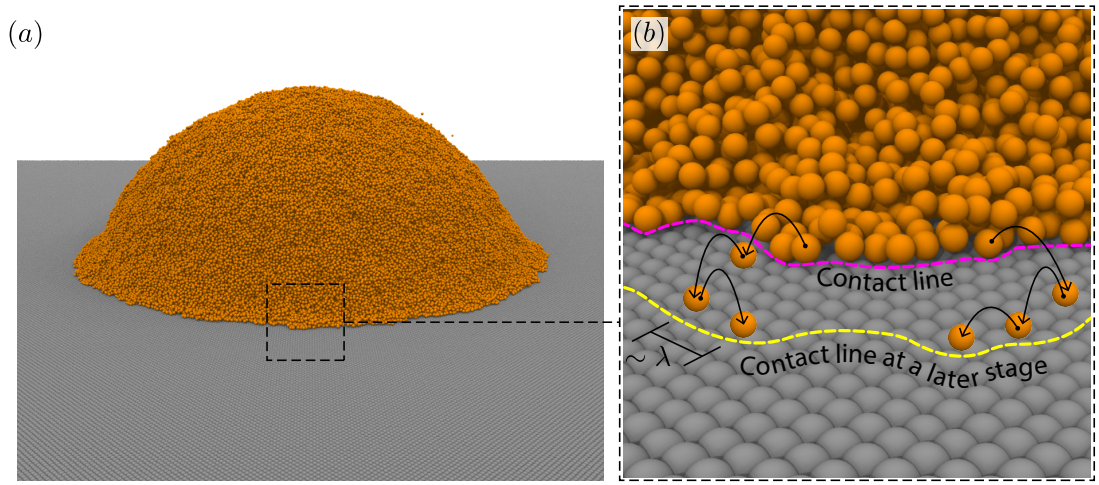

Figure 1.9: (a) Instantaneous snapshot of a spherical droplet spreading on a hydrophilic wall. (b) Enlarged image from near the three-phase-zone illustrates how a large number of individual jumps of the molecules at the three-phase-zone on the surface takes the contact line to its new location, as suggested by MKT.

surface tension force $\gamma[\cos(\theta_c) - \cos(\theta_d)]$, and the work done by this force is spent entirely in modifying the potential energy landscape over the surface, so that there is net motion in the direction of applied force. Under such circumstances, MKT predicts the CL velocity to be

$$V_{\mathrm{CL}} = 2\kappa_0\lambda \ \sinh\left(\frac{\gamma[\cos(\theta_c) - \cos(\theta_d)]}{2nk_BT}\right), \tag{1.15}$$

where n is the number of adsorption sites per unit area. In the linear limit, i.e. when the argument of sinh is small, the above equation can be rewritten in the form

$$V_{\mathrm{CL}} = \frac{\gamma}{\zeta}(\cos(\theta_c) - \cos(\theta_d)), \tag{1.16}$$

where $\zeta \equiv k_BT/\kappa_0\lambda^3$ is the contact line friction coefficient, which quantifies the contact line dissipation in the linear regime. MKT has been compared to many experiments in this linear limit with reasonable agreements (Duvivier *et al.*, 2013) and has been applied to develop multiscale simulation methods of dynamic wetting in its full form (Zhang *et al.*, 2017). Recent molecular dynamics simulations reported the non-linear regime of MKT when a liquid displaces another liquid (Wang *et al.*, 2019).

1.1.4 Coalescence-induced jumping of droplets

Many industrial and natural processes rely on water droplets condensing from a vapour phase on to a hydrophobic surface. Drop-wise condensaton has high phase-change heat transfer performance when compared to film-wise condensation (Rose, 2002), provided the condensate droplets are rapidly removed from the surface, leaving space for re-nucleation. Traditionally, gravity is required for the removal of these condensate droplets from an inclined or vertical plate (Kim *et al.*, 2002; Dimitrakopoulos and Higdon, 1999), but the droplet radius has to be on the order of the capillary length $l_\gamma = \sqrt{\gamma/\rho_l g}$, where g is the acceleration due to gravity; sub-millimetre sized water droplets cannot be dislodged in this way.

Experimental studies (Boreyko and Chen, 2009) have shown that smaller droplets can be removed from superlyophobic surfaces (with contact angle $\theta_c \geq 150^\circ$ and small contact angle hysteresis) by a self-induced jumping mechanism (see Fig. 1.10). This rapid self-coalescence and consequent lift-off behaviour of the condensate droplets results from the excess surface free energy released after coalescence being partially converted into kinetic energy of the final droplet. It has also been observed that nature has already been utilising this phenomena for various purposes, such as in self-cleaning of cicada wings (Wisdom *et al.*, 2013) and plant leaves (Mockenhaupt *et al.*, 2008), and in dew droplet removal from gecko skin (Watson *et al.*, 2011).

There have been several studies on this topic to understand the underlying dynamics of this process (Miljkovic *et al.*, 2013; Enright *et al.*, 2012; Boreyko and Collier, 2013; Enright *et al.*,

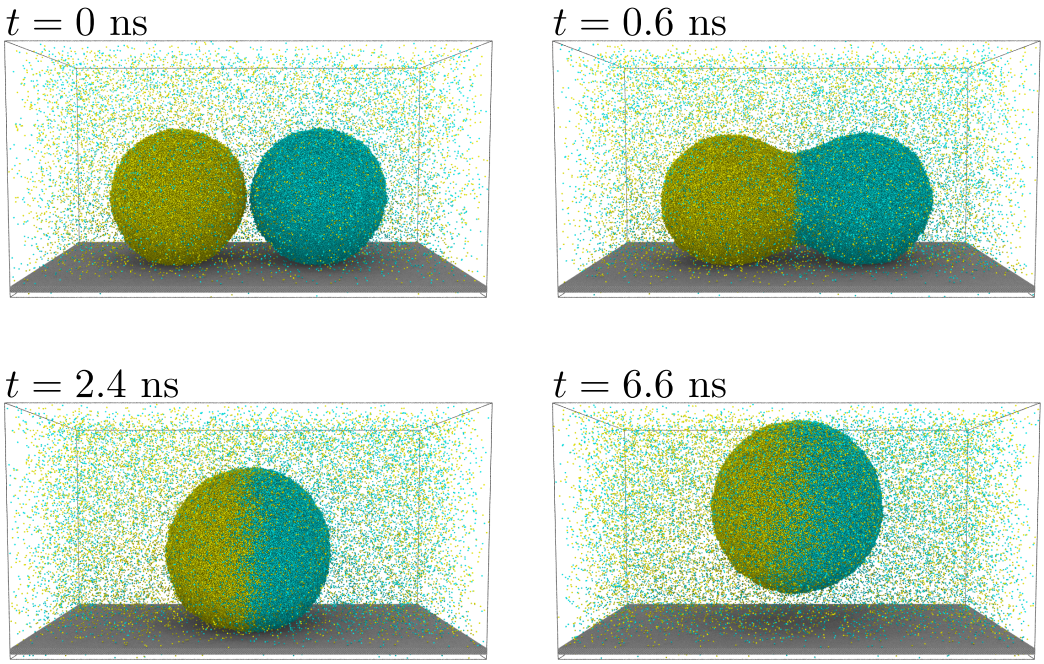

Figure 1.10: Coalescence-induced jumping of two argon droplets ($R = 55.2$ nm) from a superlyophobic surface in argon vapour at various timesteps of a molecular dynamics simulation (conducted in this work). Molecules from different droplets are coloured differently for ease of illustration.

2013; Nam *et al.*, 2013). During coalescence and jumping of two droplets, after the rupture of the intervening fluid film, the liquid bridge that forms between them grows quickly, hits the underlying surface and provides a reaction force for the final droplet to take off with a speed V_g (Liang and Keblinski, 2015; Sheng *et al.*, 2017; Enright *et al.*, 2014) (here, subscript 'g' denotes coalescence happens in the presence of a gaseous atmosphere). If the entire excess interfacial energy released during coalescence is converted into the final jumping kinetic energy of the droplet, the energy balance reads:

$$\gamma R^2 \sim \rho_l R^3 V_g^2. \tag{1.17}$$

Rearranging gives:

$$V_g \sim U \equiv \sqrt{\frac{\gamma}{\rho_l R}}, \tag{1.18}$$

where U is the inertial-capillary velocity scale. Notably, U is only a good predictor of V_g when viscous effects are negligible, which occurs when $\mathrm{Oh}_l = \mu_l / \sqrt{\rho_l \gamma R}$ is sufficiently small.

The above equation assumes that all the velocity components in the bulk of the droplets during the coalescence process contribute to the translational kinetic energy of the final droplet. Enright *et al.* (2014) studied the coalescence-induced jumping of droplets from superhydrophobic surfaces using numerical simulations and showed that only the unbalanced momentum com-

ponents can contribute to the translational motion of the final droplets. Hence, the jumping speed V_g is usually only a fraction of U, even if other factors such as gravity, viscous effects and adhesion in the system are negligible. In their numerical simulations, they found that a capillary wave propagates along the droplet surfaces from the initial point of contact and the corresponding variation in the capillary pressure with respect to its initial value decreases as Oh_l is increased, which is in accordance with the idea that Oh_l represents a dimensionless viscosity. This results in characteristic changes in both the interfacial shape evolution and internal flow dynamics during coalescence. They also showed that the jumping process is fundamentally inefficient with only about 6% of the available excess surface free energy being converted into the translational kinetic energy of the jumping droplet.

In general, while the jumping process is suppressed by internal viscous dissipation for smaller droplets (Wang *et al.*, 2011; Enright *et al.*, 2014), it is limited by gravity for relatively large ones ($R \sim l_\gamma$) (Peng *et al.*, 2013). Wang *et al.* (2011) derived an analytical expression for the jumping speed as a function of the droplet size:

$$V_g = \sqrt{\frac{\gamma}{\rho R}}\left[\frac{3}{8}\Gamma - 24\frac{\mu_l}{\sqrt{\rho_l \gamma R}}\right]^{1/2}, \tag{1.19}$$

where Γ is a term that quantifies the adhesion from the surface. Peng *et al.* (2013) improved the analysis of Wang *et al.* (2011) and observed a better match with experimental data.

The role of surface adhesion on the jumping speed is studied in detail by Cha *et al.* (2016). They report data from experiments of droplet jumping from ultralow-adhesion carbon nanotube (CNT) surfaces. CNTs of diameter ~ 7 nm and deposit thickness ~ 1 μm are grown on a silicon wafer allowing them to obtain ultralow-adhesion, coupled with negligible contact angle hysteresis. By manipulating the saturation temperature and relative humidity of the incoming vapour on to the substrate, the condensate nucleation density is maximized and jumping of droplets as small as $R \approx 500$ nm is observed. From the viscous-to-inertial crossover radius suggested by Paulsen *et al.* (2011), Cha *et al.* (2016) showed that for the lowest sizes of the droplets they studied, coalescence proceeds in the inertial regime and not in a viscous regime. This suggests that the fundamental limitation for small droplets to jump from ultralow adhesion surfaces is most likely due to a combination of a complex droplet-surface interaction mechanism, contact angle hysteresis and viscous effects, and not just the viscous dissipation mechanism as suggested before.

Experimental, theoretical and numerical analyses suggest that the jumping speed is expected to be a non-monotonic function of the size of the droplets. Its maximum is observed to be $\approx 0.25U$ (Mouterde *et al.*, 2017; Boreyko and Chen, 2009; Enright *et al.*, 2014; Liu *et al.*, 2014) for water droplets with $R \approx 100$ μm (Boreyko and Chen, 2009). As mentioned before, coalescence-induced jumping has been observed for water droplets with radii as small as $R \approx 500$ nm ($\mathrm{Oh}_l \approx 0.17$) (Cha *et al.*, 2016). The minimum size of droplets that can jump after coalescence

can further be reduced during multidroplet coalescence (Lv *et al.*, 2015).

Enhancing the jumping speed of the final droplet is crucial for increasing the efficiency of any application that utilizes this particular phenomenon. Gao *et al.* (2018) used molecular dynamics simulations to study the effect of surface textures on the jumping speed of nanodroplets. They found that the jumping speed enhances when the adhesion from the substrate is reduced. This reduction in the adhesive force is achieved either by reducing the magnitude of the attractive force from the surface or by decreasing the solid fraction, which quantifies the actual area over which a droplet is in contact with the underlying textured surface.

Wang *et al.* (2016) studied the self-enhancement of droplet jumping speed based on the interaction of the expanding liquid bridge with a small (compared to R) rectangular groove or a triangular prism. A groove delays the impact of the bridge on the surface and consequently, larger amount of excess surface free energy is spent in order to overcome the viscous dissipation. This results in a reduced jumping speed. On the other hand, with a triangular prism underneath, the accelerated retraction of the droplet base area and the redistribution of the liquid mass result in a higher jumping speed. Wang *et al.* (2016) observed $V_g \approx 0.53U$.

Vahabi *et al.* (2018) used macro-textures (size comparable to R) to enhance the jumping speed. They observed a higher energy conversion efficiency (about 570% increase compared to jumping from surfaces without any textures) resulting from the effective redirection of the in-plane velocity vectors to the out-of-plane direction. Notably, in their experiments, they observed coalescence-induced jumping for droplets with $\mathrm{Oh}_l > 1$ on such surfaces.

Observing sub-micron scale droplets is experimentally challenging and this motivated Liang and Keblinski (2015) to perform MD simulations of coalescence of argon nanodroplets on an atomically smooth superlyophobic surface. They observed jumping for droplets with Oh_l as large as 0.55. When Oh_l is so large, the coalescence process is strongly influenced by dissipative forces and a scaled jumping speed $V_g^* \equiv V_g/U$ is expected to monotonically decrease with Oh_l until no jumping is observed (Enright *et al.*, 2014; Liu *et al.*, 2014; Wang *et al.*, 2011). In stark contrast to this expectation, Liang and Keblinski (2015) observed a constant V_g^* in their study with varying Oh_l, which has so far evaded any explanation.

The role of outer gas in the jumping process is usually neglected in many analyses. Enright *et al.* (2014) neglected the role of drag from the external fluid during the coalescence process in their experimental analysis and simulations, and Peng *et al.* (2013) showed that air friction has negligible influence on jumping due to small jumping speed. Their analyses finished once the droplet lost its contact with the underlying substrate. Farokhirad *et al.* (2015) studied the jumping process using the Lattice Boltzmann method, paying particular attention to the role of density of the outer gas on the aftermath of the coalescence process – i.e. the maximum height of the final droplet jumps. Their results showed that the higher inertia of the outer fluid associated with its large density gave rise to vortices in the outer flow field, which enhanced

the jump heights.

1.2 Open problems and thesis originality

Sprittles and Shikhmurzaev (2012, 2014a) developed a singularity-free model of droplet coalescence called the *interface formation model* in which the interface evolution right after the moment when droplets establish the first contact is modelled by assuming the existence of an 'internal interface'. It takes a finite time for this internal interface to disappear, during which the divergence of pressure, local velocity etc. are taken care of. This model of droplet coalescence is shown to better represent different experimental data than models that host a singularity in the beginning of coalescence (Sprittles and Shikhmurzaev, 2012). Furthermore, the scaling laws used to describe the bridge evolution during droplet coalescence has to be subjected to systematic scrutiny, especially in the early stages of coalescence in order to better understand the role of thermal fluctuations and interatomic interactions in the dynamics. During this time, where experiments and continuum based analysis have limitations in probing the dynamics, the intervening gap between the droplets will be of the order of molecular dimensions and this necessitates the detail of MD simulations.

A similar mathematical singularity exists in many computational models that study droplet spreading on a surface. At the point of first contact between the droplet and the surface, the capillary energy suddenly becomes available at that singular point, which subsequently enable the spreading process. This singularity also arises due to the infinite free-surface curvature at the point of contact. However, this must not be confused with the singularity associated with contact line motion as described in Huh and Scriven (1971) and Dussan (1979) i.e. due to the divergence of stress and energy dissipation close to the three-phase-zone. Although the latter has been dealt with in the literature by suggesting alternative boundary conditions, the physical mechanism by which nature removes the former singularity is still unknown. Since the distance between the droplet interface and the substrate at this initial stage is of the order of a few nanometres, the interfacial thermal fluctuation and other molecular effects may play a significant role in the spreading dynamics, and this also requires systematic investigation.

In studies related to coalescence-induced jumping of droplets, a factor that is usually overlooked is the involvement of ambient gas in the overall dynamics. Besides traditional gas dynamics, coalescence-induced jumping of nanodroplets in an ambient gas could involve other effects such as slip at solid-fluid and fluid-fluid interfaces and thermal fluctuations at interfaces (Rowlinson and Widom, 1982; Werner *et al.*, 1999; Sides *et al.*, 1999; Eggers and Villermaux, 2008; Lucassen *et al.*, 1970). Since the natural length scale involved in the process is of the order of R, and the mean-free-path of the gas molecules is typically of the order of a few 10s of nanometres, the gas flow will be rarefied and involves significant slip. This slip at the interfaces can be crucial to the dynamics of the problem and is sometimes ignored in continuum

simulations; for example, previous phase-field simulations (Liu *et al.*, 2014) of nanodroplets failed to observe the bridge hitting the underlying surface as opposed to what was observed in MD simulations (Liang and Keblinski, 2015). Moreover, a part of this thesis has recently shown that the spatio-temporal fluctuations at the interface – the so called *thermal capillary waves* (Zhao *et al.*, 2019a; Zhang *et al.*, 2019) – make onset of coalescence a stochastic process and that the thermal motion of the molecules crucially affect the initial stages of coalescence (Perumanath *et al.*, 2019). Clearly, modelling nanodroplet coalescence inevitably requires a method which can incorporate such nanoscale affects. By using MD, we can simultaneously capture the spatio-temporal scales associated with rarefied gas flow and thermal fluctuations that are currently beyond experimental capabilities, and understand their influence on nanodroplet jumping.

1.3 Chapter outline

All studies carried out in this thesis employ MD simulations for the investigation of the role of molecular effects on droplet dynamics: coalescence, spreading and coalescence-induced jumping. In Chapter 2, a general introduction to MD simulations, different molecular models used in this thesis and their validations are given. The working procedure of any MD simulation is then explained through a simple example of contact angle measurement.

In Chapter 3, the coalescence of water nanodroplets is investigated in detail using MD. The role of molecular effects is quantified for the first time. Here, (a) the physical mechanism with which the first contact between coalescing nanodroplets establishes and (b) the unique mechanism of the bridge evolution in the early stages are studied. Assisted by a theoretical analysis, this chapter addresses the issue of initial singularity in droplet coalescence and provides a comprehensive picture of the entire process.

Chapter 4 resolves the initial singularity associated with droplet spreading by studying the role of intermolecular attractions between wetting liquid and the substrate on the spreading dynamics. The molecular mechanism of contact line evolution in the initial stage is shown to be completely different from our traditional understanding and this motion is quantified using different techniques.

Chapter 5 investigates the role of gas rarefaction and molecular thermal effects on the coalescence-induced jumping of nanodroplets. It is shown that the nanodroplet jumping is governed not just by the Ohnesorge number as previously thought, but also by two other non-dimensional parameters: Knudsen number and thermal fluctuation number. The effect of new parameters are explained using theoretical analyses.

Finally, Chapter 6 details the thesis conclusions and future directions along which the study presented here can move on to.

Chapter 2

Simulation Details

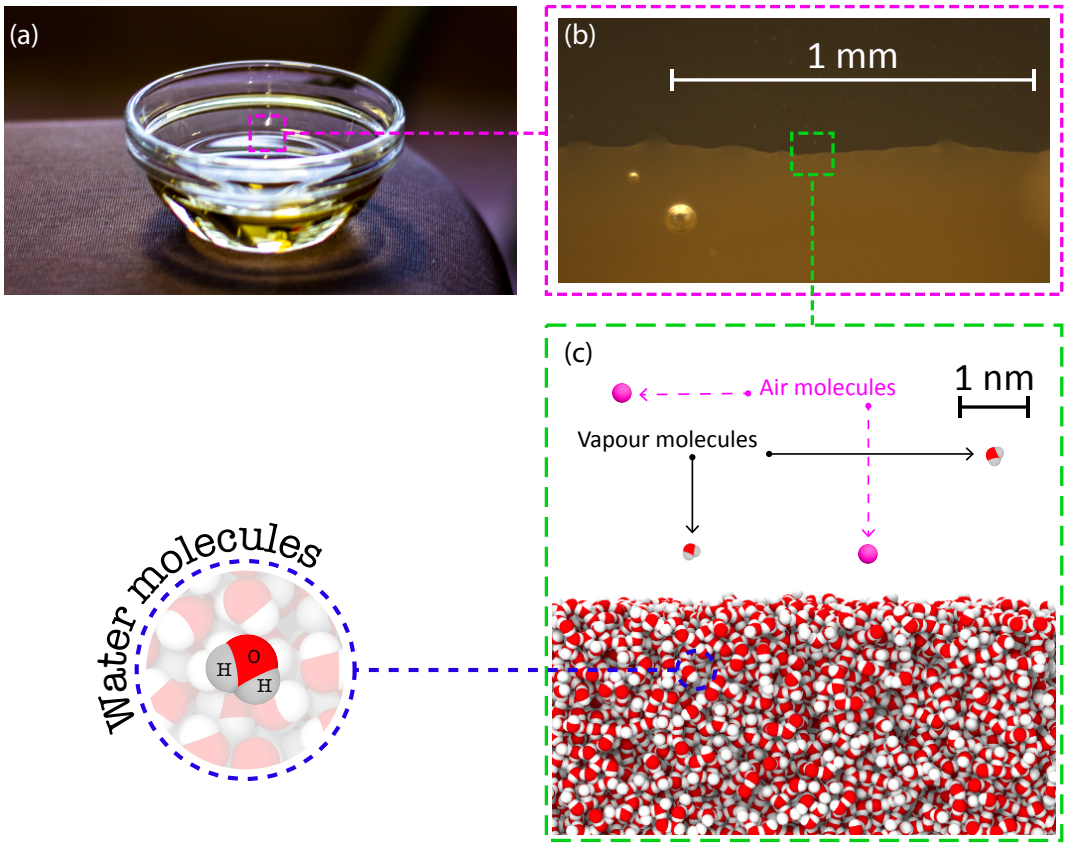

Figure 2.1: The microscopic constituents of a simulation model normally determines the overall macroscopic prediction. In a molecular dynamics simulation, every single molecule in a system is modelled. (a) shows a bowl containing water; a system that we encounter mostly daily in our lives. (b) shows a magnified version of the water-air interface in the bowl. Air bubbles of radii ~ 0.1 mm are also seen. (c) shows an MD simulation snapshot of the same interface. Several vapour molecules are also seen.

In studying and solving engineering problems in fluid dynamics, experiments are frequently used – some examples include: droplet manipulation on special surfaces, wetting/coating, flow through pipes and nanochannels and even for measurement of fluid properties, such as mass

diffusivity, surface tension and viscosity. These experiments have given us tremendous insights into the fundamentals of any problem at hand and have helped us in validating many hypotheses. Many of these experiments involve investigating a system with some probes, assuming that they do not interfere with the inherent system dynamics.

With the growth of powerful computers, researchers have also been studying many of these problems in fluid dynamics with the help of computer simulations. Once the governing equations, boundary and initial conditions are known, any software that can numerically solve a set of equations, can provide many minute details of the system that are otherwise inaccessible through experiments – for example, 3-dimensional flow velocity, pressure, density and temperature fields in a system. The key factor here is that the set of equations that govern these systems are derived under the continuum assumption: any physically measurable quantity must be continuous, finite and should not diverge anywhere in the domain of the problem.

There are many scenarios where the continuum assumption does not hold; mainly those systems where relevant processes happen over very short length and time scales. Flow in micro/nanofluidic devices, thermal fluctuations at interfaces, rarefied gaseous systems and contact line motion can be thought as examples of such systems, that are often challenging to model through traditional computational fluid dynamics (CFD) modelling. Experimental studies of these systems are also highly challenging and require a separate class of computer simulation techniques. Particle-based deterministic simulation tools, such as molecular dynamics (MD), and probability-based stochastic tools, such as direct simulation Monte-Carlo (DSMC) methods that provide solution to the Boltzmann equation, are usually used to study some of these non-continuum systems. In this thesis, MD is exclusively used to study a few engineering flow problems relevant to nanoscale interfacial fluid dynamics.

Through MD simulations, it is possible to obtain full molecular resolution of the system, including their positions and velocities, from which we can evaluate many system parameters. Since its introduction, molecular dynamics simulations have been used to study systems pertaining to widely different applications: how a liquid wets a solid surface (Blake *et al.*, 1997), the relationship between structure and function of bio-macromolecules (Dror *et al.*, 2012) and to address geological radio-active waste disposal issues (Ma *et al.*, 2019). In this chapter, the basic simulation methodology employed throughout this thesis is discussed. The free, open-source and highly parallelised MD simulation software LAMMPS (Large-scale Atomic/Molecular Massively Parallel Simulator) (Plimpton, 1995) is used for all molecular simulations in this thesis.

This chapter is (a) intended to verify various MD models that have been used in this thesis; a crucial part of any computational study and (b) to provide details to a newly starting PhD student or anyone wishing to use MD by taking them through what I think are important procedures to consider, which do not merit that much fine detail in journal publication. This chapter begins with a general description of molecular dynamics simulations, how it works

and a discussion about evaluating different properties. Since water is employed as the main working fluid in all the simulations, two computational models of water: TIP4P/2005 and the mW model are discussed in detail and are validated against experiments of water in Sections 2 and 3, respectively. In some systems, the effect of an ambient gas on nanodroplet dynamics is studied using a mono-atomic model of nitrogen, which is introduced and validated in Section 4. Finally, Section 5 discusses the basic working procedure of any molecular dynamics simulation carried out in this work by demonstrating a case for measuring contact angle of a droplet on atomically smooth surfaces.

2.1 Molecular dynamics

Molecular dynamics is a particle simulation tool in which the time evolution of a set of interacting particles is carried out by integrating their equations of motion (Allen and Tildesley, 2017). This requires force evaluations and updating the positions and velocities of these particles in discrete timesteps. In the absence of any external force fields – such as electric or gravitational – the force acting on any particle i in a system of N particles is given by the gradient of the potential energy function with respect to molecular positions:

$$\vec{F}_i = -\nabla_i \forall(\vec{r}_1, ..., \vec{r}_N), \tag{2.1}$$

where $\vec{F}_i$ is the force acting on the i^{th} particle due to it being in the potential energy field ($\forall$) generated by the presence of the rest of the $N-1$ particles in the system and ∇_i is the gradient operator with respect to the position of i^{th} particle.

The evaluated force on each particle is then used to time-march the particles forward in time and space according to Newton's laws of motion:

$$\vec{F}_i = m_i \vec{a}_i, \tag{2.2}$$

where $\vec{a}_i = d^2\vec{r}_i/dt^2 = d\vec{v}_i/dt$ is the acceleration of that particle. MD is a completely deterministic approach: given the configuration of a system at any instant of time, one can determine its configuration at any other instant in its past or future. For such a *conservative system*, the total energy (TE), which constitutes both global potential (PE) and kinetic (KE) energies, remains invariant in time. Correspondingly, the configuration of a system containing N particles will traverse a constant TE surface in a $6N$-dimensional ($3N$ positions and $3N$ momenta) phase space.

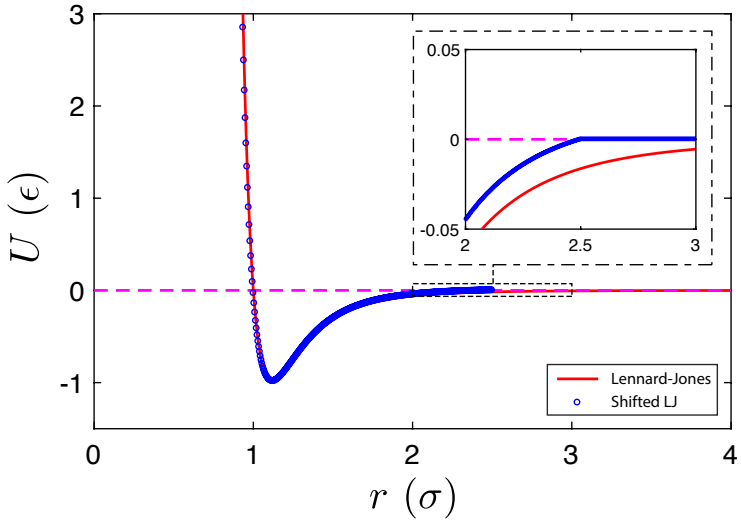

Figure 2.2: The Lennard-Jones (LJ) potential and the 'shifted LJ potential', shifted to zero at 2.5σ for a species with $\varepsilon = 1$ and $\sigma = 1$. The potentials are spherically symmetric and so depends only on the separation between any two atoms r. The inset shows magnified potential near $r = 2.5\sigma$.

2.1.1 Interaction potentials

The choice of the interaction potential V, which is translationally invariant, determines the characteristics of the system at hand. For example, V can be a two-body potential: $V = V(\vec{r}_i, \vec{r}_j)$, which is appropriate for simple systems, such as argon, or it can be a complicated many-body potential: $V = V(\vec{r}_i, \vec{r}_j, \vec{r}_k)$, which is commonly used to model semiconductor systems, such as silicon.

Two-body potentials are, perhaps, the most widely used interaction potentials in molecular simulations. Among them, the Lennard-Jones potential may be the most popular one. This potential is spherically symmetric, repulsive at short distances and attractive at long distances. Mathematically, it is represented by

$$V_{LJ} = U_{ij}(r; \varepsilon_{ij}, \sigma_{ij}) = 4\varepsilon_{ij}\left[\left(\frac{\sigma_{ij}}{r}\right)^{12} - \left(\frac{\sigma_{ij}}{r}\right)^{6}\right], \tag{2.3}$$

where ε_{ij} is the energy parameter that quantifies the strength of the interaction between the two interacting particles i and j, σ_{ij} is the zero-crossing distance for the potential and $r = |\vec{r}_{ij}| = |\vec{r}_i - \vec{r}_j|$ is the separation distance between them. Figure 2.2 shows V_{LJ} as a function of the separation distance (r) between two particles for a special case where $\varepsilon_{ij} = 1$ (in energy units) and $\sigma_{ij} = 1$ (in distance units). While the attractive nature of V_{LJ} at long distances arises due to van der Waals forces because of dipole-dipole interactions, the strong repulsion at short distances arises due to overlapping electron clouds as the atoms approach each other (i.e. due to Pauli's exclusion principle). This potential is thoroughly validated for many physical systems,

particularly containing inert gases like argon, krypton and xenon.

In reality, Eq. (2.3) is boundless and in a simulation box of finite size with periodic boundaries (see below), a particle will interact with itself and this will drastically affect the simulation predictions as well as the scalability of the system. This problem is usually solved by truncating the potential at a specified distance, essentially neglecting any intermolecular interactions above that distance. This *cut-off* distance r_c is optimally chosen such that any smaller value will result in changes of the system's microscopic behaviour that leads to changes in it's macroscopic behaviour (such as surface tension, viscosity etc.), while any larger value of r_c will result in the same microscopic/macroscopic physics, but with an unnecessarily large computational cost. Apart from truncating at r_c, the LJ potential is also shifted to eliminate the energy discontinuity at $r = r_c$, and given by:

$$U_{ij}(r;\varepsilon_{ij},\sigma_{ij},r_c) = \begin{cases} 4\varepsilon_{ij}\left[\left(\frac{\sigma_{ij}}{r_{ij}}\right)^{12} - \left(\frac{\sigma_{ij}}{r_{ij}}\right)^{6} - \left(\frac{\sigma_{ij}}{r_c}\right)^{12} + \left(\frac{\sigma_{ij}}{r_c}\right)^{6}\right], & r \le r_c, \\ 0, & r > r_c. \end{cases} \tag{2.4}$$

At $r = r_c$, the slope of the above equation (i.e. force) is still not zero and a particle moving in or out or r_c of another particle will suddenly experience a finite force, which can be avoided by smoothing the function in the neighbourhood of r_c. In Fig. 2.2, the above equation is plotted and the inset shows a magnified plot of the region close to where the original potential is truncated. Usually $r_c = 2.5\sigma$ or $r_c = 3.2\sigma$ is employed in the literature.

The force computation of Eq. (2.4) for all particles is by far the most computationally costly step in the MD algorithm. The truncation step allows molecules to interact only with their neighbours. In the MD implementation, a neighbour list is utilised, which produces for each atom a list to neighbouring atoms to identify the unique pairs. The neighbour list is built every few timesteps to save in the computational cost, and considers all molecules within a radius of $r_c + d_{\text{skin}}$, where d_{skin} is a small buffer value which allows the capacity for molecules to leave or enter r_c within the allocated time of list rebuild. Usually d_{skin} is taken as a small fraction of the molecular size σ. The larger the skin distance, the less often do we have to update the neighbour list and this may result in a higher computational efficiency.

2.1.2 Periodic boundary conditions

Periodic boundary conditions (PBCs) are the most commonly used boundary conditions in MD, as they allow mass, linear momentum and energy conservation, in line with MD practices. While implementing PBCs, the simulation box is replicated in all directions (see Fig. 2.3(b)) from the central simulation box and consequently several molecules close to the boundary may have neighbours located in a few of these replicas. Moreover, when a particle crosses one of the boundaries with a particular velocity, it is re-inserted into the central box with the same velocity, but from the opposite side. This can be thought of as another particle entering the

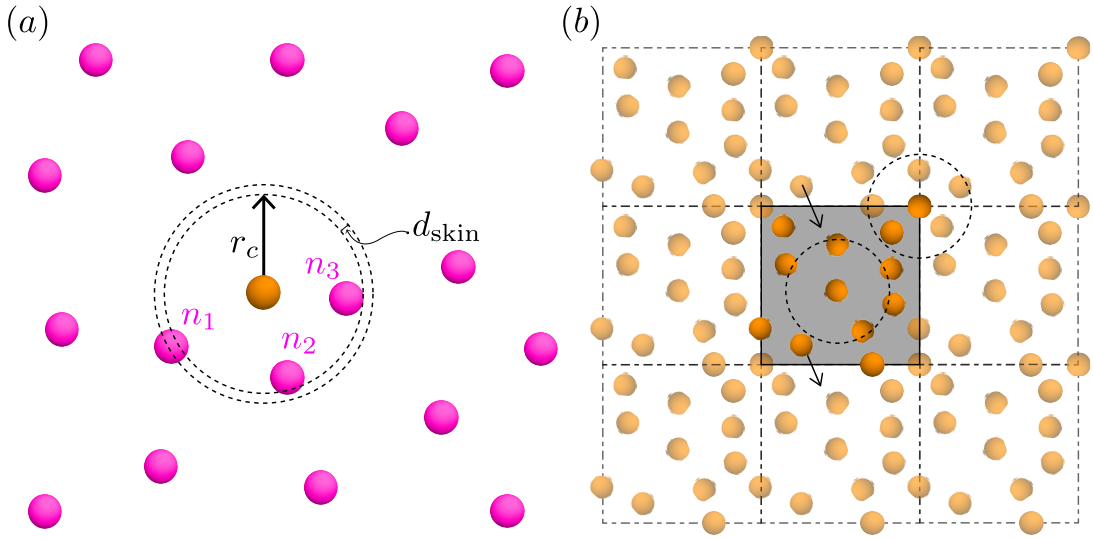

Figure 2.3: (a) All atoms within a distance of $r_c + d_{\text{skin}}$ from the central atom are considered to be its neighbours. (b) Periodic boundary conditions. The central simulation box is replicated in all directions while identifying the neighbours for each atom. An atom can have neighbours lying in the same box or lying in many other boxes. When an atom crosses over a boundary with a particular velocity (depicted by the arrows), its image from the other side enters the central box with the same velocity, thereby keeping the number of atoms constant at any instant of time.

central simulation box from one of its replicas.

It must also be noted that the separation between opposing periodic boundaries of the simulation domain must be at least greater than twice the cut-off distance employed in the simulation. Otherwise, particles will interact with more than one periodic images of itself, creating spurious effects known as finite-size effects (Rapaport, 2004). The sizes of all domains used in this thesis are always larger than $3r_c$.

2.1.3 Time integration

For the implementation of MD, many finite-difference based algorithms exist for the time integration of the system: velocity-Verlet, Leap-frog and predictor-corrector. Starting from a particular instant in time t, these algorithms allow us to determine the configuration of the system at a later instant of time $t + \Delta t$, where Δt is the timestep. Fig. 2.4 shows the collision of two molecules in an MD simulation and the corresponding variation of their potential energy. The velocity-Verlet algorithm is used for simulating any system presented in this thesis. Here, the positions and velocities of atoms are updated as follows:

$$\vec{r}(t+\Delta t) = \vec{r}(t) + \vec{v}(t)\Delta t + (1/2)\vec{a}(t)\Delta t^2, \tag{2.5}$$

$$\vec{v}(t+\Delta t/2) = \vec{v}(t) + (1/2)\vec{a}(t)\Delta t, \tag{2.6}$$

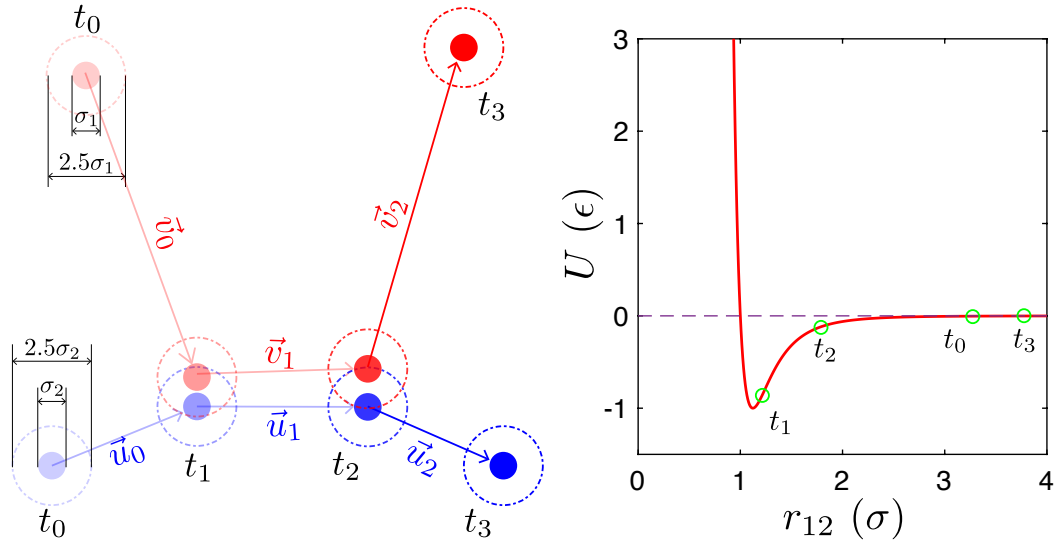

Figure 2.4: Trajectory of two atoms undergoing a collision. The heavier atom (say blue) undergoes less deviation from its original trajectory. The collision can happen over a finite interval, i.e. the atoms may remain in contact for a finite amount of time (from t_1 till t_2 in the figure). The potential energy of the system is shown on the right side at different times.

$$\vec{a}(t+\Delta t) = -(1/m)\nabla_i \forall(\vec{r}(t+\Delta t), \tag{2.7}$$

$$\vec{v}(t+\Delta t) = \vec{v}(t+\Delta t/2) + (1/2)\vec{a}(t+\Delta t)\Delta t. \tag{2.8}$$

The size of the timestep used in the above equation determines the stability a simulation and accuracy of these equations. Usage of a large value of Δt may result in atoms moving unphysically large distances from its neighbours; this is particularly adverse when the distance between any two atoms are to be kept constant — for example, if there exists a bond of fixed length between these atoms. There is an optimum range of values of the timestep for each system that minimizes computational costs and, at the same time, will not result in blowing up the entire simulation. In all the simulations presented in this thesis, a timestep size of a few femto-seconds are used.

2.1.4 Thermodynamic quantities

Molecular simulations give the microscopic details of a system, such as the positions, velocities and forces on each atom in the system. These microscopic details are of little to no use at large scales, where researchers are more interested in the thermodynamic properties of a system, such as temperature and pressure. From first principles of molecular simulations, and with the help of statistics, a link can be made between the microscopic details of a system and its corresponding macroscopic observables. These thermodynamic physical quantities are usually functions of atomic positions and velocities. Measurements of several such quantities are discussed below.

Temperature— The temperature of a system is directly related to the kinetic energy of all the

particles present in the simulation. If $3N$ is the number of degrees of freedom (which is the case, if the particles are simple spheres), the equipartition theorem suggests that each degree of freedom contributes $(1/2)k_BT$ to the total kinetic energy; i.e.

$$3N\frac{k_BT(t)}{2} = \frac{1}{2}\sum_i m_i|\vec{v}_i(t)|^2, \tag{2.9}$$

where $k_B = 1.38 \times 10^{-23}$ J/K is the Boltzmann constant. Rearranging gives the instantaneous temperature

$$T(t) = \frac{1}{2}\sum_i \frac{2m_i|\vec{v}_i(t)|^2}{3Nk_B}. \tag{2.10}$$

Note that, when there is a flow with a mean velocity, the velocity term in Eq. (2.10) becomes $|\vec{v}_i(t) - \vec{v}_m(t)|$, where $\vec{v}_m(t)$ is the instantaneous mean velocity.

Pressure— The measurement of pressure in MD is based on the virial equation

$$PV = Nk_BT + \frac{1}{D_m}\left\langle \sum_{i=1}^{N} \vec{r}_i \cdot \vec{F}_i \right\rangle, \tag{2.11}$$

where D_m is the dimensionality of the system, $\vec{F}$ is the total force on particle i, V is the the control volume and $\langle \cdots \rangle$ denotes ensemble average (see below). Here, $\vec{F}_i$ is evaluated by using Eq. (2.1). It must be noted that the above equation reduces to the ideal gas equation when the particles are non-interacting. The above equation assumes that the interaction potential is not cut off at any finite length scales.

For a system with particles interacting through pair potentials, the above equation in a principal direction (say x) reduces to

$$P_{xx}V = \sum_i m_i v_{xi}^2 + \sum_i \sum_{j>i} r_{xij} f_{xij}, \tag{2.12}$$

where f_x is the x component of the force acting between particles i and j and the second summation is performed such that any particle-particle pair is counted only once. The local pressure inside any small control volume in the domain can be evaluated by taking the average of all three equations similar to Eq. (2.12) over all atoms present in that control volume.

Since the LJ interaction potential is cut-off and shifted at r_c, the pressure evaluated using the above equations will not be the exact value of the pressure in the system. As long as the radial distribution function (see below) is roughly invariant above r_c, a 'tail correction' term can be derived that has to be added to these equations to obtain the real value of pressure:

$$P_{\text{tail}} = \frac{16\pi N^2}{3V^2}\varepsilon\sigma^3\left[\frac{2}{3}\left(\frac{\sigma}{r_c}\right)^9 - \left(\frac{\sigma}{r_c}\right)^3\right]. \tag{2.13}$$

Since all the simulations presented in this thesis, where there is an outer gas, are relatively rarefied (Knudsen number $\lesssim 1$), the tail correction term is less than 10% of the value determined from Eq. 2.11.

Similarly, the shear stress can be obtained by

$$\tau_{xy}V = \sum_i m_i v_{xi} v_{yi} + \sum_i \sum_{j>i} r_{xij} f_{yij}. \tag{2.14}$$

The above expression will be used later to evaluate the viscosity of the working fluids.

2.1.5 Ensembles

A thermodynamic system can exist in different states subjected to several conditions. At one end, it cannot exchange either mass or energy (isolated system) and at the other end, it can exchange both with surroundings (open system). Subjected to any set of conditions, the system state traverses different surfaces in its $6N$-dimensional phase space. The collection of all such possible system states is called an *ensemble*. Often, an ensemble average is used to determine different properties of the system from the principles of statistical mechanics (Allen and Tildesley, 2017). In other words, an ensemble represents a collection of all system states with different microscopic states, but identical macroscopic/thermodynamic state.

Microcanonical ensemble— An isolated system is represented by a microcanonical ensemble. For such a system, the total number of particles (N), its volume (V) and its total energy (E) are invariants, and therefore is called an NVE ensemble. Here, the system state will traverse a constant energy surface in its phase space. Examples of systems that are depicted by this ensemble are droplet coalescence and spreading that are central to this thesis. In both cases, once the initial configuration is set, the total energy within the system is contained and is redistributed among the particles during the process.

Canonical ensemble— In a canonical ensemble, the system is coupled to a heat bath such that its temperature (T) remains constant, where the heat bath is much larger in its capacity than the system. This ensemble represents a system that is in thermal equilibrium with its surroundings.

Other ensembles exist such as *the grand canonical ensemble*, which describes an open system and *the isothermal-isobaric ensemble*, which describes a system undergoing a thermodynamic process under constant temperature and pressure.

Throughout this thesis, a canonical ensemble is employed while equilibrating different systems at a desired temperature. For fair control of system temperature, a thermostat must be applied to bring any system to the desired temperature. It is then turned off during the main MD run, thereby switching to a microcanonical ensemble.

2.1.6 Berendsen thermostat

For controlling the temperature of any system studied in this thesis, a Berendsen thermostat is used. This thermostat controls the temperature of a given group of atoms by rescaling their velocities.

Suppose the current temperature of the system is T and the target temperature is T_0, the Berendsen thermostat will scale the momenta of the associated particles by a factor λ_s given by

$$\lambda_s = \sqrt{1 + \frac{\Delta t}{\tau_T}\left(\frac{T_0}{T} - 1\right)}, \tag{2.15}$$

where τ_T is the coupling parameter that determines the time scale over which the target temperature is achieved. LAMMPS recommends using $\tau_T \approx 50\Delta t - 100\Delta t$ in MD simulations and it is followed throughout this thesis.

2.1.7 Limitations of MD

Molecular dynamics simulations do not make any assumptions about matter being continuum, and the thermophysical properties of the material being studied and the thermodynamic quantities of the system will come out as emergent quantities from these simulations. Nevertheless, like any other simulation tool, MD is also burdened with its own limitations.

Perhaps, the most important of these limitations is the fact that MD simulations are computationally expensive, as it models every single atom in a system. This puts a cap on the maximum size of the system, particularly in terms of the total number of atoms. This limitation stems from the fact that for every system with N number of particles, the number of corresponding pairwise computations at each timestep scales as N^2. For systems with other type of interactions, additional computations will be required. To put this in perspective, a water droplet of radius 1 mm contains roughly $\sim 10^{21}$ molecules (so $\sim 3 \times 10^{21}$ atoms) in it and the largest MD simulation so far has only been able to simulate only 100 million atoms.

Another limitation is that typically many interaction parameters are required to model a realistic system, such as water. These parameters are usually calibrated based on experimental evidences on certain properties of these systems. For example, the energy parameter in the LJ potential can be varied until any of the properties of the model matches with that of the real system within an expected margin of error. However, this might cause other properties of the model to shift considerably away from those of a realistic system. With the advent of high-power computers, quantum mechanical calculations are often employed to determine these parameters from first principles. Development of accurate interaction potentials among atoms, by itself, is a dedicated and important inter-disciplinary research area that includes artificial intelligence, quantum mechanics, big data and statistics.

With these limitations, the size of the largest system that can be simulated using MD on even

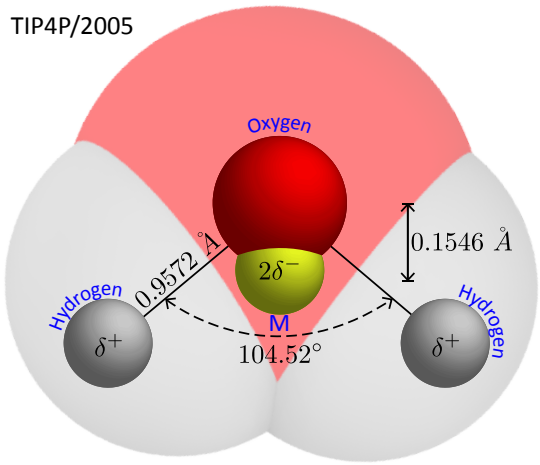

Figure 2.5: The TIP4P/2005 water molecule (not to scale). Each molecule consists of one oxygen atom (mass = 15.9994 g/mol), two hydrogen atoms (mass 1.008 g/mol each) and a massless charged site 'M'. The partial charges are: $\delta^+ = +0.5564e$ and $2\delta^- = -1.1128e$, where $e = 1.602 \times 10^{-19}$ C is the electronic charge. The image in the background is sometimes used in this thesis to represent TIP4P/2005 molecules.

today's supercomputers are only $\sim$ 100 nm, and the longest these simulations can be studied are only for $\sim$ 100 ns. Several of the simulations presented in this thesis were run for days, if not weeks on ARCHER, the UK's national supercomputer using 100s of cores. This demands exceptional care while setting up any MD simulation. Any error in the simulation that shows itself at the end would mean that the entire simulation will have to be run again and would incur a high cost in terms of power and time.

2.2 All-atom model of water – TIP4P/2005

Apart form its biological applications, water is one of the most widely used engineering fluids (Watson *et al.*, 2011; Miljkovic *et al.*, 2012; Wisdom *et al.*, 2013). Several 'all-atom' molecular models of water exist in the literature: SPC/e (Berendsen *et al.*, 1987), TIP3P (Jorgensen *et al.*, 1983), TIP4P/2005 (Abascal and Vega, 2005; Vega and de Miguel, 2007) and TIP5P (Zhao *et al.*, 2019b).

The TIP4P/2005 is an accurate and widely used model. Figure 2.5 shows the detailed atomic structure of this molecular model. There are four sites in this model of water: one charge-less oxygen (O), two positively charged hydrogen atoms (H) and a massless negatively charged site (M) located along the HOH angular bisector below the oxygen atom. The bond, angle and partial charges of different sites of this model are parametrised so as to match its thermo-physical properties to those of real water. In this model, the effective potential between any two atoms j and k is a combination of the shifted Lennard-Jones potential and electrostatic

Coulombic interaction, given by

$$U_{jk} = 4\varepsilon_{jk}\left[\left(\frac{\sigma_{jk}}{r_{jk}}\right)^{12} - \left(\frac{\sigma_{jk}}{r_{jk}}\right)^{6} - \left(\frac{\sigma_{jk}}{r_c}\right)^{12} + \left(\frac{\sigma_{jk}}{r_c}\right)^{6}\right] + \frac{1}{4\pi\varepsilon_0}\frac{q_j q_k}{r_{jk}}, \tag{2.16}$$

where ε_{jk} is the van der Waals interaction energy between the oxygen atoms, σ_{jk} is the length parameter, r_{jk} is the distance between the atoms, q_j is the charge on atom j, ε_0 is the permittivity of the vacuum, and $r_c = 1.3$ nm is the cut-off distance used. This value of r_c is typical in the literature for liquid-vapour systems (Vega and de Miguel, 2007). The hydrogen atoms have only electrostatic interactions with other atoms in the model. The long-range electrostatic Coulombic interactions are included in the model by using a particle-particle particle-mesh (PPPM) algorithm (Hockney and Eastwood, 1988). Here, the interactions outside a specified distance (d_k) are computed in the (inverse) K-space for computational efficiency. The PPPM method maps the charges on each atom to a 3-dimensional mesh and then uses a 3-dimensional fast Fourier transform (FFT) to solve Poisson's equation on that mesh. The final computed values of the forces are then linked back to each atom. The simulation parameters used while simulating any system with the TIP4P/2005 model in this work is given in the table below.

Parameter	Value
ε	0.1852 kcal/mol
σ	0.315 nm
r_c	1.3 nm
Δt	0.002 ps
τ_T	0.2 ps
Output	every 0.02 ps
d_k	0.85 nm

Apart from evaluating thermodynamic quantities using different atom attributes during a simulation, these can be used to evaluate thermophysical properties of any matter using the principles of statistical thermodynamics. Here, these properties of TIP4P/2005 water are evaluated so as to validate it against real water. For such validations, the thermophysical properties of water are either taken from the National Institute of Standards and Technology (NIST), US database or from other experiments. Many of the thermophysical properties of this model deviate slightly ($\sim 10\%$) from that of real water. Such deviations can be primarily attributed to the assumptions made in designing the model, such as the rigidity of the molecule, absence of van der Waals interactions for hydrogen atoms and the fact that this model was originally designed to match the temperature of maximum density of real water ($\approx 4^{\circ}$C). It is necessary to perform such validation studies before using a model to study any system.

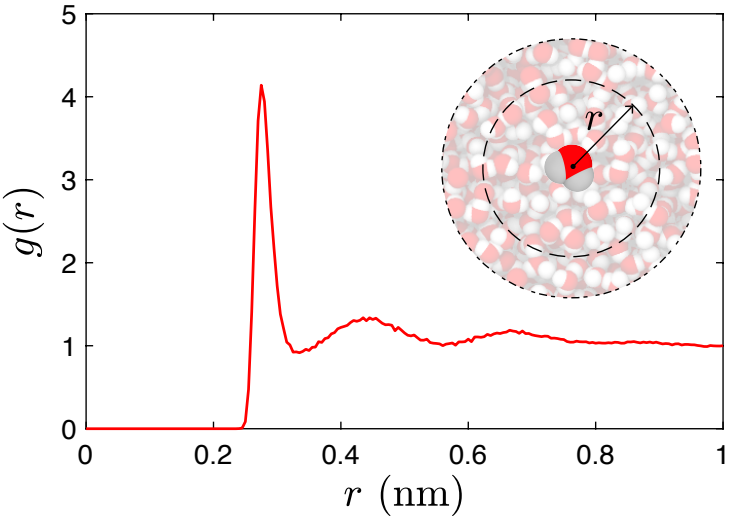

Figure 2.6: Radial distribution function (in arbitrary units) of oxygen atoms in a bulk system of TIP4P/2005 water molecules, depicting the probability of finding a neighbour at a distance r from the central molecule. There exists only short-range order.

2.2.1 Radial distribution function

In a bulk system of water, each molecule is surrounded by its neighbours and they bombard into each other by virtue of their thermal motion. For any bulk molecule, its neighbours are not uniformly distributed around its centre-of-mass. But instead, in liquid systems, there exist short-range order around any molecule. That is, it is more probable to find other molecules near to a given central molecule than it is to find another molecule far from it. This probability is mathematically quantified using the radial distribution function (RDF) $g(r)$, where r is the radial distance of a neighbour molecule from the central molecule. Figure 2.6 shows the RDF of TIP4P/2005 molecules, which is obtained by simulating 33,400 molecules in a box of $(L_x,\ L_y,\ L_z)$ = (10 nm, 10 nm, 10 nm) equilibrated for 1 ns. Far from any central molecule, it is equally probable to find neighbours as indicated by the invariance of $g(r)$ with r. Near to the central molecule, its neighbours cluster in shells of different sizes. This clustering results from a competition of the short-range repulsive and the long-range attractive interactions among the molecules. The locations of various peaks and their relative heights observed in the present study correspond well with those in Camisasca *et al.* (2019); Schlesinger *et al.* (2016), where researchers have compared RDF of different molecular models of water with experimental data.

The RDF can be used to evaluate the number of neighbours (n) a central atom has within a given distance r_c:

$$n = n_v \int_0^{r_c} 4\pi r^2 dr\, g(r), \tag{2.17}$$

where $n_v = N/V$ is the average number density of the liquid of interest and N is the total number of molecules in a system of volume V.

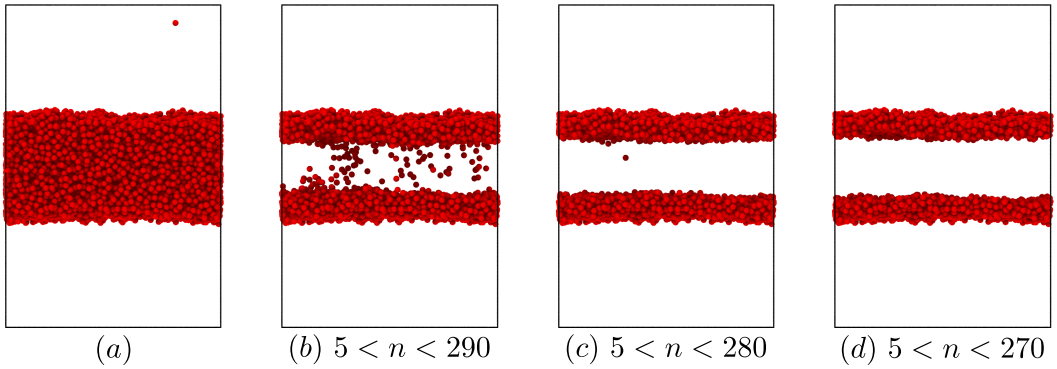

Figure 2.7: Identifying the interfacial molecules based on number of neighbours. (a) the water slab geometry used here. (b-d) The optimum criterion is determined by trial and error, by systematically changing the upper limit until only molecules at the interface are recognised. The lower limit ($n > 5$) excludes all vapour molecules. In the figure, only oxygen atoms are shown.

The number of neighbours determined in the way described above can be used as a parameter to identify interfacial molecules in a system, which can, in turn, be used to evaluate the surface area of a complex deforming liquid body required in this work. From simulations of bulk systems, it is observed that a bulk water molecule will have roughly 310 neighbours within a sphere of radius $r_c = 1.3$ nm, while an interfacial molecule will have fewer neighbours. Furthermore, vapour molecules will have nearly no neighbours (except when a collision occurs).

Here, a slab of TIP4P/2005 water molecules is simulated (Fig. 2.7(a)) and the interfacial molecules are identified through trial and error. A lower bound of $n > 5$ excludes all vapour molecules in the system. The upper bound is gradually decreased until no molecules in the bulk are identified. As shown in Fig. 2.7(b-d), a higher value of the upper limit wrongly identifies some bulk molecules as interfacial molecules. Because of thermal motion of molecules, even the bulk molecules may momentarily have fewer number of neighbours than their average value.

2.2.2 Diffusion coefficient

The diffusion coefficient D usually depends on the pressure, temperature and the size of the diffusing molecules. In molecular simulations, where a system of particles undergoes Brownian motion, the diffusion coefficient is related to the mean-squared displacement (MSD) of the diffusing molecules by Einstein's relation

$$\langle |\vec{x}(t) - \vec{x}_0|^2 \rangle = 6Dt, \tag{2.18}$$

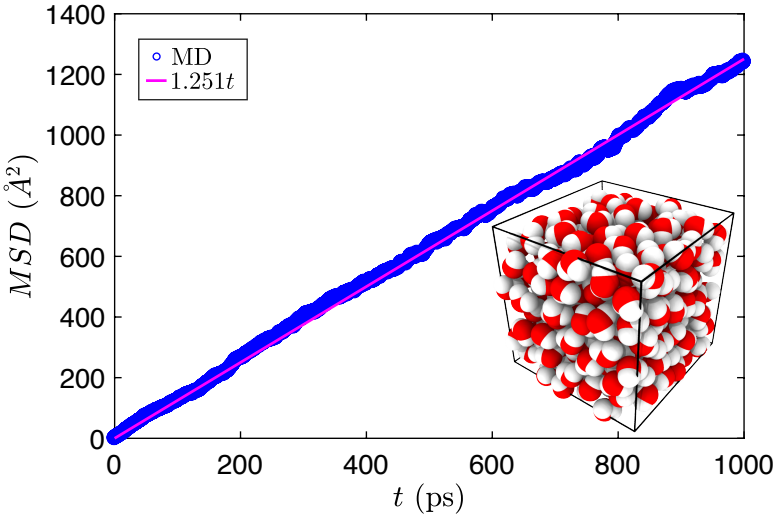

Figure 2.8: Mean-squared displacement (*MSD*) of TIP4P/2005 water molecules as a function of time.

where

$$\langle |\vec{x}(t) - \vec{x}_0|^2 \rangle = \frac{1}{N} \sum_{i=1}^{N} |\vec{x}^i(t) - \vec{x}_0^i|^2. \tag{2.19}$$

In other words, the slope of a graph of $\langle |\vec{x}(t) - \vec{x}_0|^2 \rangle$ versus time t is six times the diffusion coefficient of those species when they are in equilibrium. Figure 2.8 shows the *MSD* of TIP4P/2005 water molecules in equilibrium in a system containing 300 molecules (see inset of the Figure) at $T = 300$ K, which gives $D = 0.0021$ nm^2/ps and is fairly close to the experimentally observed value of 0.0023 nm^2/ps. The deviation can be attributed to the assumptions made while designing the TIP4P/2005 model.

2.2.3 Surface tension

The interfacial tension of an interface is the tangential force per unit length experienced by an imaginary line lying at the interface between any two phases. It can also be defined as the extra energy per unit area (e_A) possessed by molecules near any interface by virtue of them having fewer number of neighbours compared to the ones in the bulk. For determining the interfacial tension γ of the water-vapour interface from MD simulations, a slab containing 16,500 water molecules is simulated, as shown in Fig. 2.9(a). In this system, the interfacial tension can be evaluated as the integration of the imbalance of tangential and normal pressures from the bulk of one phase (liquid) to that of the other (vapour) along the direction normal to the interface y:

$$\gamma_{12} = \int P_N(y) - P_T(y)\, dy, \tag{2.20}$$

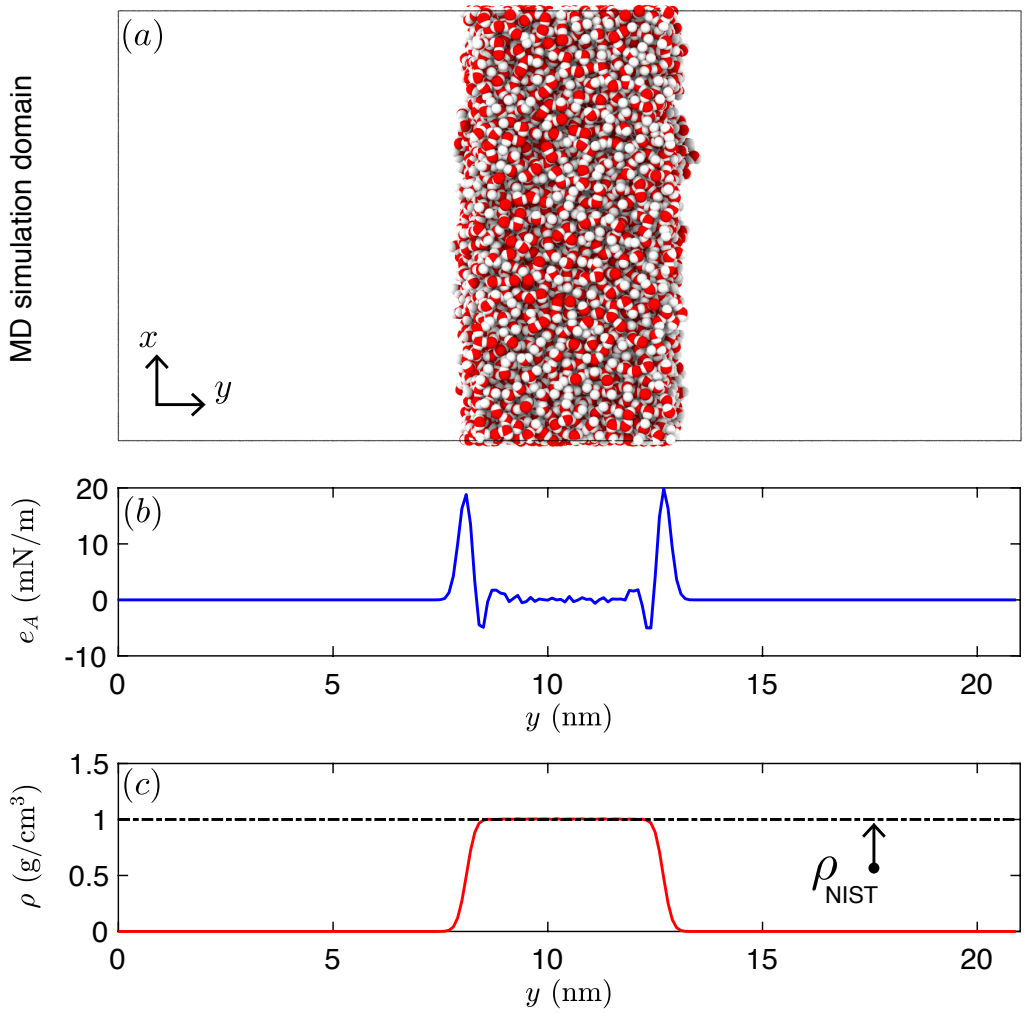

Figure 2.9: Determining the surface tension of water. (a) The water slab geometry used in the MD simulations and (b) time averaged energy per unit cross-sectional area (e_A) as a function of the coordinate normal to the interface (y). e_A at all locations are calculated by dividing the entire domain into several bins along the y direction and integrating the RHS of Eq. 2.20 from one end to the other of a bin. e_A is zero everywhere except at the interfaces, because the interfacial molecules possess some extra energy by virtue of fewer number of neighbours in comparison to bulk molecules. (c) Variation of local density with y. ρ approaches both bulk side densities in a sigmoid fashion. Here, $\rho_{\text{NIST}} = 0.99$ g/cm^3.

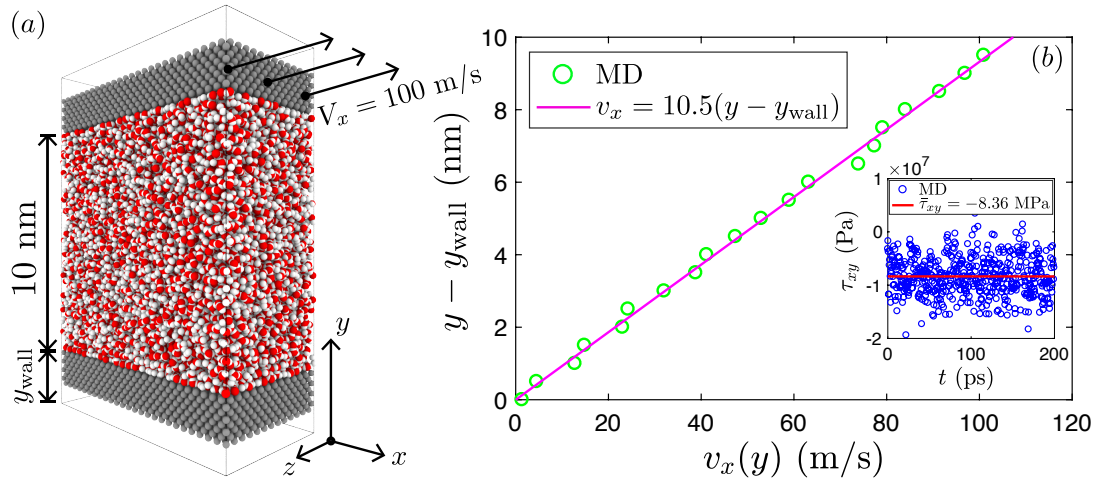

Figure 2.10: Determining the viscosity of water through shearing simulation. (a) Geometry of the simulation domain used. The top wall moves at a steady 100 m/s and the bottom wall is kept stationary. (b) The velocity profile as a function of the distance above the bottom wall in steady state. Inset shows the stress experienced by the entire water molecules over the time of simulation.

where $P_T(y) = (P_{xx}(y) + P_{zz}(y))/2$, $P_N(y) = P_{yy}(y)$. For interacting particles, the pressure components are evaluated from Eq. (2.12). The integration performed above from one location (y_1) to another (y_2) will give the energy per unit area e_A of all the molecules lying between $y_1 < y < y_2$. In Fig. 2.9(b), e_A is plotted as a function of y. It can be seen that e_A is nearly zero in the bulk of both phases, because in the bulk (where the local density is the bulk density; see Fig. 2.9(c)), pressure is isotropic in nature, i.e. $P_{xx} = P_{yy} = P_{zz}$. For such a system of TIP4P/2005 molecules, summing e_A over the entire length ($y_{min} < y < y_{max}$) of the simulation box, gives $2\gamma \approx 130.4$ mN/m (a factor 2 is present, because there are two interfaces). This gives a surface tension of $\gamma \approx 65.2$ mN/m, which is fairly close to the experimental value of 72 mN/m for real water. The deviation can be attributed to the assumptions made while designing the TIP4P/2005 model.

2.2.4 Viscosity

The viscosity of a fluid is a measure of its ability to transfer momentum between adjacent layers in a direction normal to their motion. For evaluating viscosity of TIP4P/2005 water, 16,500 molecules are simulated between the walls of a nanochannel which are 10 nm apart, as shown in Fig. 2.10(a), and is sheared using a Couette flow set-up. Periodic boundary conditions are applied in all three directions. The wall atoms are modelled as hydrophilic in order to avoid liquid slippage as much as possible, but the method will work even if slip exists. The top wall is set at a fixed speed of 100 m/s in $+x$ direction and the bottom wall is fixed to its initial location. Over time, the liquid between the channel will resist shearing and come to a steady state velocity profile as shown in Fig. 2.10(b). The tangential stress (τ_{xy}) experienced by the

entire liquid body can be evaluated from Eq. (2.14) during the simulation time. A Berendsen thermostat is applied to the liquid molecules in the z component of their velocities in order to keep its temperature constant at 300 K. In steady state, a system of Newtonian fluid will satisfy

$$\tau_{xy} = -\mu_l \frac{dv_x}{dy}, \tag{2.21}$$

where μ_l is the viscosity of the medium being sheared. From these simulations, an average value of $\bar{\tau}_{xy} = -8.36$ MPa is obtained (see inset of Fig. 2.10(b)). With $dv_x/dy = 10.5 \times 10^9$ s^{-1}, the viscosity of TIP4P/2005 water is evaluated to be $\mu = 0.8$ mPa-s and is comparable with the experimental value of 0.89 mPa-s.

2.3 Mono-atomic model of water – mW

Although the TIP4P/2005 model of water is fairly accurate, each molecule contains 4 interaction sites and on top of this requires long-range Coulombic interactions to be computed. TIP4P/2005 is therefore a computationally-expensive water model. For this reason, researchers have developed simplified models of water, such as the mono-atomic water (mW), which models water as an intermediate atom between carbon and silicon using the Stillinger-Weber (SW) potential (Molinero and Moore, 2009). The SW potential is a many-body potential developed to model semi-conductor systems involving silicon.

The advantage of using the mW water model in this work is that we can create droplet systems that are many times larger than what is possible with TIP4P/2005 for the same computational cost. This happens not just because of the fewer sites (and therefore fewer interactions and no PPPM interactions), but also because this model can use a far larger timestep. Since this is a single-site model, many of its thermo-physical properties are slightly different from those of more detailed models such as TIP4P/2005, and so below, measurements of these properties will be performed, for use in the theoretical descriptions in this thesis.

Diffusion coefficient.— One of the consequences of mW being a single-site model is that the molecules are able to diffuse through the bulk easier than all-atom models, despite their masses being identical. This is because the energy barrier for each molecule to overcome is less, as there are no explicit hydrogen atoms present in the mW model. It is observed that the MSD is almost 3 times that of actual water (Molinero and Moore, 2009), resulting in a commensurately higher diffusion coefficient.

Surface tension.— For evaluating the surface tension of the mW model, a geometry similar to that given in Fig. 2.9(a) is used. e_A as a function of the coordinate normal to the interface (y) is given in Fig. 2.12(a). e_A is zero in the bulk of both phases and is non-zero only at the interfaces. The surface tension of mW model is found to be ≈ 66.1 mN/m (Molinero and Moore, 2009), which is comparable to that of TIP4P/2005.

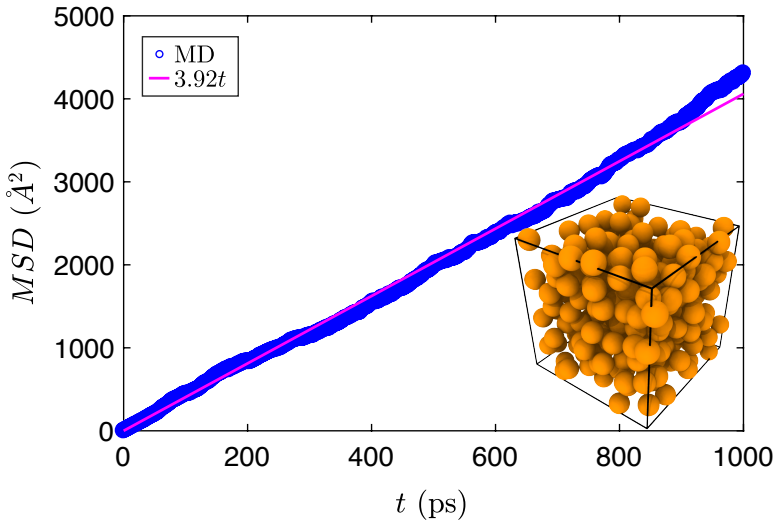

Figure 2.11: MSD of mW water molecules as a function of time. A small simulation box containing roughly 300 molecules is used to evaluate the MSD. Due to the simplicity of the model, the MSD is almost three times as that of TIP4P/2005 molecules, as they can diffuse faster.

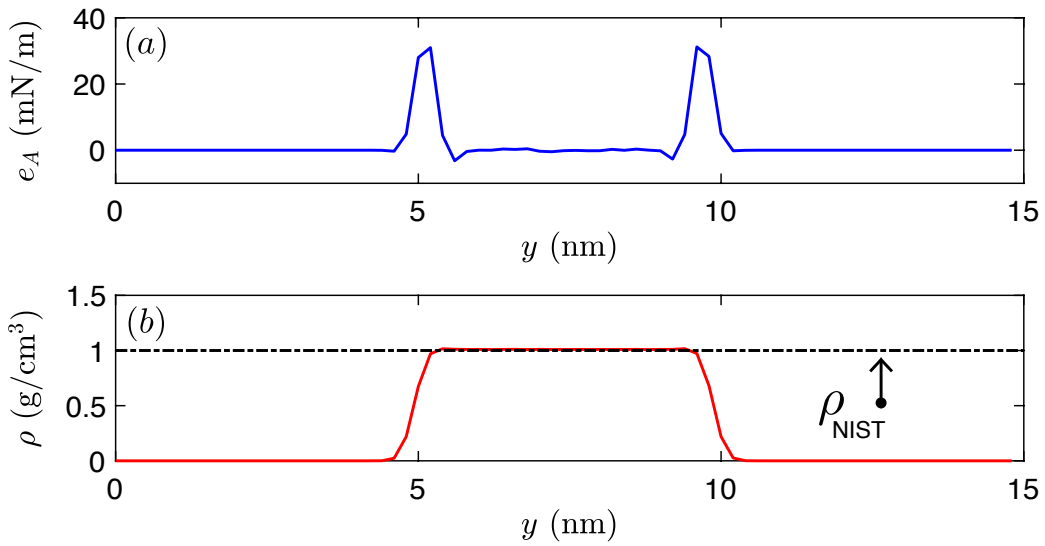

Figure 2.12: Determining the surface tension of mW water. A similar geometry as in Fig. 2.9(a) is used here. (a) The time averaged interfacial energy per unit area (e_A) as a function of the coordinate normal to the interface (y) and (c) the variation of local density with y. Experimental density is $\rho_{\text{NIST}} = 0.99$ g/cm^3.

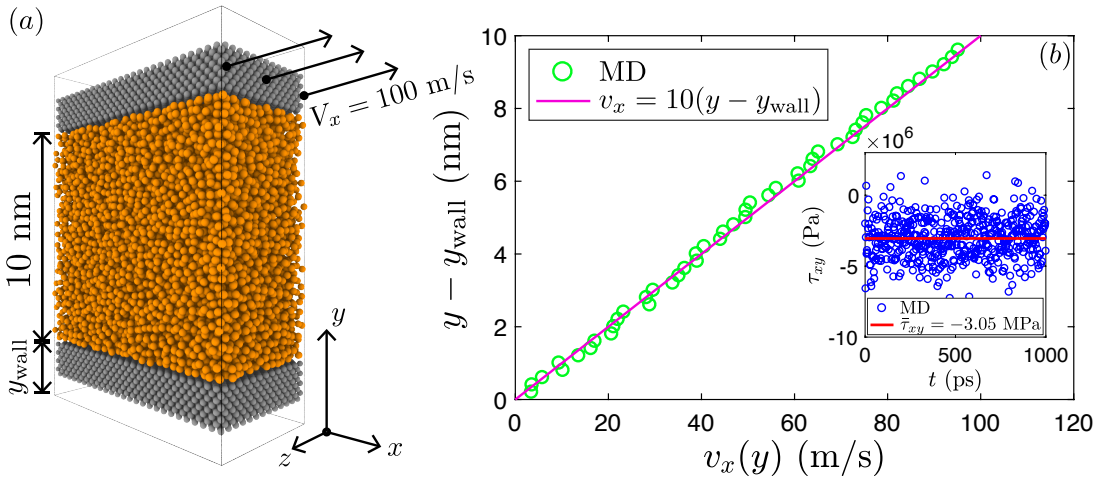

Figure 2.13: A similar geometry as in Fig. 2.10(a) is used here to determine the viscosity of mW water. Inset shows that the stress experienced by mW molecules is only as half as that experienced by TIP4P/2005 molecules in a similar situation. Consequently, mW water has proportionately lower viscosity.

Viscosity.— The viscosity of mW model is evaluated by the shearing method described for TIP4P/2005 model in the previous section. Periodic boundary conditions are applied in all three directions. Because of the simplicity of this model, for the same strain rate, the mW molecules experience only a fraction of the shearing stress experienced by the TIP4P/2005 model. Correspondingly, the viscosity of the model is only $\mu_l = 0.31$ mPa.s (see Fig. 2.13) (Dhabal *et al.*, 2016).

These results show that, despite quantitative changes in some fluid properties, mW and TIP4P/2005 models are qualitatively comparable. Nevertheless, care must be taken while interpreting results that describe same physics. The simulation parameters used while studying any system with the mW model are:

Parameter	Value
Δt	0.01 ps
τ_T	1.0 ps
Output	every 0.02 ps

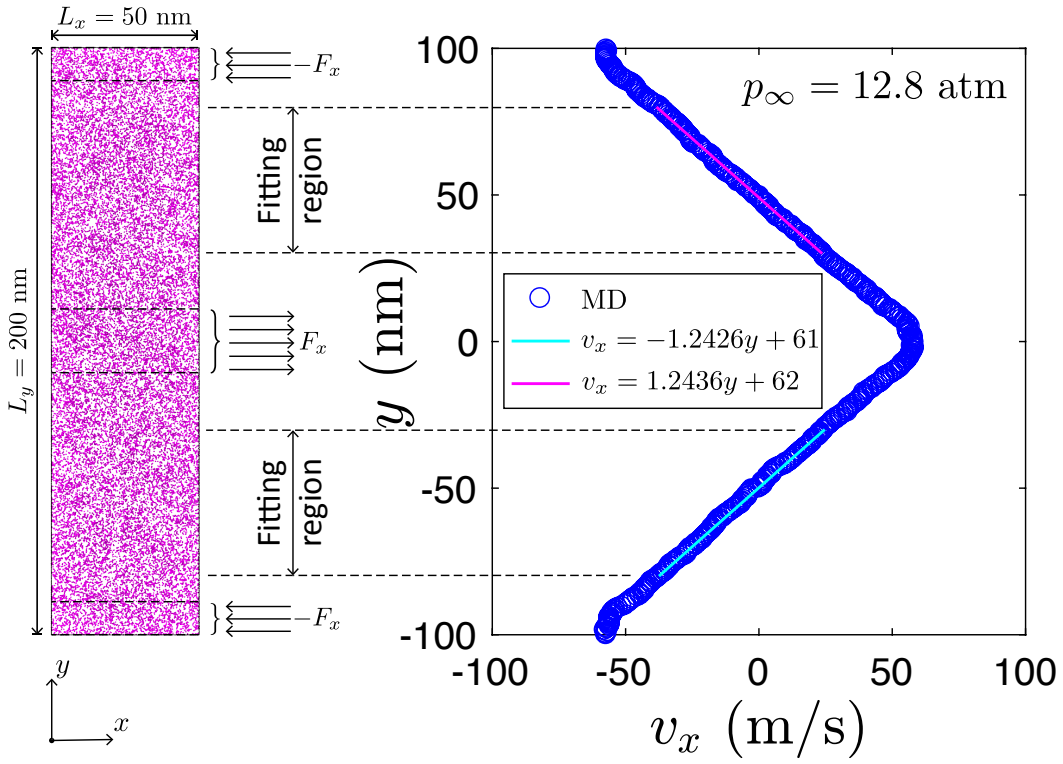

Figure 2.14: Determining the viscosity of nitrogen through modified-shearing simulation. A long square pillar-like geometry is used here. All molecules in the top and bottom regions of the box experience an extra force $-F_x$ in the $-x$ direction and molecules in a central region (twice as big as the former) experience F_x in $+x$ direction. Resulting velocity profile shows velocity is linear in steady state in the fitting region, which is well outside the forcing regions.

2.4 Mono-atomic model of nitrogen

In several chapters of this thesis, a mono-atomic model of nitrogen (at $T = 300$ K) is used to study the effect of an ambient gas on the dynamics of nanodroplets. Although real nitrogen molecules are diatomic in nature, this model is computationally efficient. Here, the interaction between any two nitrogen molecules is defined by a shifted LJ potential (Eq. (2.4)) with $\varepsilon_{NN} = 0.189$ kcal/mol, $\sigma_{NN} = 0.375$ nm and $r_c = 0.94$ nm. In what follows, this model is validated against experimental data on nitrogen obtained from NIST database.

Viscosity.— The main effect of ambient gas outside droplets is to oppose the droplets' motion by virtue of the viscosity of the gas. In this section, the viscosity of the single-site model of nitrogen is tested against corresponding experimental data from NIST. For the determination of viscosity, a long and fully periodic simulation box is set up, as shown in Fig. 2.14. The simulation domain is filled with molecules that match the target thermodynamic state, and is then divided into 5 sub-regions. Three regions are used to apply a steady-state shearing force, and two regions are used to measure the response, from which the viscosity can be calculated. A force of $|F_x| = 3.9 \times 10^{-12}$ N is applied on each molecule in the negative x direction in

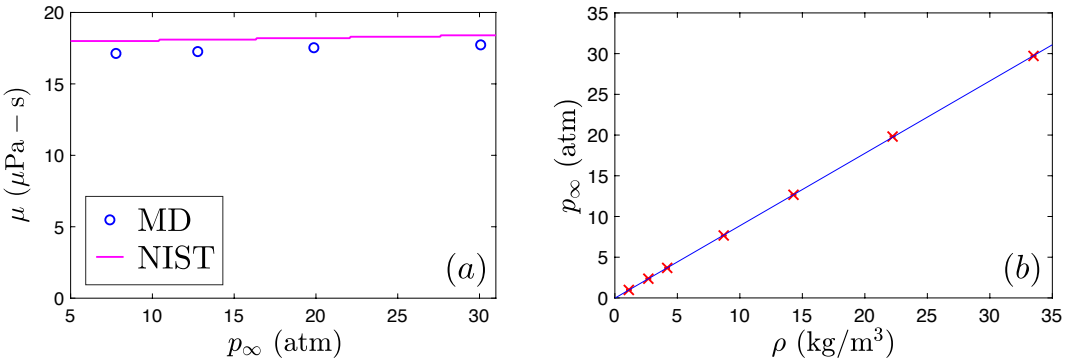

Figure 2.15: (a) Viscosity of nitrogen determined through modified-shearing simulations as a function of bulk pressure compared with that obtained from NIST data base. Viscosity of single-site model of nitrogen is comparable to the NIST values. (b) Ideal gas behaviour of the nitrogen model. The errorbars in p_∞ is smaller than the data points.

the top and bottom forcing regions, and the same magnitude of force is applied on molecules in the central region, but in the positive x direction. Because the top and bottom regions are half the size of the central region, the net force on the system is zero. Unlike the Lees-Edwards boundary condition, where a location dependent velocity is explicitly applied on fluid atoms, applying a body force in the manner described above will ultimately result in a linear velocity profile, as shown in Fig. 2.14. In this 'modified-shearing simulation', where shearing is performed without confining walls, by measuring the shearing stress (τ_{xy}) experienced by all the molecules in the 'fitting region', the viscosity of nitrogen at different pressures can be measured by using Eq. (2.21) (Ramisetti *et al.*, 2017).

The simulation parameters used while studying systems containing nitrogen are:

Parameter	Value
Δt	0.01 ps
τ_T	1.0 ps
Output	every 0.02 ps

It must be noted that for simulations that contain both water and nitrogen in the system, parameters relevant to the water model are used. For example, a timestep size of $\Delta t = 0.002$ ps is used in a system of TIP4P/2005 water droplets coalescing in a nitrogen atmosphere. The viscosity of nitrogen obtained in this manner at different pressures is shown in Fig. 2.15(a). The viscosity matches well with the NIST data at 300 K at higher pressures. Figure 2.15(b) shows the pressure-density graph at $T = 300$ K. The mono-atomic model of nitrogen behaves nearly as an ideal gas in the range of pressures investigated.

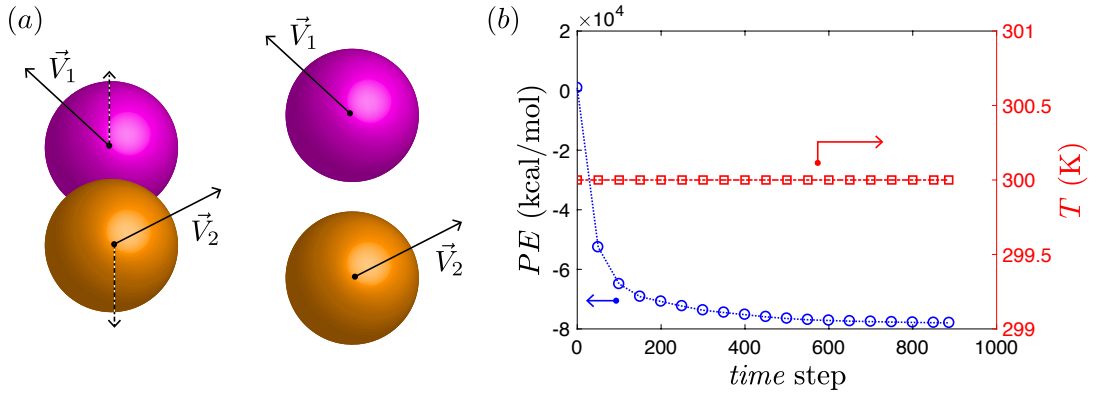

Figure 2.16: (a) Two molecules that are overlapped in the initialisation step are moved apart during energy minimization. This needs not be in the direction of their velocities. Since no time integration is performed on the system during this process, the initial velocities of molecules remain unaltered. (b) Reduction in the potential energy of a system during energy minimization resulting from the removal of overlaps. System contains 5832 TIP4P/2005 water molecules randomly arranged in a $R = 3.5$ nm sphere in the beginning. Temperature remains constant during the process, as velocities are unaltered.

2.5 Basic machinery – example of contact angle measurement

Once the interaction potentials between any pair of molecules are known, a system can be set up based on a target number of molecules, operating temperature, system dimensions and initial conditions. MD simulations usually work in four basic steps, and are followed in studying any system presented in this thesis. In this section, each of these steps will be explained using a simple example of contact angle measurement of a nanodroplet on a hydrophilic wall.

2.5.1 Energy minimization

The first step in this process is to arrange molecules in a spherical droplet of desired size. Initially, 5832 water molecules are randomly arranged in a sphere of $R = 3.5$ nm. Because of the initial random arrangement, several molecules may overlap with their neighbours, resulting in a high repulsive interaction among them. Time-integrating a system like this will move these molecules to unphysically large distances, thereby blowing up the entire simulation.

LAMMPS has a 'minimize' command to perform energy minimization over a system of particles. During energy minimization, the atom coordinates are iteratively adjusted so as to remove all the overlaps among them with an aim to attain a local potential energy minimum. Time-integration is not performed during this process. As shown in Figure 2.16(a), it may be easier to remove overlaps by moving the molecules in a direction different from what is suggested by their respective velocities. Figure 2.16(b) shows the potential energy change during the minimization process of the system mentioned above. During initialisation, all molecules are given velocities from a Gaussian distribution corresponding to a temperature of $T = 300$ K. As

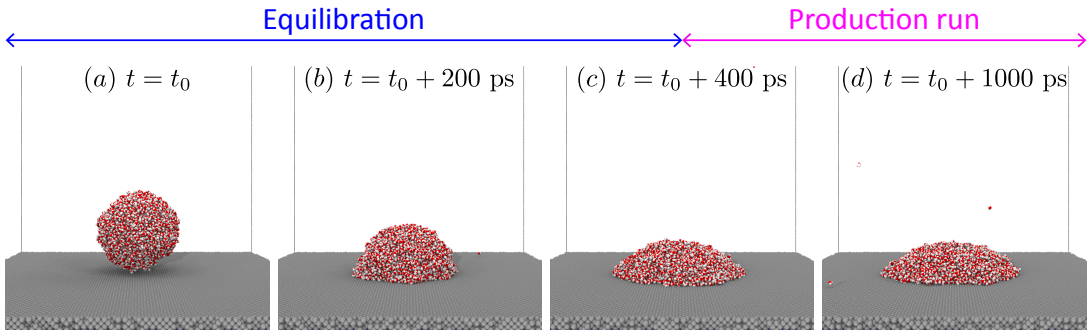

Figure 2.17: (a-c) Equilibration of a $R = 3.5$ nm droplet on a hydrophilic wall. (c-d) Time during which production run is carried out.

their velocities are not updated during energy minimization, temperature remains constant.

2.5.2 Equilibration and production run

After it reaches a local potential energy minimum, the system can now be equilibrated. Time-integration updates the velocities and coordinates of all molecules in the system. In this example, the droplet is placed over a substrate, which is pre-equilibrated at 300 K. The attraction from the underlying substrate will bring the droplet down and let it evolve until it reaches its equilibrium configuration. Figure 2.17(a-c) show different stages in the equilibration stage. By the end of $t = t_0 + 400$ ps, the centre-of-mass coordinate of the droplet in the direction normal to the wall, potential energy of the system and various other measurable quantities have come to a steady state, indicating that the system is in its equilibrium configuration.

If the dynamics of the spreading process is not of interest, it is better to let the system equilibrate as long as possible, and the data collection should only begin afterwards. During this 'production run' stage, relevant atom attributes, such as coordinates of all oxygen atoms, are stored in a separate file for post-processing. The amount of data collected during this stage directly determines the statistical reliability of the measured quantities, while evaluating their 'time averages'.

If the dynamics is of interest, it may not be possible to collect sufficient data for reliable statistics. In such cases, it is better to perform several versions of the same simulation with different initial conditions, and then evaluate any quantity that is of interest from each of these 'realisations'. This will give us an ensemble average of the measured quantity. If the system is in equilibrium, the 'ensemble average' evaluated in this manner and the 'time average' evaluated as before will give identical results. This is known as the 'ergodic hypothesis'.

During the equilibration and production run stages, it is desirable to geometrically arrange the processors in the domain such that each processor gets more or less the same number of atoms. When LAMMPS is executed in parallel, this will make sure that the load is uniform

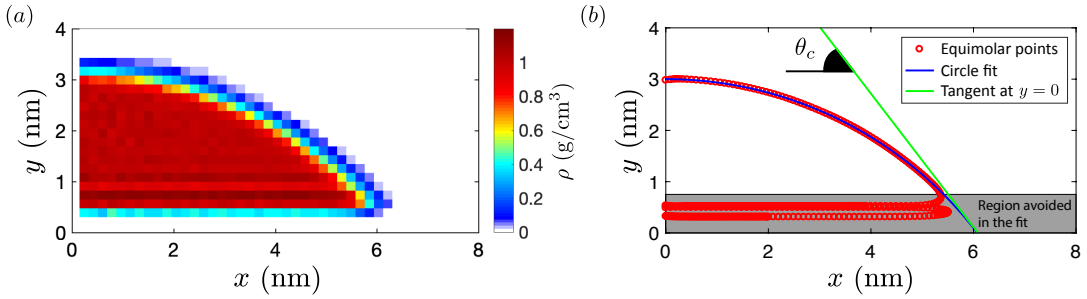

Figure 2.18: (a) 2D density field inside the equilibrated water droplet evaluated during the production run time. (b) Equimolar points, where the density falls to the average of the liquid and vapour bulk densities. A circle is fit to these points to determine the equilibrium contact angle θ_c. Roughly a 0.8 nm thick region above the surface is not included in the fit due to the density layering close to the wall. The first layer of wall molecules are at $y = 0$.

on each processor involved and it decreases the execution time to a great extent. LAMMPS has a 'processor' command to redistribute the total number of processors in all three directions and a 'balance' command to arrange them in any fashion. In all the simulations presented in this thesis, processors are initially arranged in the domain such that the load is uniformly distributed.

2.5.3 Post-processing

Once all the relevant atom attributes are obtained from the production run stage, several computer programs can be used to evaluate other measurable quantities that are otherwise difficult to determine during the previous stages. For post-processing the output data obtained from MD simulations, primarily C++ and MATLAB programs are used in this thesis. These programs read atomic positions and velocities from the LAMMPS output files and evaluates the relevant quantity. For example, if the position coordinates of all molecules in a droplet are known as a function of time, post-processing programs can easily evaluate the centre-of-mass location and velocity. For droplets coalescing in gaseous systems, if the stress tensors of the gas molecules are output, each of those molecule can be assigned into a spatial bin and the pressure field in the system can be determined as coalescence proceed. Typically, these codes are run serially on a single core and would take a few hours to a few days to finish, depending on the total number of atoms.

In the present example, a C++ program is written for evaluating the density profile inside the droplet. Since the effect of body forces such as gravity are negligible at the nanoscale, a nanodroplet will spread on a surface until a circular profile of the interface is achieved because of the surface tension forces. In this example, from the coordinates of all oxygen atoms, the density profile of the droplet can be evaluated by assuming axisymmetry around a centroidal axis normal to the wall. For this purpose, the entire domain is sub-divided into a number of bins, each of size 0.1 nm, and the local density is evaluated. Figure 2.18(a) shows that deep inside

the droplet, the local density is roughly the same as the bulk density of water (~ 1 g/cm^3) and towards the interface, the density drops to the vapour density. A Gnuplot code is then used to pick all those points on the interface where the density falls to the average of liquid and vapour bulk densities (see Fig. 2.18(b)). A circle is then fit to these points after discarding a region of roughly 0.8 nm above the surface. This is done in order to avoid any complications due to density ordering close to the wall. The tangent to the circle where it meets the top layer of the wall ($y = 0$) gives information about the contact angle made by the water droplet on the wall.

Chapter 3

Droplet coalescence commences in a *thermal regime*

The majority of this chapter is already published in *Perumanath, S., Borg, M. K., Chubynsky, M. V., Sprittles, J. E., and Reese, J. M. Droplet coalescence is initiated by thermal motion. Phys. Rev. Lett., 122:104501, Mar 2019.*

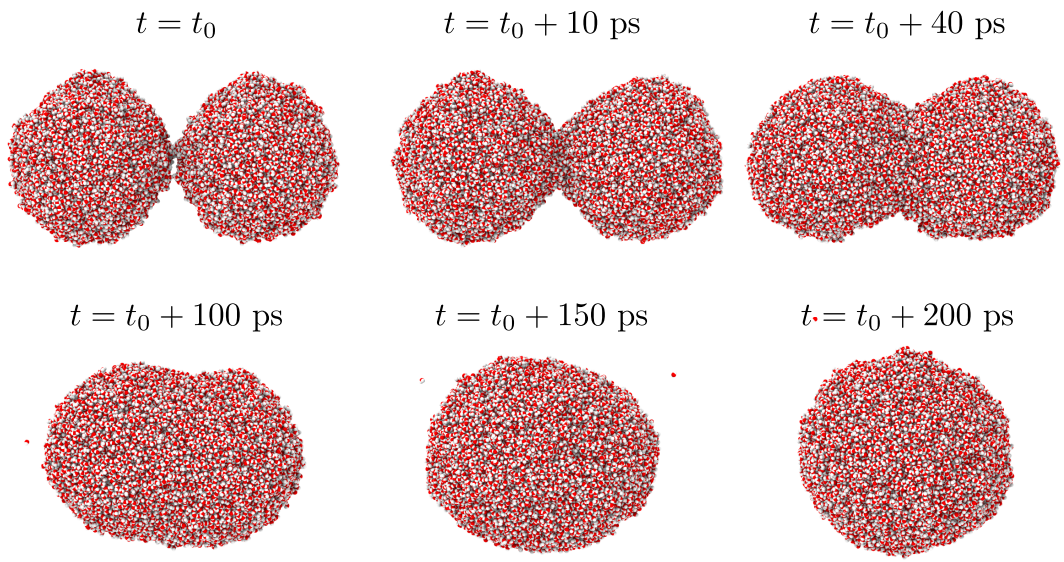

Figure 3.1: Coalescence of two water nanodroplets of radii $R = 5.1$ nm. A bridge connecting both droplets develops after the first contact between the droplets is established, which grows in time (measured in picoseconds (ps)) until the droplets are completely merged. Here, oxygen atoms are represented in red and hydrogen atoms are represented in white.

Droplet based systems are ubiquitous in our daily lives; ranging from storm cloud formation and rain droplet size distribution in the atmosphere to office ink-jet printers and emulsion-based products, such as mayonnaise (Kovetz and Olund, 1969; Ristenpart *et al.*, 2006; Miljkovic *et al.*, 2012; Boreyko and Chen, 2009; Kumar *et al.*, 1996). Often many of these systems involve coalescence of two or more smaller droplets that form a larger one. As a process that involves a

variety of length and time scales which span over a few orders of magnitude, the mathematical modelling of droplet coalescence is highly challenging (Eggers *et al.*, 1999; Duchemin *et al.*, 2003; Sprittles and Shikhmurzaev, 2014a,b,c; Paulsen *et al.*, 2012). Although existing computational models have provided us with deep insights into how the coalescence proceeds as a function of time (see Chapter 1), the reliability of these models breaks down drastically as one marches backward in time to the exact point of the beginning of coalescence. In other words, these models are not accurate in the initial stages of the process, as many of these models host a finite-time singularity in the beginning of coalescence, where the continuum assumption breaks down. Experimental study of droplet coalescence becomes increasingly challenging as one tries to investigate the early stage dynamics of the process, which involve small length and time scales.

In this chapter, the problem of coalescence is approached from a molecular perspective and we try to understand how this singularity is removed in reality. Molecular dynamics is perhaps the best tool to study the effect of non-continuum nature of the liquids on coalescence dynamics, as this technique makes no assumption that gives rise to a singularity. Figure 3.1 shows MD simulation snapshots of coalescence of two nanodroplets. Since every single atom in the system is modelled, the only restriction in using MD is that only droplets of nanometre sizes can be simulated. Nevertheless, good scalability of the results presented here is expected. In this chapter, mainly quasi-2D droplets are simulated, since it has been shown that the early stage dynamics of coalescence of spherical droplets can be asymptotically studied using their cylindrical counterparts (Eggers *et al.*, 1999) and also there are qualitative similarities between coalescence of cylindrical and spherical droplets (Burton and Taborek, 2007; Pothier and Lewis, 2012). Computationally expensive coalescence simulations of 3D spherical droplets are used to validate any inferences made by studying cylindrical droplets. This chapter is organised as follows: in Section 1, the thermal fluctuations at an interface is introduced and quantified. Section 2 investigates how these fluctuations affect the onset of coalescence. After a first contact is established between coalescing droplets, the physical mechanism of bridge growth is investigated in Section 3, thereby explaining how a singularity is removed. The affect of outer fluid and impact velocity is studied in Section 4. Lastly, Section 5 discusses the impact of this particular chapter.

3.1 Thermal fluctuations at droplet interfaces

By investigating closely the behaviour of interfacial thermal fluctuations and quantifying their characteristics, we can then start to understand how two droplets coalesce, with particular attention to its initial stages (where these fluctuations are thought to be important). For example, quantifying the amplitude of these fluctuations on droplet surfaces will give a rough idea about when the coalescence will initiate as two droplets are brought together from a distance. In what

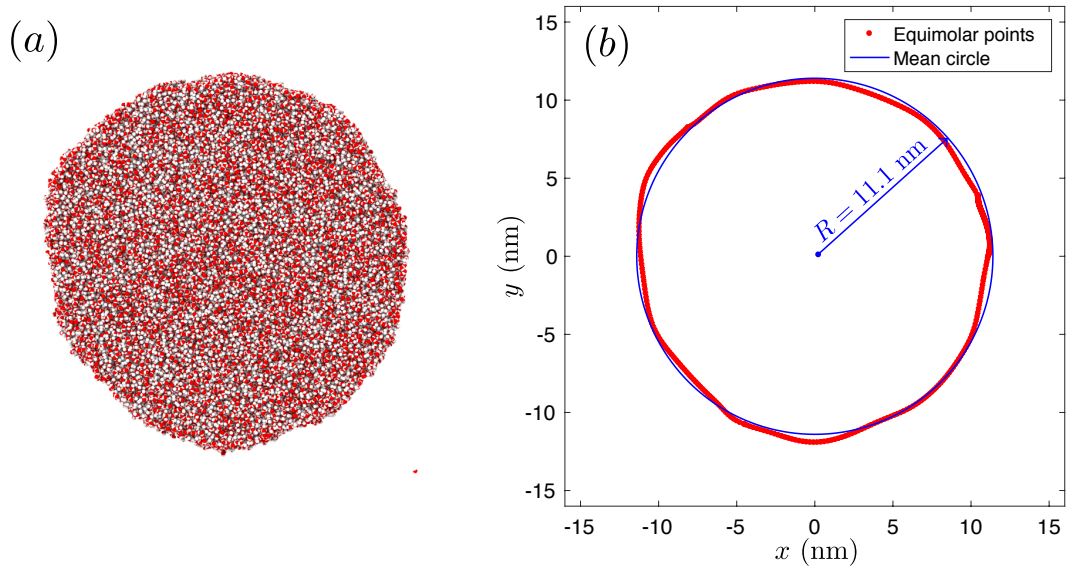

Figure 3.2: (a) MD simulation snapshot of a quasi-2D droplet at a particular instant of time. (b) The corresponding equimolar points (red), where the local density falls to the average of liquid and vapour densities, and the mean circular profile (solid blue circle). At any instant, the profile deviates significantly from the mean profile due to thermal fluctuations at the interface.

follows, the amplitude of interfacial thermal fluctuations on both quasi-2D and 3D spherical droplets are quantified using theory and compared to MD simulations.

Any interface is composed of some 'dynamic roughness' due to interfacial thermal fluctuations. Figure 3.2 shows the snapshot of a quasi-2D water nanodroplet with radius $R = 11.1$ nm and its instantaneous equimolar line. Since the liquid-vapour interface is diffusive in nature, an 'equimolar' line, where the local density falls to the average of the bulk densities of both liquid and vapour is identified to mark the location of the interface. It can be clearly seen that the presence of thermal-capillary waves distorts the interface from the mean circular profile of a droplet. The instantaneous profile of such a thermally fluctuating interface can be

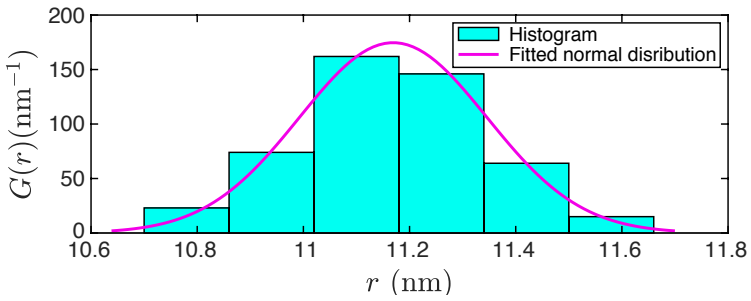

Figure 3.3: Probability distribution of the position of an interfacial point on the equimolar line with respect to the radius of a quasi-2D droplet with $R = 11.1$ nm. The location of this interfacial point is normally distributed about its mean surface.

represented by a sum of Fourier modes (or spherical harmonics, if it is a spherical droplet) that are orthogonal to each other. For a *large enough* droplet, the interfacial fluctuations are small in comparison to the large radius, and the oscillation of any 'interfacial point' on the equimolar line in the radial direction will be distributed normally about its mean location. Figure 3.3 shows the probability distribution, $G(r)$, of the location of a particular point on the interface of a droplet measured using MD, which follows a normal distribution.

For a planar interface, the capillary wave modes are plane waves, each characterized by a wave number $q \equiv 2\pi/W$, where W is the wave length. The theory of thermal-capillary waves (Rowlinson and Widom, 1982; Sides *et al.*, 1999) predicts that the mean-square amplitude of thermal fluctuations at the interface will be given by

$$\langle \zeta^2 \rangle_{pl} = \frac{k_B T}{2\pi\gamma} \ln\left(\frac{q_{\max}}{q_{\min}}\right), \tag{3.1}$$

where $q_{\max}$ and $q_{\min}$ are the maximum and minimum wave numbers, which are required to prevent divergence of the above expression. The square-root of Eq. (3.1) will quantify the standard deviation of the normal distribution $G(r)$.

For a spherical droplet, the above expression is still expected to hold, since for most modes (except for the longest ones) the mean surface is effectively flat on the scale of the wavelength. In the absence of an external field – for example gravity (which will be negligible at the nanoscale) – the minimum wave number will be determined by the longest possible wave on the surface. For the case of a spherical droplet, this will have a wave length of half of its perimeter, i.e. $q_{\min} \approx 2\pi/(\pi R)$. In Eq. (3.1), $q_{\max} = 2\pi/B_0$ signifies an upper cut-off for the wave number, beyond which it is meaningless to discuss fluctuations in terms of a set of continuous waves. Here, B_0 signifies the wave length of the shortest possible wave. An obvious choice for B_0 is the size of a constituent molecule (Rowlinson and Widom, 1982) and radius of gyration or segment length in case of polymer chains (Werner *et al.*, 1999). Therefore, by assuming the above equation to be valid for 3D spherical droplets, the standard deviation of thermal fluctuations on the surface is expected to be:

$$\sigma_{sph}(R) = \sqrt{\langle \zeta^2 \rangle_{sph}} \approx \sqrt{\frac{k_B T}{2\pi\gamma}} \left[\ln\left(\frac{\pi R}{B_0}\right)\right]^{\frac{1}{2}}. \tag{3.2}$$

It is assumed that $R \gg B_0$. Although σ is a diverging function of R, the divergence is very weak. It can be noted that on pure liquid surfaces, these waves have nanoscale amplitudes, i.e. $\sigma \sim \sqrt{k_B T/\gamma}$ (note that σ here is not to be confused with the LJ length parameter described in the previous chapter.)

For quasi-2D cylindrical droplets, the principal difference is that the characteristic lengths are quite different in the azimuthal and axial directions. Such droplets are of interest because: (a) for the same droplet radius R, a quasi-2D cylindrical droplet will only have fewer number of

molecules compared to its spherical counterpart, essentially promising huge savings in terms of computational power and (b) the complications that might arise because of the capillary pressure due to the azimuthal curvature are completely absent in this geometry. To this end, the axial length L must be made smaller compared to circumference of the droplet, i.e. a 'thin disc' geometry is assumed. In all the cases studied here, a value of $L \approx 3r_c$ is chosen to avoid other complexities, for e.g. finite size effect.

For such a thin disc geometry, i.e. $R \gg L$, an expression for the standard deviation of the thermal fluctuations is derived:

$$\sigma(R)_{cyl} = \sqrt{\langle \zeta^2 \rangle_{cyl}} = \sqrt{\frac{k_B T}{2\pi\gamma}} \left[\frac{3R}{2L} + \ln\left(\frac{L}{B_0}\right) \right]^{\frac{1}{2}}, \tag{3.3}$$

(see Appendix A for full derivation). Unlike Eq. (3.2), Eq. (3.3) diverges quickly with increasing R, while keeping L constant. This means that, beyond a certain limit (say, $2\pi R > 100$ nm), quasi-2D cylindrical droplets cannot model their 3D counterpart. However, a smaller full-cylindrical droplet spread on a wall can give an identical coalescence radius R but has a lower value of σ than predicted by Eq. (3.3) (see example in Fig. 3.4); a value of σ_{cyl} close to σ_{sph} can be obtained in the same way when R is large. This is because in the system where a droplet is spread on a wall, the longest Fourier wavelength is only a fraction of πR. Coalescence of two such quasi-2D droplets spread on walls is used in this thesis to study the largest of the systems investigated (i.e. with $R = 58.5$ nm). Coalescence simulations using this method is not necessary for small droplets as (a) the computational cost of simulating small droplets are feasible and (b) the top most portion of the spread droplet must be as far away as possible (at least $\sim$10 nm) from the wall in order to reduce the influence of density layering near the wall on coalescence dynamics; this is achievable only for *large enough* droplets ($R > 20$ nm).

The above discussion describes the impact of the longest possible thermal-capillary wave on a surface on σ. In order to determine B_0, the length scale that describes the shortest wave, a separate set of MD simulations of cylindrical droplets with varying R, but fixed L are used. Water droplets at $T = 300$ K are simulated and the standard deviation of surface thermal fluctuations as a function of the perimeter $2\pi R$ (see Fig. 3.5) is explicitly evaluated. During the simulation, the position of all atoms are recorded at regular intervals of 0.02 ps for a total simulation time of 1 ns. Then, a point on the equimolar line is randomly chosen and the standard deviation of its thermal fluctuation is evaluated. A fit to the MD data points in the form of Eq. (3.3) gives $B_0 \approx 1.2$ nm, which represents around 3 water molecule diameters in scale. In Fig. 3.5, the standard deviation of fluctuations for 3D spherical droplets with the same value of B_0 is also shown, assuming B_0 applies to the 3D case.

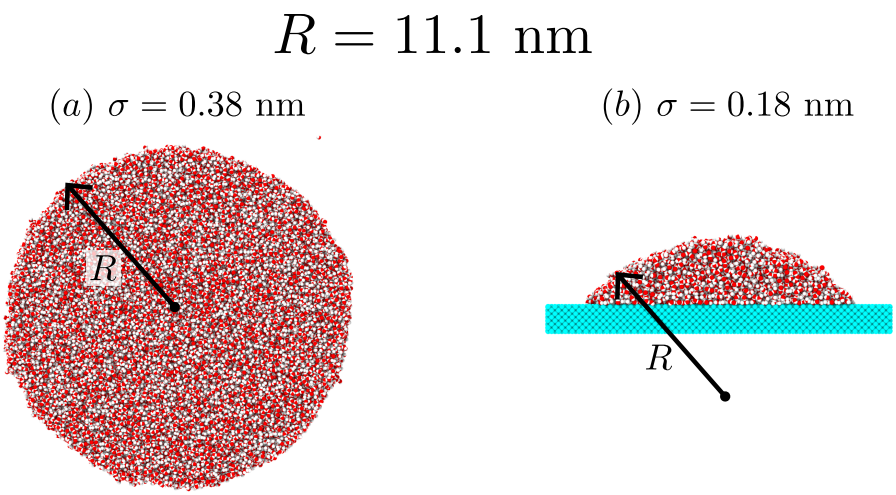

Figure 3.4: The standard deviation of thermal fluctuations changes as the longest Fourier wavelength on the surface changes, even though the coalescence radius (R) is kept constant. The figure shows a full cylindrical droplet and a smaller cylindrical droplet spread on a wall, each with identical R. As the longest Fourier wavelength in (b) is smaller than that in (a), σ is also correspondingly smaller in (b).

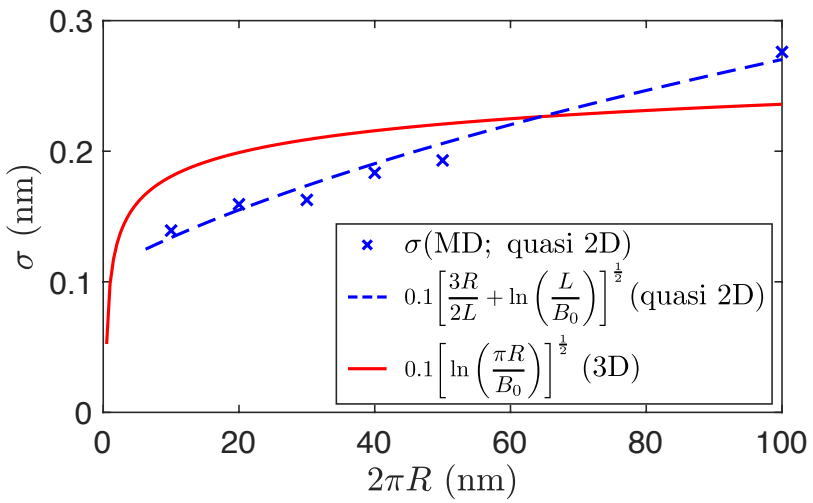

Figure 3.5: Standard deviation of the local thermal fluctuations on top of (quasi-2D) cylindrical droplets as a function of droplet circumference $2\pi R$. The broken blue line is a fit to the blue points in the form of Eq. (3.3) using only B_0 as the fitting parameter. Note that Eq. (3.3) is not applicable when $2\pi R < L$. The red curve shows Eq. (3.2) for the 3D droplet case with the same fitted value of B_0 from the quasi-2D case. A C++ code is written in order to evaluate average fluctuation amplitudes from MD simulations.

3.2 Location of first contact between droplets during coalescence

The traditional understanding of the formation of a bridge between two droplets during coalescence is by the growth of a hydrodynamic instability (Vrij, 1966; Lucassen *et al.*, 1970). When two droplets approach each other, the attraction between their confronting interfaces will cause a set of modes on both surfaces to grow exponentially until a first contact between them is established. Once a bridge of finite size connects the droplets, interfacial tension will drive the processes until both droplets are completely merged; these processes have been extensively studied by continuum CFD simulations (Paulsen *et al.*, 2012; Sprittles and Shikhmurzaev, 2012, 2014a).

What has not been studied in the past is the onset of coalescence: when two droplets start to interact, touch for the first time and the subsequent bridge growth. The presence of thermal fluctuations on the surface will inevitably destroy the axisymmetry along the line of approach of two droplets that is usually assumed in continuum simulations during coalescence. With thermal-capillary waves on the surface, there is no guarantee that the first contact between the droplets will happen along the line connecting their centres-of-mass. Furthermore, with the limited set of modes present on nanodroplet surfaces, the mechanism of onset of coalescence may be different from what is described above for larger droplets. Figure 3.6 shows an MD simulation snapshot of the beginning of coalescence of two droplets, where the first contact occurred offset from the line of approach. During the simulation, two independently equilibrated droplets of same size are brought towards each other along the coalescence axis connecting their centres-of-mass, either in vacuum or in an outer fluid with a relative velocity V_r. This is repeated several times using different realisations. A sample LAMMPS code for such a case is given in Appendix B.

Knowing the relative fluctuation of neighbouring points on the surface, assuming that the fluctuations on both droplets are independent and there are no instabilities, the theory of thermal-capillary waves allows us to derive an expression for the extent of the region (l_c) from the coalescence axis, within which a contact can happen:

$$l_c \approx \left(\frac{k_B T}{\gamma}\right)^{1/4} R^{1/2}, \tag{3.4}$$

(see Appendix C for details of the derivation). Figure 3.7 shows the distribution of coalescence onset points along x for two quasi-2D droplets of radii $R = 11.1$ nm obtained through 40 independent realisations. While the most probable location for the onset of coalescence is close to the line of approach, as expected, it is still possible to initiate coalescence from a location away from the line of approach. From Fig. 3.7, l_c is comparable within a pre-factor of order unity to the spread of the distribution obtained through MD simulations, which is determined by fitting a Gaussian function to it (99% confidence interval (CI)). This shows that for nanodroplets, within the region $|x| < l_c$, the first contact happens when thermal fluctuations of

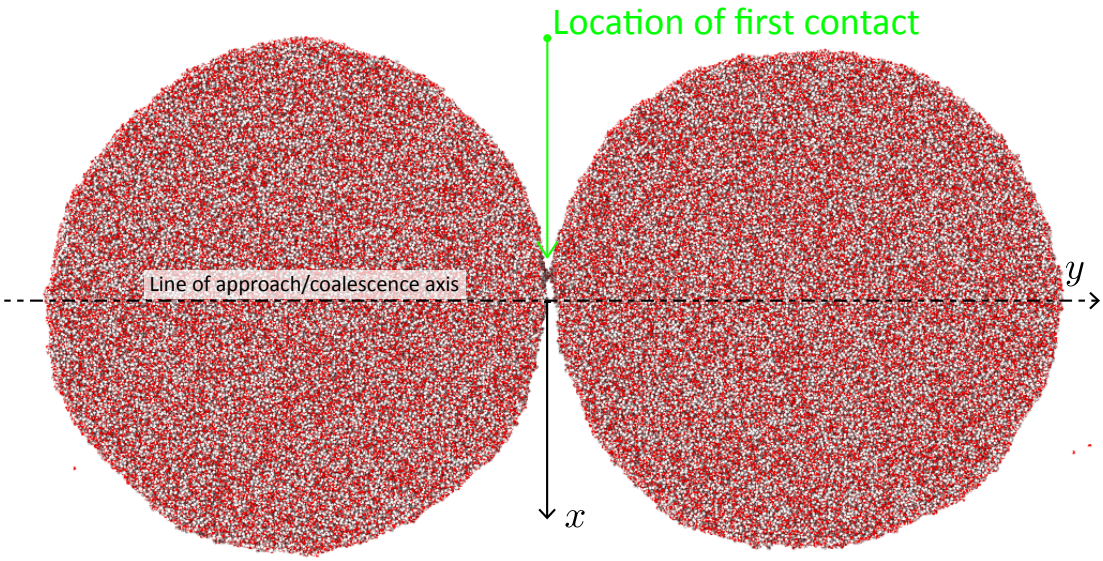

Figure 3.6: MD simulation snapshot of coalescence of two droplets with $R = 20.1$ nm. The presence of thermal fluctuations on their surfaces renders the onset of coalescence a stochastic process. Here, the first contact can be seen made away from the line of approach.

coalescing droplets meet from opposite sides; there is no evidence of a growth of hydrodynamic instability. In other words, no significant shape change of the droplets, as described in Subsection 1.1.1, is observed in any of the MD simulations of nanodroplets before the coalescence began. Consequently, there may be multiple contacts between droplets during coalescence, which is more probable for larger droplets. Figure 3.8 shows the beginning of coalescence between two quasi-2D droplets with $R = 58.5$ nm characterised by two local bridges between them.

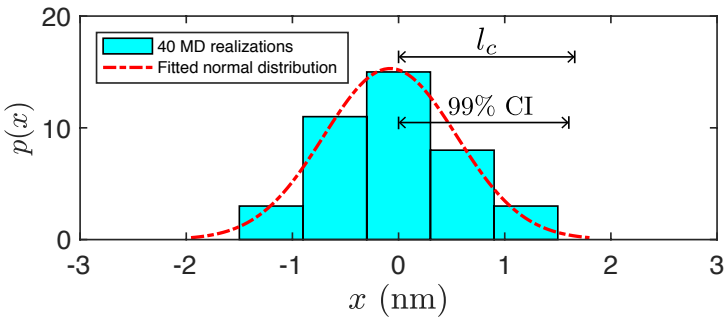

Figure 3.7: Distribution of coalescence onset points obtained from 40 MD realisations of two $R = 11.1$ nm quasi-2D droplets coalescing in vacuum. See Fig. 3.6 for the definition of x direction.

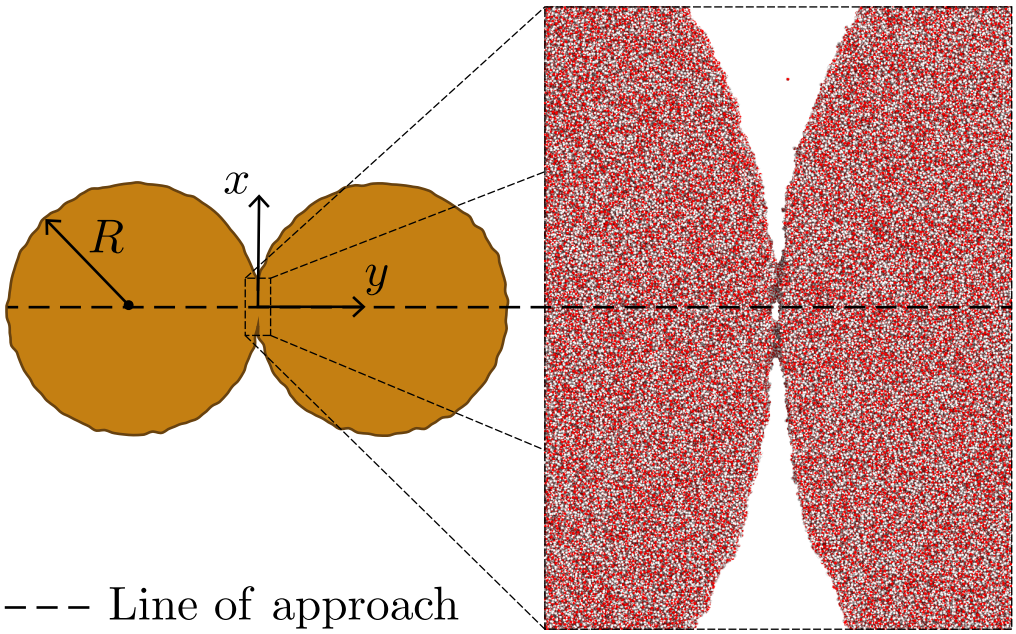

Figure 3.8: MD simulation snapshot of two cylindrical droplets coalescing with $R = 58.5$ nm, characterised by multiple local bridges between the droplets.

3.3 Physical mechanism of the bridge growth

Continuum simulations have shown how the flow field develops inside the droplets once a finite bridge connects both droplets, which results in the complete merger of them. Traversing from the unperturbed surfaces of both droplets towards the bridge, there is a sharp contrast in the local curvature at the bridge. In an attempt to equalise local curvature everywhere on the liquid surface, the surface tension will drive the entire process until a larger droplet forms. The traditional picture of bridge growth, therefore, is that a 'flow' of liquid develops during this surface tension-driven process and it will push the bridge front to its new location (Hopper, 1990; Eggers *et al.*, 1999; Duchemin *et al.*, 2003). Figure 3.9 schematically shows how a 'control volume' close to the bridge front moves to its new location according to the traditional understanding. Depending on the relative magnitude of the driving surface tension force and the opposing viscous or inertial forces, different scaling arguments have been developed for bridge growth in time, as already discussed in Chapter 1. As discussed previously, such mathematical models of bridge growth hosts a finite-time singularity in the beginning of coalescence.

Interestingly, there has been no study so far which has looked into the role of nanoscale effects near the singularity in coalescence. Using MD, the trajectories of different groups of molecules close to the bridge front are analysed as coalescence proceeds. Figure 3.10 shows the MD simulation snapshots of bridge growth at different stages of coalescence. In the initial stages, the bridge grows due to *collective molecular jumps* (Fig. 3.10(a)) next to the bridge

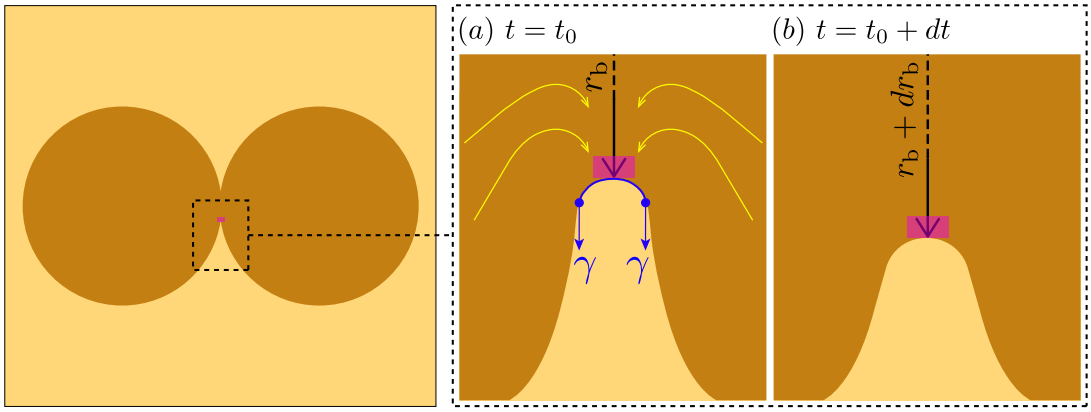

Figure 3.9: A schematic of our traditional understanding of how a bridge evolves with time during droplet coalescence. As the interfacial tension pulls the high-curvature region, a 'flow field' develops which will push a control volume next to the bridge front to its new location.

front (indicated by green arrows) instead of a *bridging flow* of molecules towards the neck, as one might expect from the traditional picture. During this initial *thermal regime*, which these simulations reveal for the first time, due to the proximity of the confronting surfaces of the droplets coupled with the thermal-capillary waves at the interface, the molecules are observed to gradually fill the intervening gap between the droplets (this motion resembles that of a zip). When there are multiple local bridges, this mechanism will go on until two such bridge fronts meet from opposite sides and merge. Otherwise this type of bridge growth proceeds until the bridge front reaches a *thermal length scale* l_T from the coalescence axis, where thermal fluctuations can no longer be the dominant mechanism of the bridge evolution and the traditional hydrodynamic mechanism takes over the dynamics.

For quantifying l_T, a statistical method is adopted, since the initial stages of bridge growth involves thermal motion of the molecules. At first, Fig. 3.11(a) shows how interfacial molecules (yellow) are identified in the system at a particular instant of time by using the criteria mentioned in Chapter 2 and 'bridge molecules' (maroon) selected within a 1 nm region of the bridge. At a later stage, molecules are identified in a similar way (coloured cyan), however now we are able to highlight those molecules which have travelled from the original maroon list. If the fraction of molecules which came from the maroon to the cyan list is less than 0.5, the bridge growth is identified to be in the thermal regime; otherwise if the fraction is larger than 0.5, this is identified as the hydrodynamic regime. The point where this fraction crosses over the half way mark of 0.5 is designated as the extent of the thermal regime, identified by the thermal length scale l_T. l_T is measured for different droplet sizes during their coalescence and its size-dependence is shown in Fig. 3.12, which shows $l_T \sim \sqrt{R}$. It is also observe that l_T is seemingly captured by $2l_c$ for both 3D and cylindrical droplets, which is reasonable, since both length scales are defined by thermal mechanisms.

The bridge growth during coalescence is further analysed by studying the time-evolution of

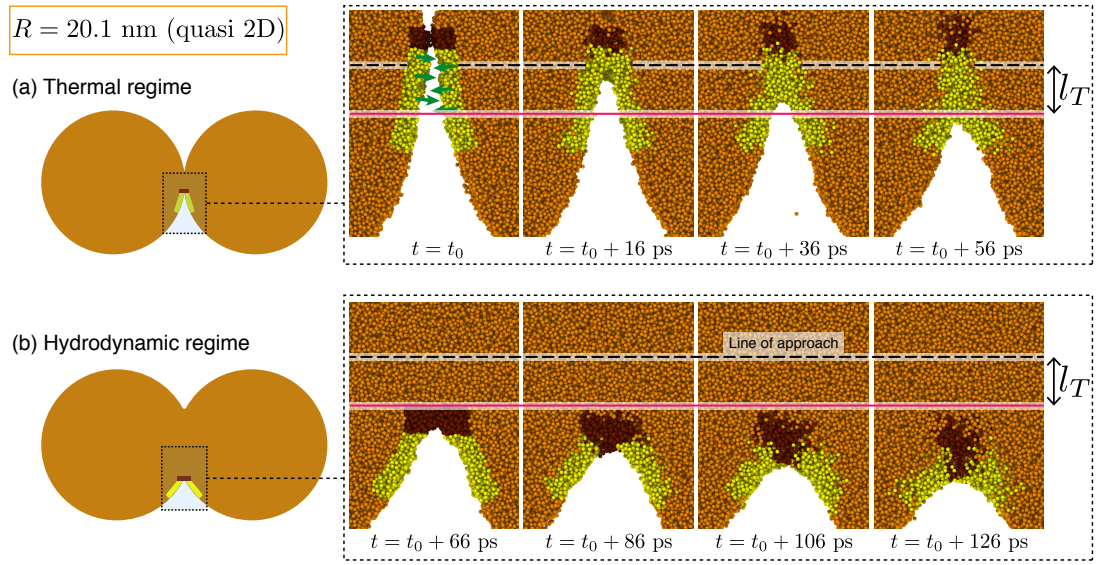

Figure 3.10: The bridge growth mechanism at different stages of coalescence. (a) In the 'thermal regime', the bridge grows due to a large number of molecules jumping into the gap between the droplets. These collective molecular jumps occur until the bridge radius reaches l_T, measured from the line of approach. (b) At a later stage, i.e. after the bridge has passed l_T, the mechanism resembles that of the traditional picture, where the liquid hydrodynamics moves a 'control volume' next to the bridge front to its new location. In the figure, only oxygen atoms are shown for improved visibility, and a few of them are coloured differently for illustrative purposes.

equimolar lines. Figures 3.13 – 3.15 show the equimolar line and corresponding bridge evolution in three cases (quasi-2D) right after the first contact is established between the droplets. Here 'offset' represents how far away from the line of approach the first contact is established. Figure 3.16 shows the bridge evolution for two cases when 3D spherical droplets coalesce. The bridge evolution in the initial stages of both quasi-2D and 3D droplets is observed to be linear in time with a characteristic speed that seemingly depends on the local radius of curvature next to the bridge front. It is to be noted that in most cases, the characteristic speed of bridge evolution is much greater than the viscous-capillary velocity scale (γ/μ_l), which would be expected, if the bridge was expanding in the Stokes regime. This further verifies that the bridge operates in a new thermal regime in the beginning of coalescence.

In order to better differentiate the mechanism of bridge evolution at different times, the time-evolution of the total surface area of the droplets during coalescence is studied. With MD, the number of interfacial molecules in the system can be tracked, which is a direct indicator of the instantaneous total surface area of the droplets (see Chapter 2). Since during coalescence, there is a reduction in the surface area as the bridge grows in time, these two measurable quantities must be directly related.

If the total surface area of a single droplet is A, and the number of interfacial molecules per unit

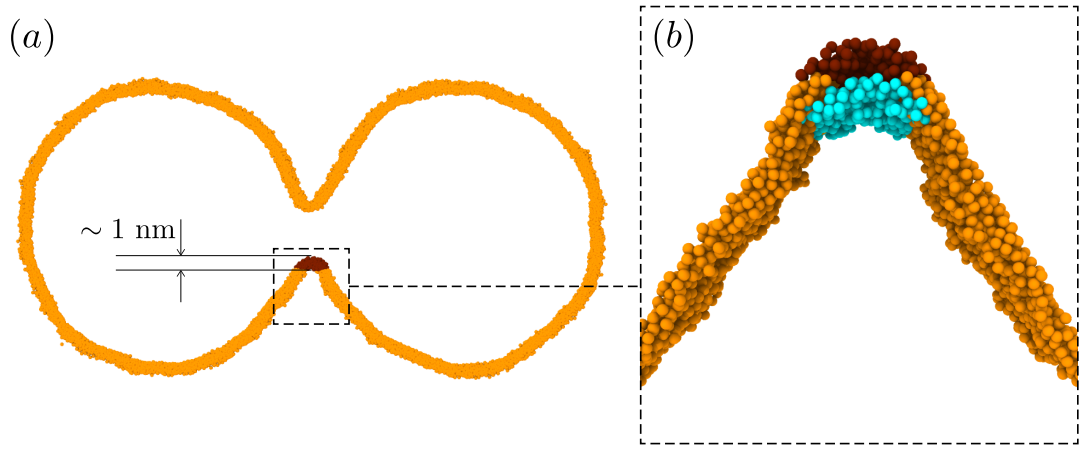

Figure 3.11: (a) The interfacial molecules in the system during coalescence of two $R = 11.1$ nm droplets. Only oxygen atoms are shown. A few molecules near to the lower bridge front are identified and coloured differently. (b) Bridge front molecules at a later stage in coalescence are coloured in cyan for comparison with interfacial molecules in (a). A C++ code is written in order to distinguish these groups of molecules at different timesteps.

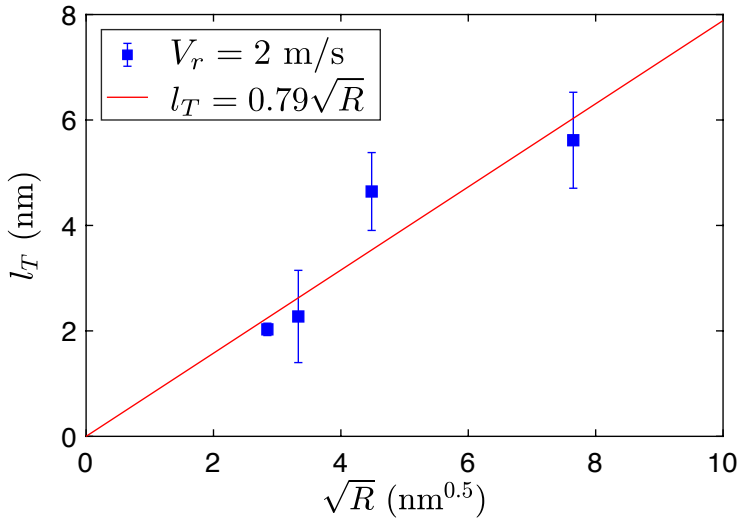

Figure 3.12: The variation of the extent of the thermal regime l_T with $\sqrt{R}$. Here V_r denotes the approach speed of both droplets.

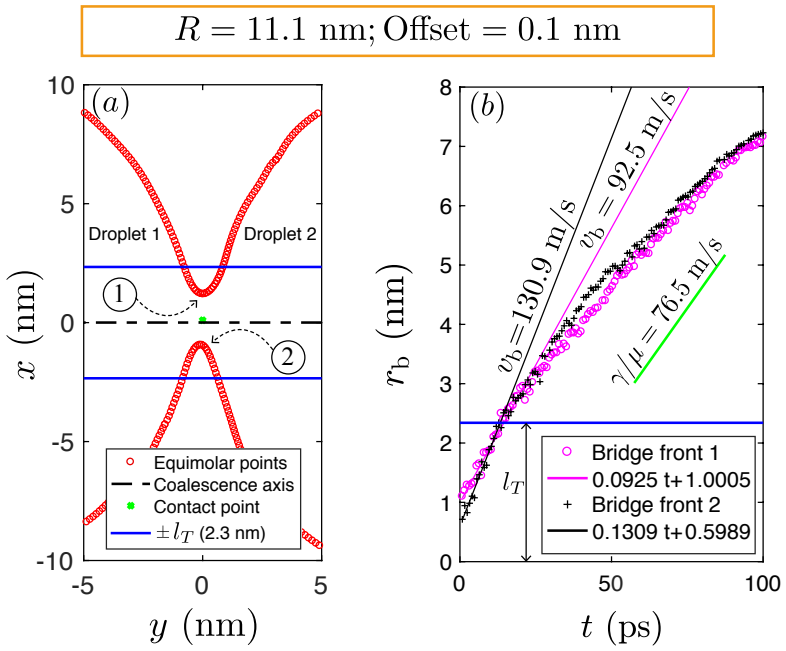

Figure 3.13: (a) The equimolar line showing the location of the interface during coalescence right after a contact is established close to the coalescence axis ($R = 11.1$ nm). Bridge fronts are randomly labelled as 1 and 2. (b) Bridge growth in time for the case shown in (a). The bridge location is measured from the coalescence axis. Here $t = 0$ denotes the time at which a bridge appeared in the equimolar plots. In reality, the coalescence might have begun a few timesteps earlier than this. A C++ code is written in order to identify the equimolar points.

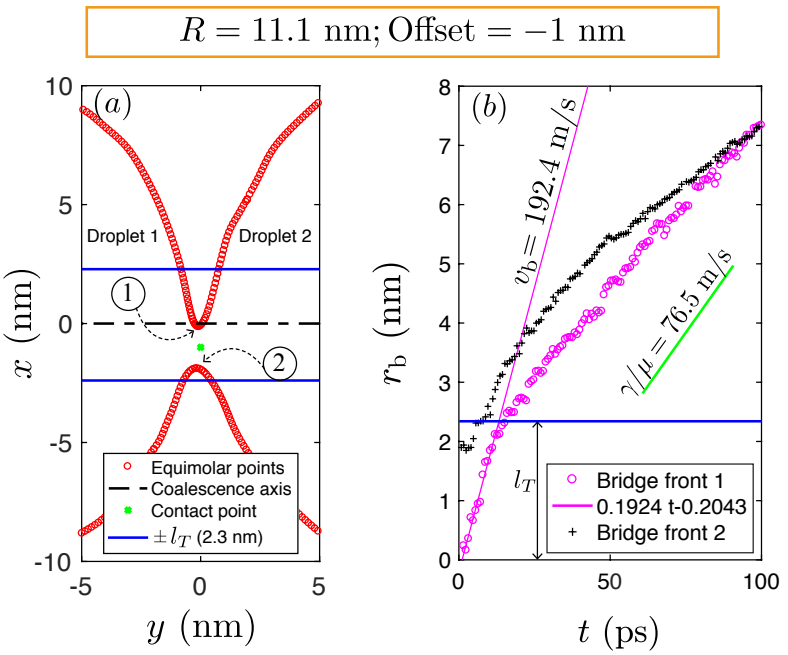

Figure 3.14: Similar to Fig. 3.13, but here, the first contact occurred significantly offset from the coalescence axis.

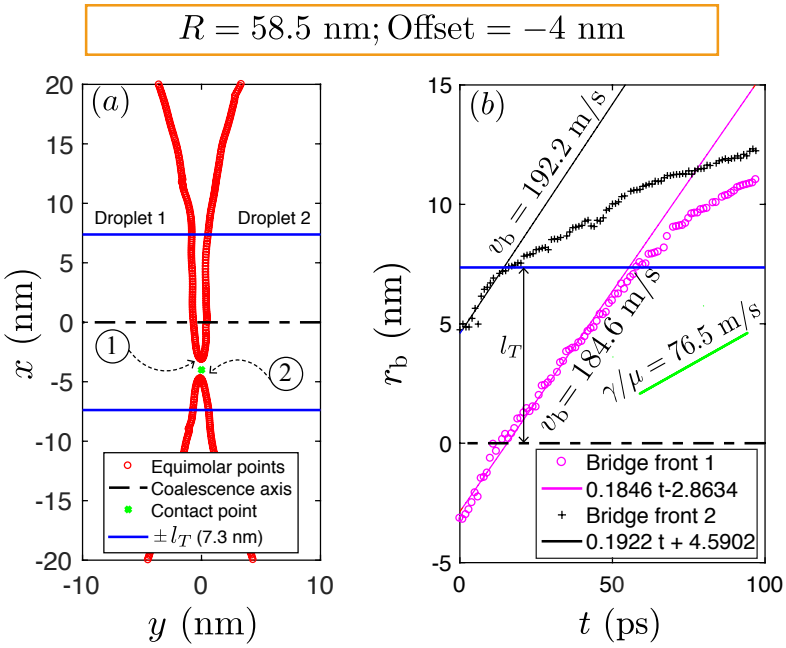

Figure 3.15: Similar to Fig. 3.13, but for $R = 58.5$ nm droplets with the first contact again significantly offset from the coalescence axis.

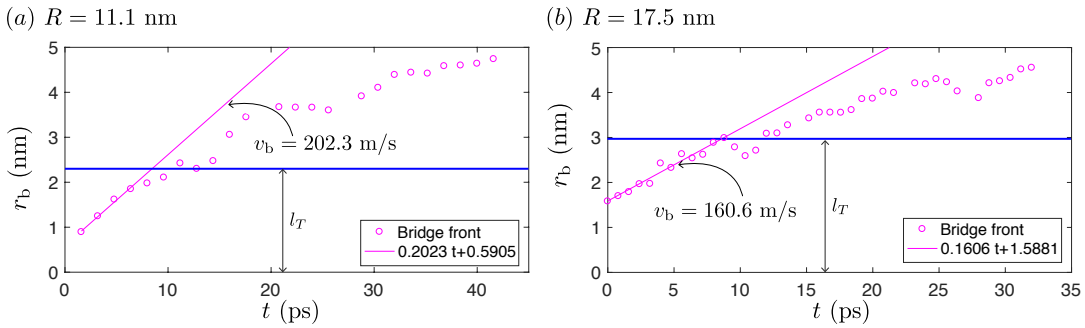

Figure 3.16: Bridge growth in time in the case of coalescence of two 3D spherical droplets. The bridge growth in the early stages is linear in time as it is in the case of cylindrical droplets with a speed much larger than the viscous-capillary velocity scale.

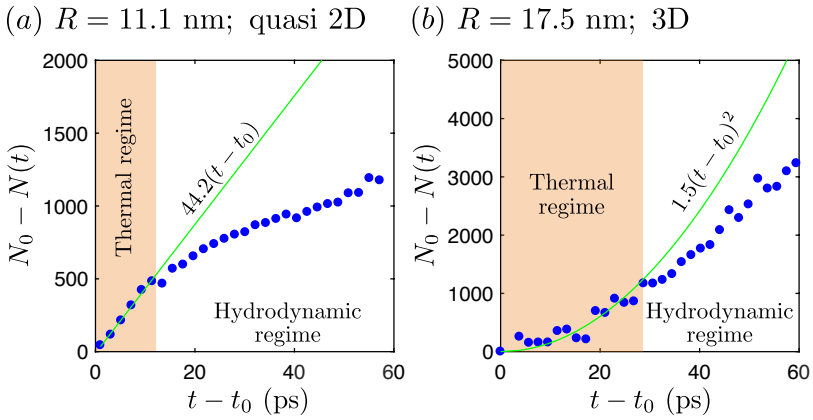

Figure 3.17: Time variation of the number of interfacial molecules during coalescence of (a) two quasi-2D droplets and (b) two 3D spherical droplets.

area is n_A, the change in the number of interfacial molecules during coalescence when the area decreases by $2\Delta A$ will be $2n_A\Delta A$. That is the rate at which the number of interfacial molecules are changing:

$$dN/dt = 2n_A(dA/dt). \tag{3.5}$$

The decrease in the area can also be estimated in terms of the rate of bridge growth:

$$dA/dt = -(dr_b/dt)\Delta Z, \tag{3.6}$$

where ΔZ is the length of a particular bridge front over which molecular jumps occur in the thermal regime.

Combining Eqs. (3.5) and (3.6), an estimate for the bridge growth speed for comparison with its counterpart observed in MD simulations is obtained:

$$v_b \equiv \frac{dr_b}{dt} \approx \frac{-dN/dt}{2n_A\Delta Z}. \tag{3.7}$$

Figure 3.17(a) shows the time dependence of the number of interfacial molecules in the system during coalescence of two quasi-2D droplets that corresponds to the case of 'bridge front 1' highlighted in Fig. 3.14. The variation of interfacial molecules are linear in time: $N_0 - N(t) = -dN/dt(t - t_0)$. Here N_0 denotes the number of interfacial molecules above or below the contact point, before coalescence began, $N(t)$ is the instantaneous number of interfacial molecules above or below that contact point, and t_0 is the time at which that contact is made. From Fig. 3.17(a), with $-dN/dt \approx 44.2$ molecules/ps, $\Delta Z \equiv L = 4.3$ nm used in this study, and $n_A \approx 25$ molecules/nm^2 for water-vapour interface, Eq. (3.7) predicts $v_b \approx 200$ m/s, which agrees well with the bridge growth velocity in Fig. 3.14(b). The slower speeds in Fig. 3.13(b) is due to a smaller dN/dt because of the initial contact occurring close to the coalescence axis.

On the other hand for spherical droplets, ΔZ grows as the bridge expands in time. Since the bridge growth in the thermal regime is observed to be linear in time for spherical droplets as well (Fig. 3.16), $\Delta Z \equiv 2\pi r_b \sim t$, so that $-dN/dt \sim t$ since $v_b \sim t^0$ from Eq. (3.7). This implies that the number of interfacial molecules should decrease as $\sim t^2$ in the thermal regime and Fig. 3.17(b) seems to agree well with this.

As expected, the bridge growth qualitatively changes after the thermal regime in both cases, as now there is a 'flow' of molecules towards the neck. It is interesting to note from Figs. 3.14(b) and 3.15(b) that even though there is no symmetry in bridge growth in the initial stages of coalescence, a symmetry gets established as time proceeds as is usually assumed in continuum simulations.

3.4 Effect of outer fluid and impact velocity

In many realistic situations, droplet coalescence occurs in the presence of an outer fluid. In nature, rain droplets coalesce by bombarding into each other at various speeds in the presence of air. A variety of industrial applications involve coalescence of liquid droplets in another liquid. In this section, the effect of outer fluid and impact velocity on l_T is studied.

Droplet coalescence is simulated in a nitrogen atmosphere at various densities (see Fig. 3.18), and separately in the presence of liquid ethane. Both droplets are brought towards each other and l_T is measured as described earlier. From Fig. 3.19, the extent of thermal regime is observed to be independent of the outer gas Knudsen number (Kn), where $\mathrm{Kn} \equiv \lambda/R$ is defined as the ratio of mean-free-path of gas molecules to the droplet radius. Interestingly, when the outer fluid is a liquid (i.e. in the limit as $\mathrm{Kn} \to 0$), a negligibly small l_T is obtained (not shown in the figure), which is close to the spatial resolution of the method described above to determine l_T. Since every fluid is composed of its own constituent molecules, a system of liquid-in-liquid emulsion will have a finite non-zero Kn. After both droplets of the dispersed medium make the first contact at a molecular scale, the first few molecules which form the bridge will not be able to develop the bridge due to a 'flow of molecules', simply because there are not many molecules available to carry out this process. Consequently, the bridge must expand in a thermal regime to a finite extent, even if the outer fluid is as dense as a liquid. The interfacial molecules will collectively jump to the gap that still exists between the two fluids (dictated by immiscibility).

Another complication that might arise in such case is the depletion layer interaction between coalescing droplets, as it plays a role in coagulation of colloidal particles. In colloids, the excluded volume around the dispersed phase gives rise to forces that are of entropic origin that bring these particles together to coagulate. As the continuous phase moves out of the intervening gap between the dispersed phase particles, the corresponding rise in osmotic pressure in the surroundings will push the dispersed phase, aiding coagulation. On the contrary, for the case

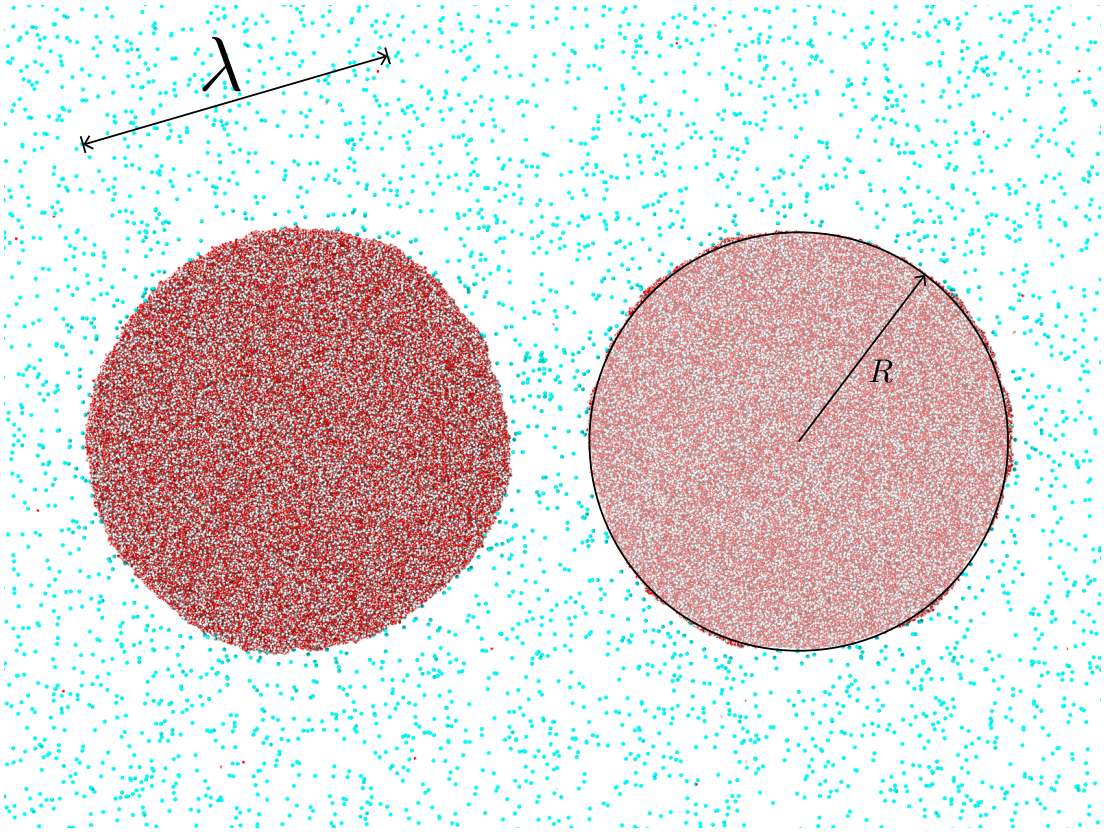

Figure 3.18: MD simulation domain used in order to study the effect of an outer gas on l_T. A Knudsen number is defined based on the mean-free-path of gas molecules λ and the droplet size R in order to characterise the rarefaction in the outer medium.

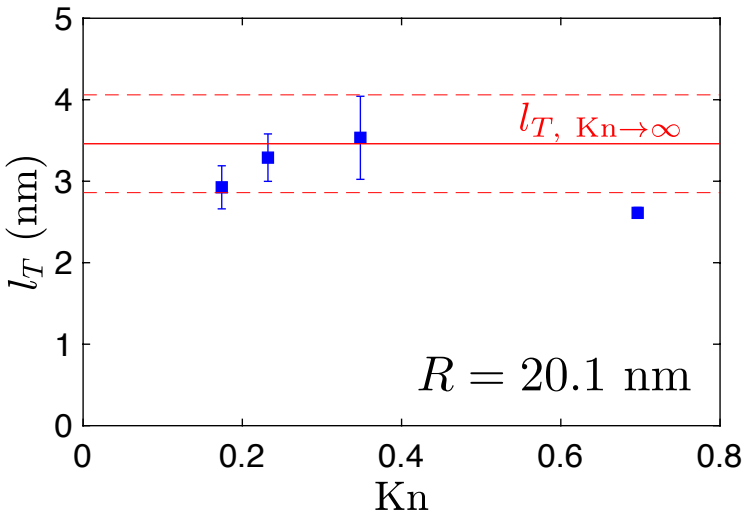

Figure 3.19: The variation of l_T with outer fluid Kn. For gaseous atmospheres, l_T is essentially independent of Kn in the range of Kn studied here. In the figure, Kn $\to \infty$ corresponds to the value in vacuum, with dashed lines representing the standard error.

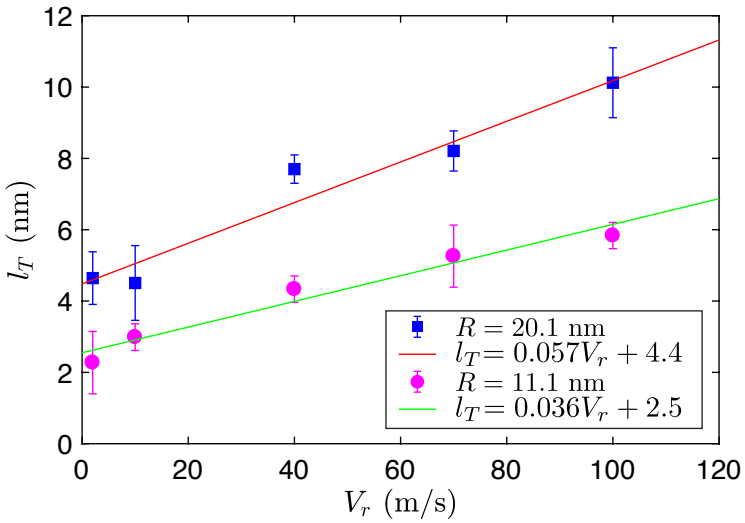

Figure 3.20: The variation of l_T with impact velocity for $R = 11.1$ nm and $R = 20.1$ nm droplets. The variation is linear with a non-zero y-intercept.

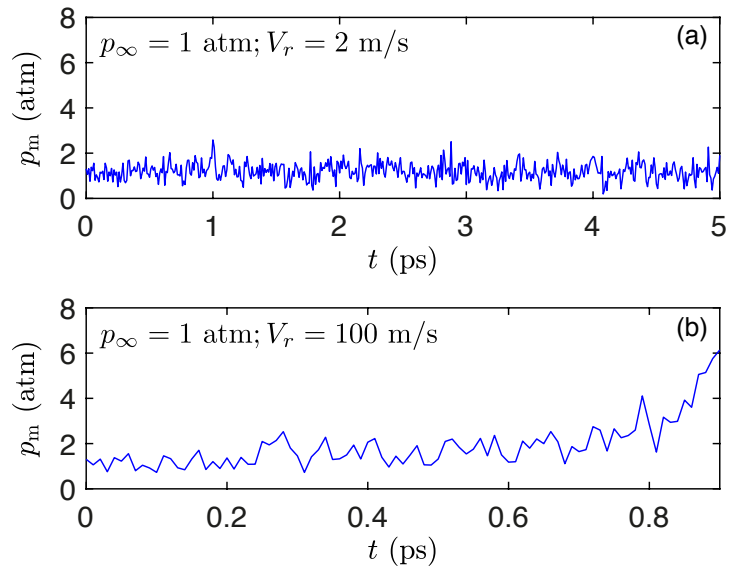

Figure 3.21: Variation of local pressure between approaching droplets (p_m) when ambient pressure is 1 atm. $p_\mathrm{m} = p_\infty$ in the beginning of the simulation. (a) At low approach speeds, the local pressure stays roughly as a constant until coalescence begins at around $t \approx 5$ ps. (b) At higher speeds, compressibility of the ambient gas becomes noticeable, as the intervening gas molecules do not get sufficient time to escape from the gap between the droplets as they approach. A higher number density of gas molecules in the local region gives rise to a higher pressure. Here, coalescence begins at $t \approx 0.9$ ps, as the approach speed is higher.

of droplet coalescence, there is no depletion layer around the droplets; in fact there is a local high-density region of gas just around the droplets (Ramisetti *et al.*, 2017). As a result, when the droplets approach each other in an gaseous medium, particularly at high approach speeds, the pressure of the gas in the intervening gap is observed to rise (see Fig. 3.21), primarily because of the increase in number of gas molecules in the gap. Once the gap width falls within a minimum distance, thermal fluctuations initiate coalescence of nanodroplets, as discussed before. These evidences suggest that the depletion interactions are not of relevance during droplet coalescence.

The effect of impact velocity on l_T is studied by imposing a wide range of initial centre-of-mass velocities ($\pm V_r/2$) to both droplets coalescing in vacuum. Figure 3.20 shows the variation of l_T with V_r for two droplet sizes. A simple argument based on geometry and hydrodynamics can predict the linear behaviour exhibited by l_T (see Appendix D). The non-zero y-intercept, which indicates the limit when the impact speed approaches zero is clearly a nanoscale effect which arises because of the bridge growth due to collective molecular jumps.

3.5 Discussion and outlook

The major impact of the existence of a thermal regime in the initial stages of droplet coalescence is that it provides us with an improved understanding of how a singularity is removed in coalescence. This particularly inspires one to see the traditional problems in fluid dynamics, which host a singularity in their mathematical formulation from a molecular perspective. The existence of a thermal regime in coalescence calls into question previous studies that have tried to address this issue through continuum simulations (Paulsen *et al.*, 2012; Sprittles and Shikhmurzaev, 2014a). These simulations are highly sensitive to the initial conditions such as the value of initial bridge radius with which the simulations begin, and is usually below the corresponding l_T found in this work. Since existing CFD simulations do not consider such fundamental molecular physics in their formulations, the next best way to incorporate the effects of thermal fluctuations is to use $r_b \sim l_T$ as the initial condition. Although this will qualitatively improve the closeness of simulations and experiments, their accuracy must be quantified separately.

Interestingly, for two $R \sim 1$ mm droplets (the size that is usually considered in experiments), $l_T \sim 1$ μm, which shows how a high-aspect ratio geometry between the confronting surfaces of a droplets enhances the extent to which nanoscale phenomena such as molecular jumps can have an effect. With bridge fronts expanding with a high speed as observed in the present study, the thermal regime in such macro-scale systems will be covered in a few nanoseconds, and this is well beyond the temporal resolution of latest experiments. Besides, in previous experiments, which used an electrical method to study bridge growth during coalescence (Case and Nagel,

2008; Case, 2009; Paulsen *et al.*, 2011), the electrostatic interactions between the droplets may have changed the initial geometry and so the extent of the thermal regime itself.

A previous droplet coalescence study using molecular dynamics failed to notice the existence of the thermal regime due to low-resolution measurements (Pothier and Lewis, 2012). In the present study, the effect of molecular thermal motion is analysed not only in initiating coalescence, but also in the subsequent bridge growth. Droplet coalescence using a different molecular model of water: the mW (Molinero and Moore, 2009) model is also studied and the results are qualitatively unchanged. There are quantitative differences, in particular, in the bridge growth speed, which justifies using a computationally expensive, but more accurate TIP4P/2005 model for the major portion of our studies.

As pointed out in the beginning of this chapter, although the nanoscale amplitude of interfacial thermal fluctuations on pure liquid surfaces makes it difficult to observe the thermal-capillary waves experimentally, some experiments have observed them on the surfaces of ultra-low surface tension liquids (Aarts *et al.*, 2004). As for computational studies, thermal-capillary waves have already been incorporated into continuum analysis based on a fluctuating hydrodynamic theory to investigate stability of nanojets (Zhao *et al.*, 2019a). Moreover, the nature of bridge growth in the thermal regime is reminiscent of the interface disappearance exhibited by the computational model of droplet coalescence developed by Sprittles and Shikhmurzaev (2014c). Incorporating thermal fluctuations to this model to study macro-scale droplets coalescence seems to be a promising way forward. Such experiments and computational techniques will be capable of further verifying the existence of the thermal regime in droplet coalescence.

Chapter 4

Earliest transient dynamics of wetting

The work presented in this chapter is being drafted to be submitted to Nanoscale Horizons: *Perumanath, S., Chubynsky, M. V., Pillai, R., Sprittles, J. E., and Borg, M. K. Droplet spreading commences in a thermal-vdW regime. Nanoscale Horiz.*.

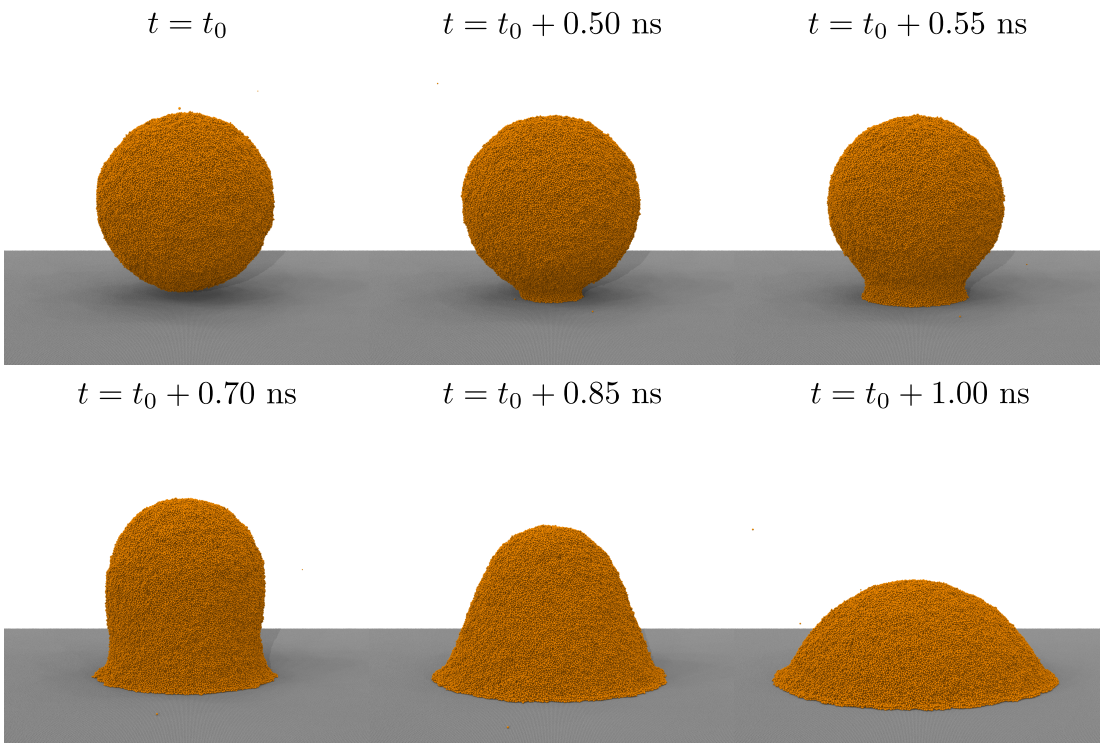

Figure 4.1: A spherical water nanodroplet of $R = 17.5$ nm spreading on a hydrophilic wall. After the first contact, the liquid molecules at the three-phase-zone jumps over the atoms of the underlying wall as described by molecular kinetic theory, taking the contact line further.

Numerous practical situations are conditioned by the spreading of a liquid on a solid substrate, such as treatments of plant leaves with pesticides (Bonn *et al.*, 2009), metal or glass coatings in industries (Simpkins and Kuck, 2003), painting, ink-jet printing (de Gans *et al.*, 2004) and self-assembly of nanoparticles (Brinker *et al.*, 1999; Vakarelski *et al.*, 2009). A liquid droplet coming in contact with a wettable surface spreads on it in order to minimise total interfacial energy in the system. During spreading, a liquid bridge connecting the spreading droplet to

the substrate develops in time after the first contact, until the system attains equilibrium. At this point, the liquid-solid contact angle will have come to rest at its minimum value, which is determined by the affinity of the spreading liquid towards the underlying substrate — the higher the affinity, the lower the equilibrium contact angle, θ_c.

The fundamental difficulty in numerically modelling droplet spreading is that the standard 'no-slip' boundary condition gives rise to divergences in energy dissipation and pressure near the three-phase-zone (TPZ), where the liquid, gas/vapour and the solid meet (Huh and Scriven, 1971; Dussan, 1979; de Gennes, 1985). There have been many attempts to solve this issue, particularly by suggesting alternative boundary conditions from a continuum fluid mechanics perspective (Huh and Mason, 1977; Hocking, 1976). Blake and Haynes (1969) explained the motion of the contact line (CL) as a result of a large number of individual molecular jumps occurring at the TPZ. In this way, they were able to suggest the existence of a 'contact line friction' near the TPZ, which helped us further understand the physical mechanism of CL motion in detail.

Nevertheless, the early stage dynamics of droplet spreading has still proved to be elusive. It is assumed that the capillary energy suddenly becomes available at a singular point in space and time, the moment a droplet touches a wettable substrate. Similar to the problem of droplet coalescence, it is reasonable to expect nanoscale forces to play a key role in removing this singularity. In this chapter, molecular simulations are used to study the initial dynamics of droplet spreading and provide an improved understanding of the entire process, such as the example in Fig. 4.1, which shows a water nanodroplet spreading on a partially wetting substrate. Similar to the previous chapter, here the focus is also on quasi-2D droplets. This chapter is organised as follows: several simulation details specific to this chapter are provided in Section 1. In Section 2, the molecular picture of contact line motion, widely known as the molecular kinetic theory (MKT) is discussed. It is crucial to understand the molecular mechanism of CL motion at the later stage in order to distinguish the early stage dynamics from it, which will be discussed in Section 3. In Section 4, the impact of this work is examined and possible future directions in which this work can move to are discussed.

4.1 Simulation details

In this chapter, the mW model (Molinero and Moore, 2009) of water is used in order to study the early stages of droplet spreading on a substrate. Since how the interaction between the substrate and the liquid affects the CL motion is of interest, usage of a computationally expensive TIP4P/2005 model is not absolutely necessary in this case, as the solid-liquid interactions are usually modelled identically (using LJ potential) irrespective of the water model used.

A pre-equilibrated quasi-2D mW water droplet of radius $R = 29.8$ nm (at $T = 300$ K) is placed roughly 2 nm above the substrate and is brought towards the wall by imposing a net velocity of

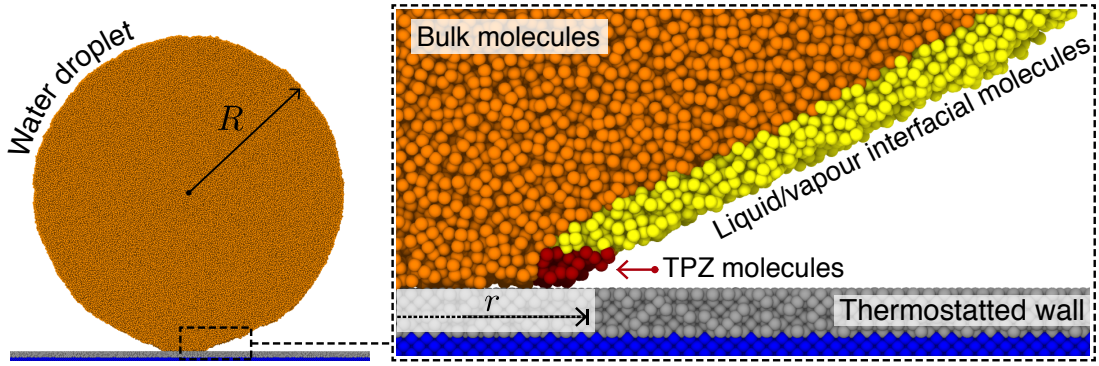

Figure 4.2: Geometry of the problem studied here. A thermostat is applied only to the top few layers (grey) of the wall ($T = 300$ K). Wall atoms in the remaining layers underneath (blue) are fixed. Location of the contact point r on both sides is measured from the initial location of the centre-of-mass of the droplet.

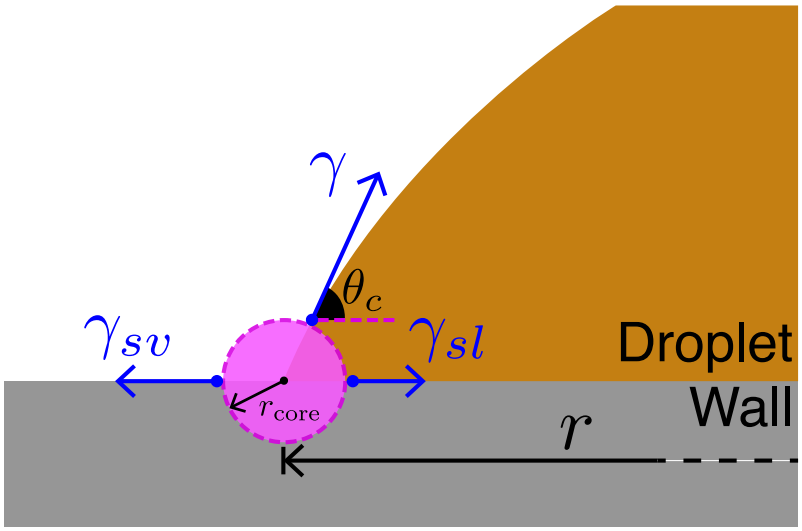

Figure 4.3: Dependence of equilibrium contact angle θ_c on solid-liquid intermolecular energy parameter ε_{SL} normalised with mW liquid-liquid energy parameter $\varepsilon_{LL} = 6.189$ kcal/mol.

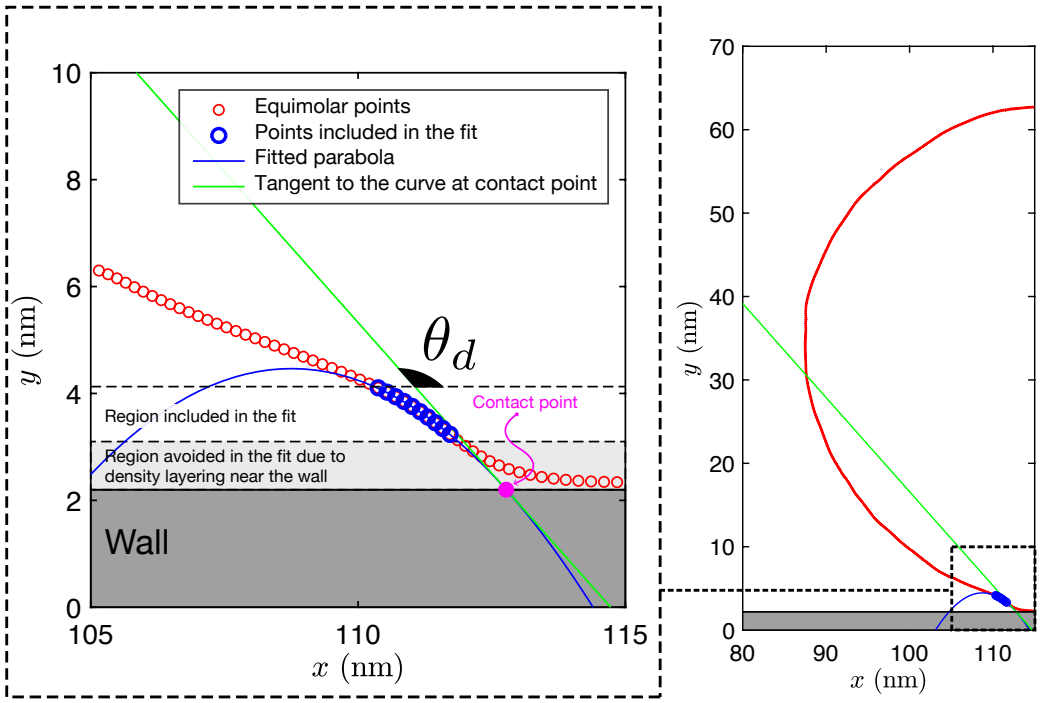

Figure 4.4: Definition of the dynamic contact angle (θ_d) and the corresponding location of the contact point. A parabola fit is used in order to deal with the strong interface bending close to the wall, which occurs in the early stages.

1 m/s to it. Figure 4.2 shows the geometry of the problem studied in this chapter. A Berendsen thermostat is applied to a few layers on the top of the substrate and the atoms in the rest of the layers underneath are fixed in order to maintain the integrity of the entire substrate. The droplet will come in contact with the substrate and spread to an equilibrium configuration that depends on the solid-liquid interaction parameter, ε_{SL}. Figure 4.3 shows how ε_{SL} determines the equilibrium contact angle of a quasi-2D droplet spreading on a substrate. The variation is linear until θ_c becomes 0°, in which case the droplet completely wets the solid substrate. For quasi-2D cylindrical droplets, θ_c does not depend on the size of the droplets as the CL curvature is zero. A sample LAMMPS code for this case is provided in Appendix E.

While studying the dynamics of the droplet spreading problem, the dynamic contact angle θ_d is evaluated in a way that is slightly different from previous researches. The most widely used method in determining the contact angle is by fitting a line to a group of interfacial points of the droplet above the surface. It is recommended to discard a few immediate layers (~ 0.6 nm) just above the surface in order to avoid complications that might arise due to layering of the liquid close to the wall, as described in Chapter 2. In the next few layers, instead of fitting a line to the interfacial points, a parabola is fit. The main motivation for using a second degree polynomial for the fit is to account for the strong interface bending close to the TPZ, especially in the early stages of spreading.

This method reproduces the contact angle data obtained using the method of line fitting instead, when there is negligible interface bending close to the wall. The location where this curve intersects the top layer of the wall is designated as the instantaneous contact point and the rate at which this point moves on the surface directly gives the CL velocity, V_{CL}.

4.2 Contact line motion – MKT

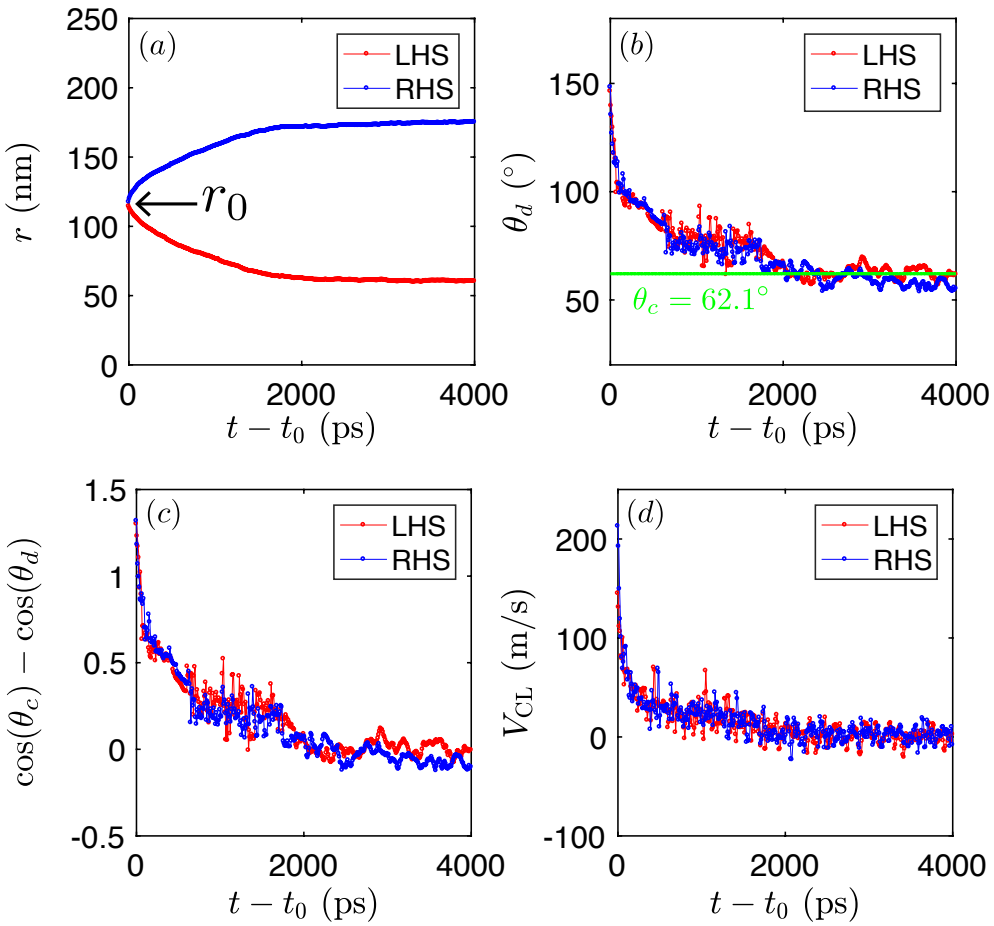

Figure 4.5: Variation of (a) location of contact point, r, on both sides and (b) dynamic contact angle, θ_d, as a quasi-2D droplet ($R = 29.8$ nm) spreads on a hydrophilic wall. Here, r_0 is the location of the projection of centre-of-mass of the droplet on the wall before spreading begins. Spreading need not start at r_0. As the system approaches its equilibrium state, (c) the deviation of cosine of θ_d from that of θ_c approaches zero along with (d) the CL velocity. A C++ code is written in order to identify the location of contact line and the value instantaneous contact angle.

MKT describes the contact line motion as a consequence of a large number of individual jumps of the molecules belonging to the liquid phase on top of the potential energy landscape formed by the substrate atoms (see Fig. 1.8 in Chapter 1). Due to the thermal motion of the liquid

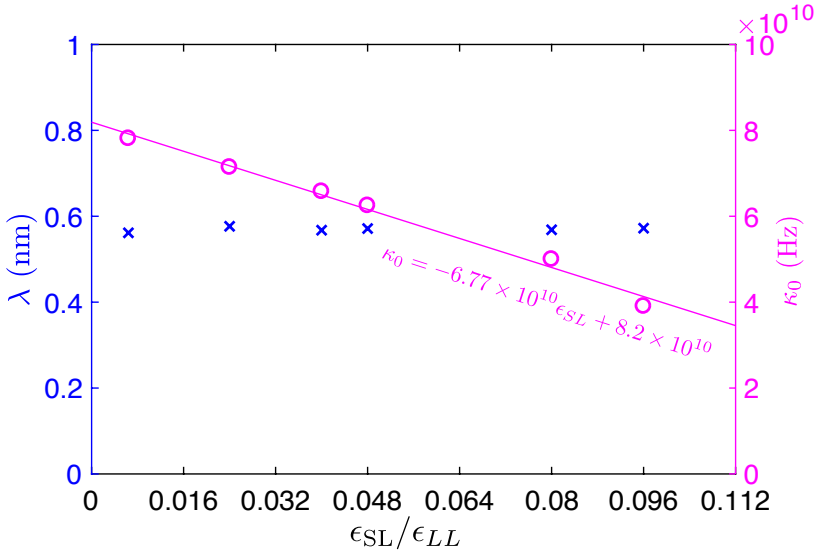

Figure 4.6: Variation of MKT parameters λ and κ_0 with $\varepsilon_{SL}/\varepsilon_{LL}$. While λ is independent of the wetting parameter, κ_0 decreases linearly with increasing ε_{SL}.

molecules coupled with the force which drives the wetting process, they traverse the energy landscape until an equilibrium configuration is achieved. Their motion is characterised by an average distance of their jumps (λ) and the equilibrium frequency of such jumps (κ_0). Figure 1.9 schematically shows how the CL advances due to several molecules at the TPZ jumping over the sites of wall atoms and shows the definition of λ. This physical mechanism underpinning the CL motion is the foundation of MKT, and so later this definition is referred back in order to distinguish it from another regime of dynamic wetting during droplet spreading, which these simulations reveal for the first time.

Blake and Haynes (1969) assumed that the driving force during spreading is the out-of-balance surface tension force, $\gamma[\cos(\theta_c) - \cos(\theta_d)]$, and the work done by it is spent entirely in modifying the potential energy landscape over the surface, so that there is net motion in the direction of applied force. Under such circumstances, the CL velocity will be given by

$$V_{\mathrm{CL}} = 2\kappa_0\lambda \sinh\left(\frac{\gamma[\cos(\theta_c) - \cos(\theta_d)]}{2nk_BT}\right), \tag{4.1}$$

where n is the number of adsorption sites per unit area. Further details of this model are provided in Chapter 1. Figure 4.5(a) shows the evolution of contact point in the MD simulations conducted here and Fig. 4.5(b) shows the dynamic contact angle as a function of time when a quasi-2D droplet of $R = 29.8$ nm spreads on a hydrophilic surface with $\theta_c = 62.1°$. For all cases of θ_c, V_{CL} is evaluated along with the deviation of cosine of θ_d from that of θ_c in order to compare their functional inter-dependence to Eq. (4.1).

It is interesting to note that, under the assumptions made in developing MKT, only the equilib-

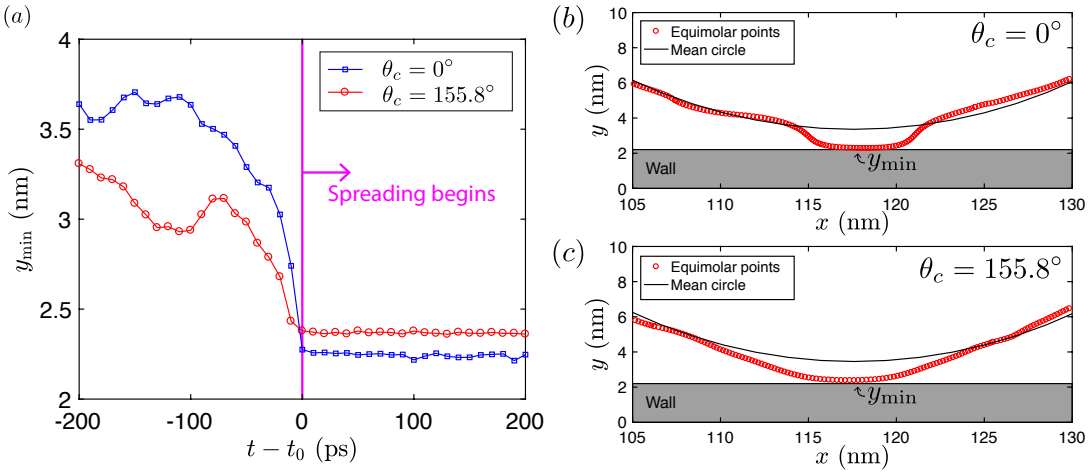

Figure 4.7: (a) Approach of the lowest point on the equimolar points at the droplet interface towards the wall. When there is higher solid-liquid interaction (lower θ_c), the approach is faster as indicated by the slope of $y_{\min}$ vs. $t - t_0$ graph just before the beginning of spreading. At small θ_c, the density layering close to the wall is severe and consequently, $y_{\min}$ settles at a lower point after $t = t_0$ than where it settles when θ_c is higher, where density layering is only moderate/negligible. Droplet profile close to the wall at $t = t_0$ for (b) complete spreading ($\theta_c = 0°$) and (c) superhydrophobic case ($\theta_c = 155.8°$). There are characteristic differences in the local profile of the droplet in both cases. In the figures, the mean circle is drawn by placing its centre at the instantaneous centre-of-mass of the droplet.

rium jump distance (λ) and the equilibrium jump frequency (κ_0) affect the CL motion. Here, these MKT parameters are explicitly evaluated in order to independently verify whether droplet spreading follows Eq. (4.1) from MKT at all stages or not. In Fig. 4.6, the dependence of these parameters on ε_{SL} is shown. Jumping frequency linearly depends on the solid-liquid coupling in the range of ε_{SL} that is of interest. Here the length of all the jumps that occur parallel to the surface (Bertrand *et al.*, 2009) is evaluated. At higher coupling, the contact line friction increases, which results in a decrease in κ_0. The average jump distance λ, on the other hand, is found to be independent of ε_{SL}. This is because changes in ε_{SL} will not result in a change in the lattice spacing between the wall atoms (Bertrand *et al.*, 2009; de Ruijter *et al.*, 1999; Blake *et al.*, 1997). Since evaluation of λ involves contribution from all molecular displacements parallel to the wall, which are close to the wall, it is greater than the lattice spacing ≈ 0.39 nm.

4.3 Instability growth and the first contact

The free surface shape of a droplet can be assumed to be composed of a mean profile (*i.e.* a circle for quasi-2D droplets and a sphere for 3D droplets) and a fluctuating part that arises from the interfacial thermal fluctuations. The free surface shape can be decomposed into a number of orthogonal modes of various wave numbers; Fourier modes for quasi-2D droplets and spherical harmonics for 3D droplets. As the droplet approaches the wall, a set of modes of

the interfacial thermal fluctuations on the surface of the droplet with wavelengths larger than a critical value will grow exponentially. This growth occurs since the increase in free energy due to the increase in surface area is smaller than the decrease in free energy owing to the attraction between the droplet interface and the substrate.(Vrij, 1966; Vrij and Overbeek, 1968) The rate at which these modes grow depends on the strength of attraction from the wall — quantified by the Hamaker constant (A_H) between the droplet interface and the wall (which in turn, depends on ε_{SL}). Using an analysis presented in Appendix F, the conditions under which an instability can develop to make a contact between two interfaces are examined:

$$\sigma_{\max}(H)\frac{H}{v} > 1, \tag{4.2}$$

where

$$\sigma_{\max} \approx \left(\frac{4a_H^3}{27\gamma\rho^2}\right)^{1/4}, \; a_H = \frac{A_H}{16\pi H^4}, \tag{4.3}$$

$\sigma_{\max}$ is the maximum growth rate of the available wave numbers, ρ is the liquid density and μ is its dynamic viscosity. H is half the distance between approaching interfaces, which is ~ 1 nm (the typical size of fluctuations on droplet surface) as a droplet approaches the wall and v is the approach speed. By substituting relevant parameters in the above equations, it can be shown that Eq. (4.2) is satisfied in all cases considered in this work, indicating that the role of thermal capillary waves is significant in establishing the first contact between the droplet and the substrate. Although the above relations are derived for two approaching planar interfaces, we expect them to be applicable for the case of droplets approaching a substrate before wetting as $H/R \ll 1$.

Figure 4.7(a) shows the approach of the lowest point at the droplet interface closest to the wall as a result of the instability growth in two cases: complete wetting ($\theta_c = 0^\circ$) and on a superhydrophobic surface ($\theta_c = 155.8^\circ$). Once these interfacial points are significantly within the region of influence of the wall, they approach the wall at different speeds, as indicted by the slopes of the plots in Figure 4.7(a). When ε_{SL} is higher, this approach is faster because of the larger intermolecular force experienced by the fluid atoms. As they reach the wall at $t = t_0$, the lowest point on the droplet interface $y_{\min}$, establishes the first contact with the substrate. For highly wettable surfaces, the density layering close to the wall is severe, and consequently, the value of $y_{\min}$ after t_0 is closer to the wall than it is when wettability is lower, where density stratification is only moderate/negligible.

4.4 Early stage dynamics of contact line motion

After the first contact is established (see Figs. 4.7(b,c)), we investigate the dynamics of wetting at its early stages by studying the motion of interfacial liquid molecules on the droplet surface. Surprisingly, the way in which the CL advances during droplet spreading is completely different in its early stages from what is envisioned by MKT. Figs. 4.8 and 4.9 show snapshots

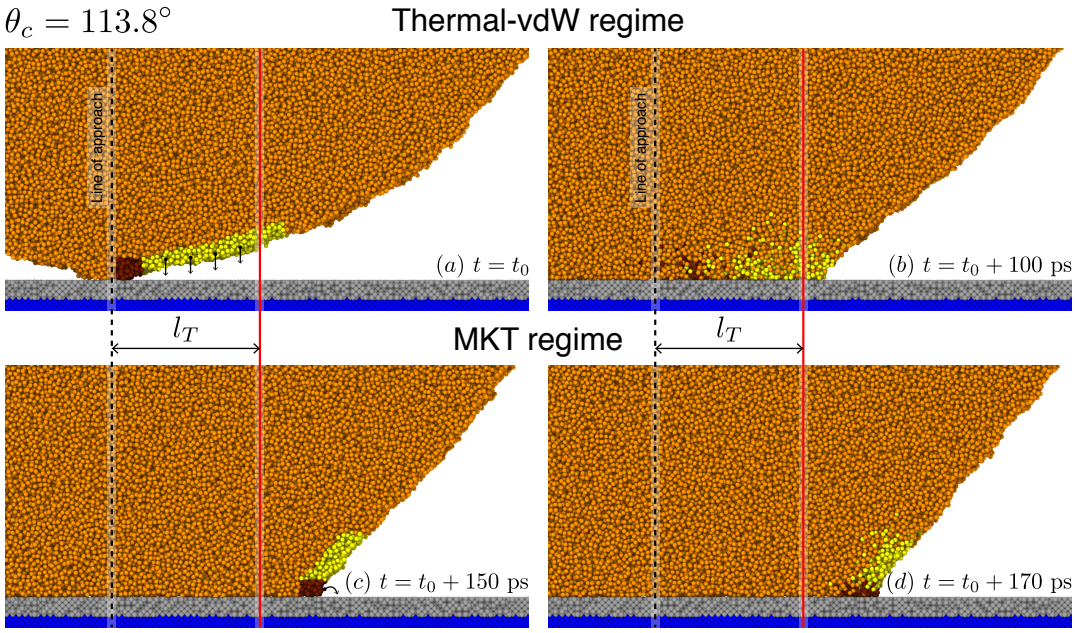

Figure 4.8: Simulation snapshots showing how the contact line proceeds at different stages of droplet spreading when $\theta_c = 113.8^\circ$. In the initial stages, interfacial molecules (yellow) get directly deposited on to the substrate. After the contact line passes l_T, contact line proceeds in a way that is suggested by MKT.

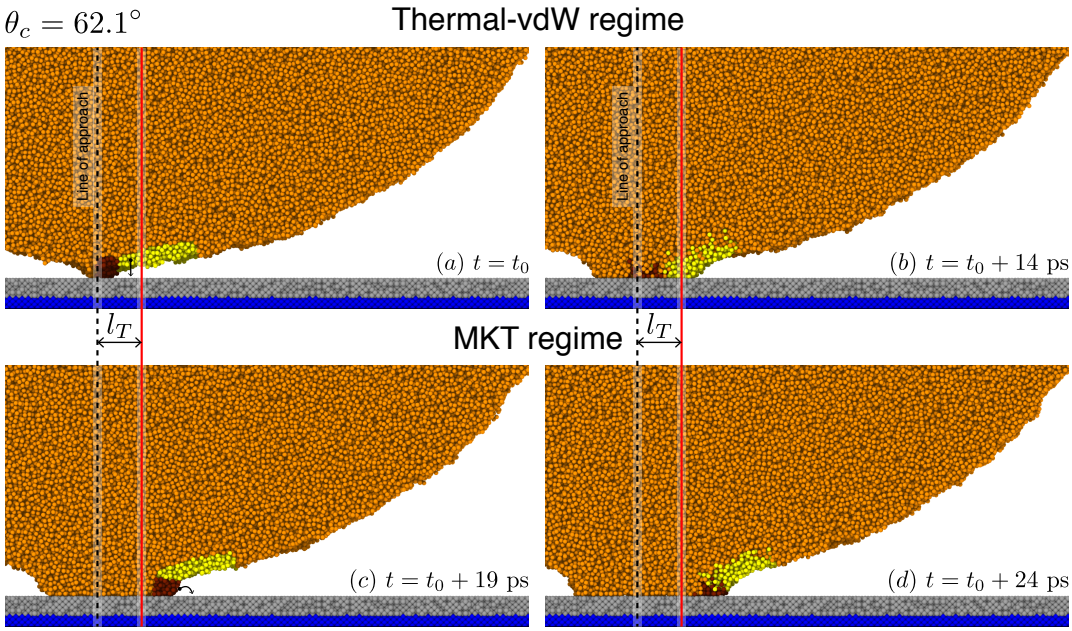

Figure 4.9: Similar to Fig. 4.8, but for $\theta_c = 62.1^\circ$. l_T for this case is observed to be less than that of the $\theta_c = 113.8^\circ$ case.

of simulations where a droplet spreads on a surface — the equilibrium contact angles are $\theta_c = 113.8^\circ$ and $\theta_c = 62.1^\circ$, respectively. Similar to the discussion of 'thermal regime' in droplet coalescence analysed (see Chapter 3), during the initial stages of droplet spreading, the contact line advances in a *thermal-vdW* regime. It is termed in this way, because unlike the MKT, both the thermal capillary waves *and* the effect of van der Waals forces between the solid and liquid play a role in the initial dynamics.

This new thermal-vdW regime is also characterised by interfacial molecules (yellow ones) jumping across the gap between the droplet surface and the underlying wall (see Figs. 4.8(a,b) and 4.9(a,b)). In this regime, the CL motion resembles how a caterpillar vehicle moves on a ground, i.e. by a rolling type motion. The CL is found to advance in this manner until it reaches a distance l_T (the proposed thermal length scale) from the line of approach, which passes through the centre-of-mass of the droplet before the beginning of spreading. Here, l_T is determined in a similar way as described in the previous chapter: the interfacial molecules near the TPZ (i.e. just above the wall) are identified at a particular instant. The fraction of these TPZ molecules, which came from the TPZ at a previous instant is then determined. If this fraction is greater than 0.5, which means the majority of the molecules at the present TPZ came from the previous TPZ by jumping over the substrate atoms, the base radius is considered to be in an MKT regime. And if the fraction is less than 0.5, meaning the majority of the molecules at the present TPZ came from the free interface of the droplet, the base radius is considered to be in the thermal-vdW regime. The point where this fraction crosses over the half way mark of 0.5 is designated as the extent of the thermal-vdW regime.

The CL motion within l_T is observed to be linear in time, as it is for droplet coalescence (see Fig. 4.10), with V_{CL} being a decreasing function of θ_c. This constant velocity motion removes the singularity in the beginning of droplet spreading.

Figure 4.11(a) shows how l_T depends on the equilibrium contact angle, θ_c, for a quasi-2D droplet of $R = 29.8$ nm. l_T is evidently dependent on the solid-liquid interaction energy ε_{SL}. The initial intuition is that a low ε_{SL} (such as that of a hydrophobic surface) inhibits the free interface molecules of the droplet from getting directly deposited on to the wall in the thermal-vdW regime. Correspondingly, l_T is expected to be small at low ε_{SL}. This would mean l_T being an decreasing function of θ_c. However, counter-intuitively, Fig. 4.11(a) shows that l_T behaves in the opposite manner, and is actually an increasing function of θ_c. This is explained from further measurements from the MD simulations.

As the droplet approaches the wall, a set of modes of the interfacial thermal fluctuations on the surface of the droplet begin to grow owing to the attraction from the wall. The rate at which these modes grow depends on the strength of attraction from the wall i.e. ε_{SL}. Figure 4.7(a) shows the approach of the lowest point at the droplet interface towards the wall in two cases: complete spreading ($\theta_c = 0^\circ$) and on a superhydrophobic surface ($\theta_c = 155.8^\circ$). Once these interfacial points are significantly within the region of influence of the wall, they approach

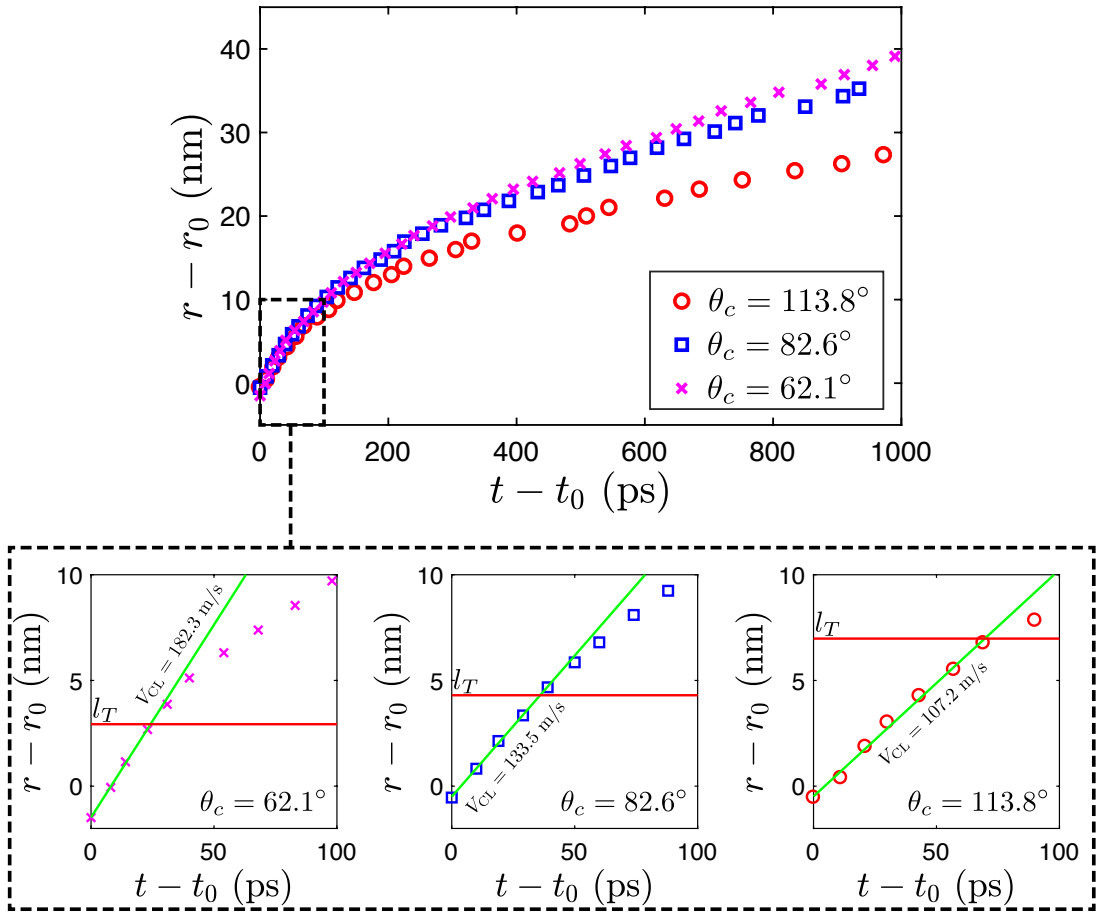

Figure 4.10: Variation of location of contact point measured from r_0. The CL motion within l_T is linear in time with V_{CL} increasing with decreasing θ_c.

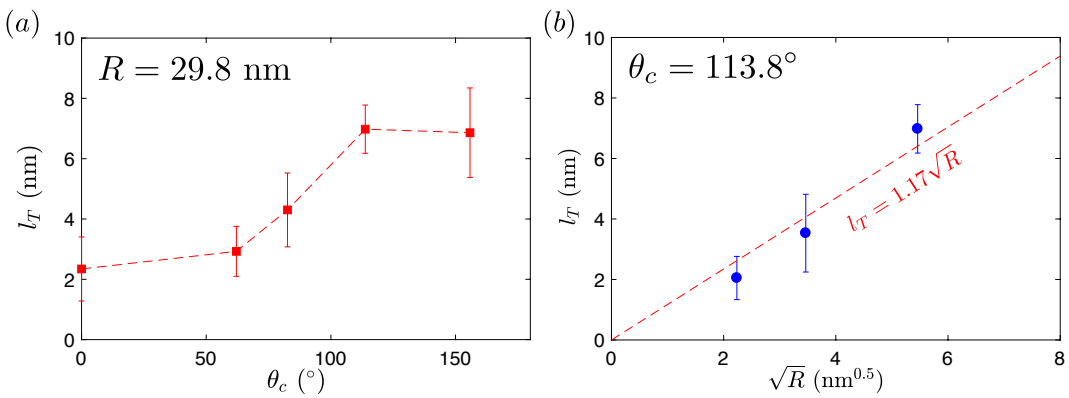

Figure 4.11: (a) Variation of the extent of the thermal-vdW regime, l_T with equilibrium contact angle θ_c. (b) Variation of l_T with size of the droplets. l_T seemingly scales as $\sqrt{R}$.

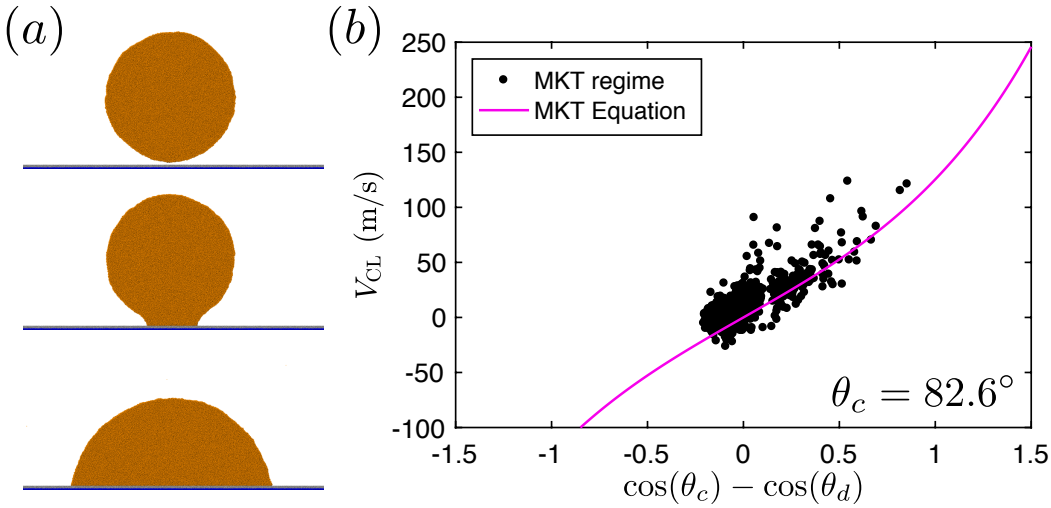

Figure 4.12: (a) MD simulation snapshots and (b) variation of V_{CL} with $\cos(\theta_c) - \cos(\theta_d)$ when $\theta_c = 82.6°$.

the wall at different speeds. As they reach the wall at $t = t_0$, the lowest point on the droplet interface y_{min}, remains approximately constant. It has to be noted that depending on ε_{SL}, there are characteristic differences in the local profile of the droplets in both cases, as indicated by Figs. 4.7(b) and 4.7(c). In the complete spreading case, a local radius of curvature at the TPZ is higher compared to that in the superhydrophobic case. Consequently, the remaining free interface of the droplet is further away from the wall in the complete spreading case (Fig. 4.7(b)) than it is in the superhydrophobic case (Fig. 4.7(c)). Accordingly, more liquid molecules from the remaining droplet interface will approach the wall in the initial stages of spreading, when θ_c is larger, resulting in a larger value of l_T. In all cases, CL motion continues in this manner until l_T, after which the dynamics is dominated by a large number of individual molecular displacements, as described by MKT.

Furthermore, as a circular profile of radius R approaches a planar interface, the gap between the surfaces scales as $r^2/2R$. Here, at a given ε_{SL}, all molecules that lie within the influence of the solid wall (i.e. within r_c from the top layer of the wall) after the first contact will get deposited on the wall during the thermal-vdW regime. This process will continue until the contact point reaches $\pm l_T$ from the line of approach where the gap width, $l_T^2/2R \sim r_c$. Since r_c is kept constant throughout the simulations, $l_T \sim \sqrt{R}$ (see Fig. 4.11(b)) is expected, as it is in the case for droplet coalescence. As explained in Chapter 2, a large enough cut-off is used such that any interatomic interaction above r_c is negligibly small. Therefore, l_T is not expected to change appreciably at a higher r_c.

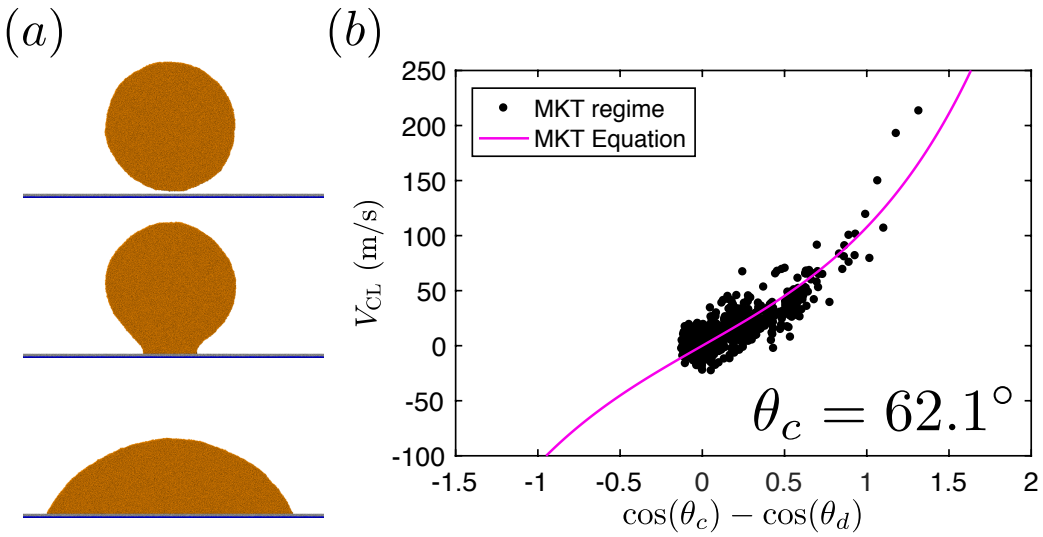

Figure 4.13: (a) MD simulation snapshots and (b) V_{CL} vs. $\cos(\theta_c) - \cos(\theta_d)$ for $\theta_c = 62.1°$. As θ_c is decreased, the thermal-vdW regime is not that far off from the MKT regime.

4.5 Discussion and outlook

The obvious difference in the molecular mechanism of base radius growth between the initial and later stages of wetting is the defining characteristic of the thermal-vdW regime identified in this work. During complete wetting, a precursor film only develops after the thermal-vdW regime. As seen in the simulation snapshots (Figs. 4.8(c,d) and 4.9(c,d)) in the later stage, the CL advances as a result of displacement of molecules belonging to the TPZ as described by MKT. The dynamics of the CL motion after l_T is compared with Eq. (4.1) and reasonable agreement is observed (see Figs. 4.12 – 4.13); the late stage of wetting is hence termed as 'MKT regime' in this work.

The mW water model used in the present analysis is one of the simplest models of water available in the literature. Similar to real water, this model exhibits low vapour pressure at 300 K, high surface tension and relatively high viscosity. The motivation for using such a simple model in the present chapter, apart from the improved computational savings, is that liquid-wall interactions are usually modelled in a similar manner, i.e. using the LJ potential, irrespective of the liquid-liquid interactions considered. Further validation of the thermal-vdW regime can be done by using a more accurate, but computationally expensive, TIP4P/2005 model of water. Here, the manner in which the individual molecular displacement parameters are evaluated must be revisited in order to acknowledge the structural complexities of this four site model.

The CL motion in the thermal-vdW regime during droplet spreading on a surface is strikingly similar to the bridge evolution in the thermal regime during droplet coalescence. In both cases, the thermal-capillary waves play a crucial role and a CL/bridge evolves due to collective molecular displacements into the intervening gap between the droplet and the wall/other droplet.

It may be the case that such a process of interface disappearance is common in the initial stages of many other natural and industrial processes, which have so far avoided rigorous analysis due to the presence of a singularity in their mathematical formulations. An innovative way of incorporating molecular effects within a hydrodynamic framework has been suggested by Shikhmurzaev (1997). Perhaps the thermal-vdW regime can be used to parametrise this model from a molecular perspective. Such accurate hydrodynamic analyses will be extremely beneficial in the numerical studies of many industrial applications.

Chapter 5

Molecular physics of jumping nanodroplets

The work presented in this chapter has been submitted to Nanoscale: *Perumanath, S., Borg, M. K., Sprittles, J. E., and Enright, R. Molecular physics of jumping nanodroplets. Nanoscale.*

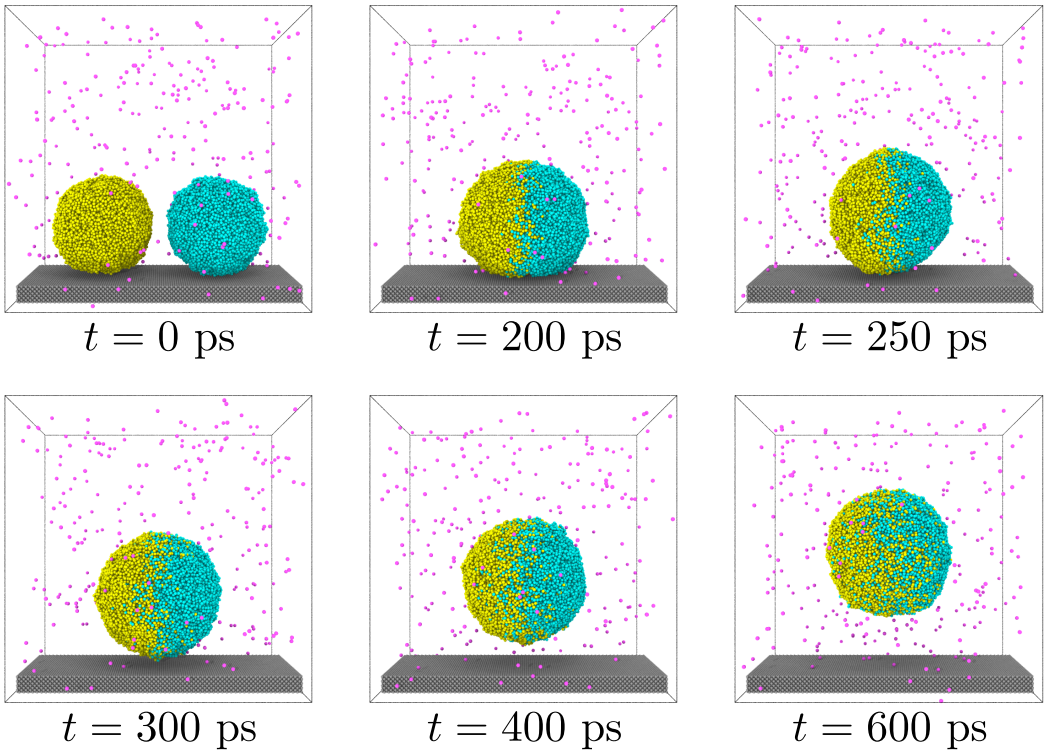

Figure 5.1: Coalescence-induced jumping of two water droplets (yellow, cyan) of $R = 7.2$ nm from a superhydrophobic surface in a nitrogen atmosphere (magenta).

The coalescence-induced jumping phenomenon of nanodroplets on superhydrophobic surfaces is a promising candidate in heat transfer and self-cleaning applications without the necessity of any moving parts. In condensation heat transfer, drop-wise condensation has high phase-change heat transfer performance when compared to film-wise condensation (Rose, 2002),

provided that these droplets are rapidly removed from the condensing surface, leaving space for re-nucleation. Traditionally, gravity is used for the removal of droplets from an inclined or vertical plate (Kim *et al.*, 2002; Dimitrakopoulos and Higdon, 1999), but the droplet radius has to be larger than the capillary length $l_\gamma = \sqrt{\gamma/\rho_l g}$, where g is the acceleration due to gravity; sub-millimetre sized water droplets cannot be dislodged by gravity.

Recent experimental studies have shown that smaller droplets can be removed from superlyophobic surfaces (with contact angle $\theta_c \geq 150^\circ$ and negligible contact angle hysteresis) by a self-induced jumping mechanism (Boreyko and Chen, 2009). This occurs when condensate droplets grow until they coalesce with neighbouring droplets, which results in the final droplet jumping off the surface. This rapid self-coalescence and consequent lift-off behaviour of the droplets results from the excess surface energy released after coalescence getting partially converted into kinetic energy of the final droplet. Since the original breakthrough, there have been many studies on this topic attempting to understand the underlying dynamics of the process (Miljkovic *et al.*, 2013; Enright *et al.*, 2012; Boreyko and Collier, 2013; Enright *et al.*, 2013; Nam *et al.*, 2013) and enhance jumping speed in various ways (Gao *et al.*, 2018; Vahabi *et al.*, 2018; Wang *et al.*, 2016). Interestingly, nature has already been utilising this phenomena for self-cleaning of cicada wings (Wisdom *et al.*, 2013) and plant leaves (Mockenhaupt *et al.*, 2008), and in dew droplet removal from gecko skin (Watson *et al.*, 2011).

During coalescence of two droplets, after the rupture of the intervening fluid film, a liquid bridge will form, which grows quickly, hits the underlying surface and provides a reaction force for the final droplet to jump (see Figure 5.1) (Enright *et al.*, 2014). Previous numerical and experimental studies have shown that while the jumping process is limited by gravity for droplets with $R \sim l_\gamma$ (Peng *et al.*, 2013), it is suppressed by internal viscous dissipation for smaller ones (Wang *et al.*, 2011; Enright *et al.*, 2014). Therefore, the jumping speed V_g (where the subscript g denotes 'coalescence in the presence of a gas') is expected to be a non-monotonic function of R and its maximum is observed to be $\approx 0.25U$ (Mouterde *et al.*, 2017; Boreyko and Chen, 2009; Enright *et al.*, 2014; Liu *et al.*, 2014) for $R \approx 100$ μm (Boreyko and Chen, 2009) water droplets, where U is the inertial-capillary velocity scale. Notably, U is only a good predictor of V_g when viscous effects are negligible, which occurs when the *Ohnesorge number* $\mathrm{Oh}_l = \mu_l/\sqrt{\rho_l \gamma R}$ is sufficiently small.

Although jumping has been observed experimentally for water droplets with radii as small as $R \approx 500$ nm (Cha *et al.*, 2016), observing sub-micron scale droplets is highly challenging. This motivated researchers to use MD simulations to study jumping of nanodroplets (Gao *et al.*, 2018; Sheng *et al.*, 2017; Liang and Keblinski, 2015). A factor that is usually overlooked in such studies is the role of the ambient gas in the overall dynamics. Besides gas dynamics, there exist a host of other intricacies in this scenario such as slip at solid-fluid and fluid-fluid interfaces and interfacial thermal fluctuations. Clearly, modelling nanodroplet coalescence requires a method which can incorporate such nanoscale affects. In this chapter, MD is used

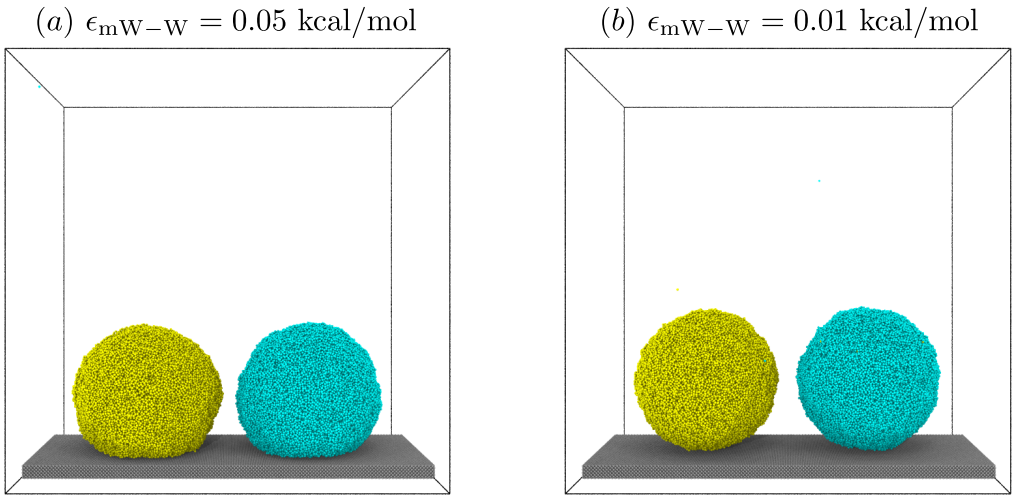

Figure 5.2: (a) Starting the MD simulations with two mW water droplets on top of a 'slightly' hydrophobic wall. (b) The same droplets after the water-solid interaction potential is decreased to create a superhydrophobic wall ($\theta_c \approx 170^\circ$).

to study the influence of nanoscale effects on the jumping characteristics of nanodroplets. This chapter is organised as follows: simulation details are provided in Section 1. In Section 2, the viscous dissipation in the droplets and adhesion from the surface are quantified. In Section 3, the effect of ambient gas on the jumping speed is studied. The influence of thermal capillary waves on nanodroplet jumping is analysed in Section 4. Finally, in Section 5, the impact of this particular chapter with respect to our existing understanding is discussed.

5.1 Simulation details

Molecular dynamics is, perhaps, the only computational technique that can simultaneously capture the spatio-temporal scales associated with rarefied gas flow and thermal fluctuations at a molecular scale that are currently beyond experimental capabilities, and understand their influence on nanodroplet jumping. In this chapter, water-based systems are primarily investigated using the coarse-grained mW model of water and mono-atomic argon systems are employed in order to compare with previous findings in the literature, as well as isolating the effect of the outer gas. Unlike argon, water has negligible vapour pressure at the operating temperature (300 K) and so the effect of outer fluid on jumping speed can be isolated by adding an insoluble gas outside the water droplets such as nitrogen. The simulation begins with two liquid droplets sitting on a 'slightly' hydrophobic wall (see Fig. 5.2(a)). The energy parameter between the wall and liquid molecules in the LJ potential is then reduced in small steps until the contact angle increases well above 150° (see Fig. 5.2(b)), which is then equilibrated for a further 5 ns. During this stage, a Berendsen thermostat is applied to the droplets and the time-integration

is performed with a timestep size of 0.01 ps for the water-based systems and 0.004 ps for the argon-based systems. The wall atoms are fixed to their initial lattice coordinates. After equilibration, an impact speed (2 m/s) is imparted to each droplet towards the other, which is sufficiently small to avoid having any influence on the jumping dynamics (Liang and Keblinski, 2015). This procedure is repeated under various ambient conditions for different droplet sizes. A large number (30) of independent realisations are performed for each case in order to obtain statistical reliability. The results are also compared with predictions of 3D continuum volume-of-fluid (VoF) simulations in order to get a comprehensive picture of the size dependence of the jumping speed. Details of the VoF simulations are provided in Appendix G.

In order to characterise the role of outer gas on jumping speed, a Knudsen number based on the mean-free-path of the surrounding gas and the droplet radius, i.e. Kn = λ/R is defined. Here, the mean-free-path is evaluated using the hard sphere model:

$$\lambda = \frac{\mu_g}{p_\infty}\sqrt{\frac{\pi k_B T}{2m}}, \tag{5.1}$$

where m is the mass of a single gas molecule and μ_g is the gas viscosity. The vapour pressure of argon at $T = 85$ K is so high that Kn is very low (see Fig. 1.10). Correspondingly, jumping speeds in such cases are represented by V_g, where subscript 'g' indicates 'in the presence of a gas'. In stark contrast, the jumping of mW water droplets is represented by V_v, where subscript 'v' indicates 'in vacuum', because the vapour pressure of water at $T = 300$ K is so low that Kn is very large for all cases (Kn $\gg 10$). For water droplets coalescing in nitrogen, however, V_g is used to denote jumping speeds.

5.2 Jumping speed in vacuum

Studying nanodroplet coalescence in vacuum, where the process is adiabatic, will allow us to isolate the coalescing liquid's dynamics during the process, so that a comparison with coalescence of argon droplets or water droplets surrounded with nitrogen will help us identify the role of the outer gas/vapour.

When two droplets coalesce, energy is released as the total interfacial area decreases. A portion of this energy released is dissipated due to viscosity of the coalescing droplets (E_μ). The remaining portion of the total energy budget is utilised to overcome the adhesion from the surface (W_{adh}), generate a flow field inside the droplet after coalescence that does not contribute to jumping ($E_{\text{circulation}}$) and convert it into the kinetic energy (KE) of the final droplet (if it jumps off the symmetry breaking superlyophobic surface), i.e.

$$\gamma \Delta A = W_{\text{adh}} + W_{\text{flow}}, \tag{5.2}$$

$$W_{\text{flow}} = E_\mu + \text{KE} + E_{\text{circulation}}, \tag{5.3}$$

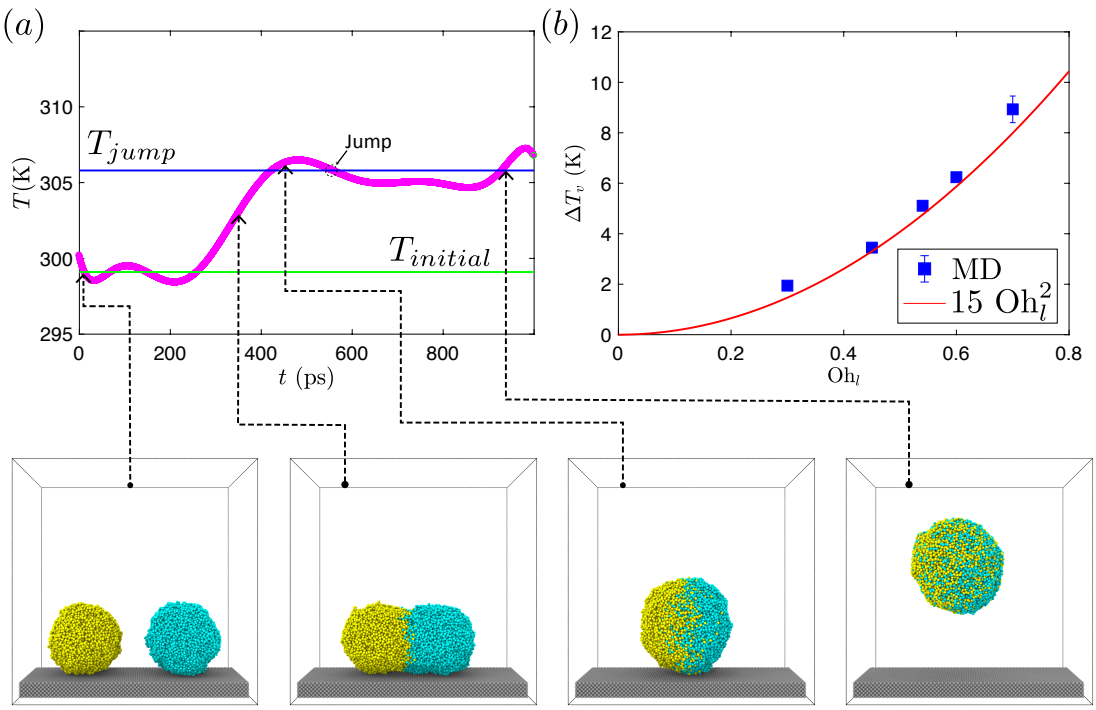

Figure 5.3: (a) Temperature rise during coalescence of two water nanodroplets ($R = 4.1$ nm, $\mathrm{Oh}_l = 0.6$) in vacuum and corresponding simulation snapshots. (b) Comparison of the temperature rise ($\Delta T = T_{jump} - T_{initial}$) obtained from MD simulations with Eq. (5.5) for various droplet sizes (or Oh_l).

where $\Delta A = 4\pi R^2(2-2^{2/3})$ is the reduction in the surface area when a sphere is rapidly formed. It is worth noting here that W_{adh} is of the order of KE (see next section).

At the point where the droplet leaves the surface, W_{flow} is composed of the viscously dissipated flow component E_μ, the translational kinetic energy KE, and what is left of the incoherent flow within the droplet $E_{\mathrm{circulation}}$ that is also viscously dissipated quickly after the jump point. The energy spent due to viscous dissipation results in an increase in the average temperature over the entire coalescing droplets and is given by $2m_d c_p \Delta T_v$, where $m_d = 4\pi R^3 \rho_l/3$ is the mass of a single droplet of radius R, c_p is the specific heat capacity of the coalescing liquid, $\Delta T_v = T_{jump} - T_{initial}$ is the temperature rise during coalescence, with subscript 'v' representing processes occurring in vacuum, T_{jump} is the temperature of the final droplet when it takes off the non-wetting surface and $T_{initial}$ is the initial temperature of the droplets. In Fig. 5.3(a), the variation of temperature with time during coalescence of two water nanodroplets and the corresponding simulation snapshots are shown. Notably, temperature is far easier to measure in MD than directly computing viscous dissipation from gradients of the flow fields.

For nanodroplets, the coalescence process is largely viscous dominated and by noticing that the temperature of the final droplet does not increase appreciably after jumping happens, the energy associated with the circulatory flow field inside the droplets is assumed to be negligible

($E_{\text{circulation}} \approx 0$). Eq. (5.2) therefore changes to

$$\gamma\left[4\pi R^2(2-2^{2/3})\right] = W_{\text{adh}} + 2m_d c_p \Delta T_v + m_d V_v^2. \tag{5.4}$$

Rearranging the terms for temperature rise gives:

$$\Delta T_v = \left(1.24 - V_v^{*2} - \frac{W_{\text{adh}}}{m_d U^2}\right)\frac{(\gamma/\mu_l)^2}{2c_p}\text{Oh}_l^2. \tag{5.5}$$

In the above equation, $V_v^* = V_v/U$ is the jumping speed in vacuum normalised with U. With $V_v^{*2} \ll 1$, $W_{\text{adh}} \sim KE$ (see below) and inserting the properties of mW water, Eq. (5.5) simplifies to $\Delta T_v(\text{K}) \approx 15\ \text{Oh}_l^2$. As one would expect, viscous dissipation increases as the 'dimensionless viscosity (Oh_l)' increases. In Fig. 5.3(b), the temperature rise measured from MD simulations is compared with the above equation, and their closeness validates the assumptions made.

5.3 Jumping speed in presence of a gas

The physics may be widely different, when the droplets are surrounded by a gas. Since γ is a weak function of the pressure outside the droplets (p_∞), the total energy budget of the system in the presence of a gaseous atmosphere can be assumed to be the same as that in the absence of it. However, during the coalescence process, a part of the energy budget is spent in order to overcome the drag from the ambient gas. The energy balance in this case is modified to:

$$\gamma\Delta A = W_{\text{adh}} + 2m_d c_p \Delta T_g + m_d V_g^2 + W_{\text{drag}}, \tag{5.6}$$

where ΔT_g is the increase in temperature of the droplets, V_g is the jumping speed in the presence of gas and W_{drag} is the work done against drag during the time both droplets coalesce.

A separate set of MD simulations are performed on argon droplets to determine the share of W_{adh} in the overall energy balance. Figure 5.4 shows the variation of $V_g^* \equiv V_g/U$ as a function of argon-wall energy parameter, $\varepsilon_{\text{Ar-W}}$. The major effect of adhesion is in changing the jumping speed by a factor of ~ 1 in the range of ε investigated (where θ_c is well above 150°). This infers that $W_{\text{adh}} \sim KE$. This is further verified by evaluating W_{adh} directly from MD simulations and comparing its value with KE of corresponding cases. For this purpose, all the liquid molecules lying within a distance of $r_c = 1.3$ nm from the top layer of the wall at the starting point of the simulation are considered. Their total LJ potential energy due to their interactions with substrate atoms are then evaluated, which will give a measure of the work of adhesion in the system. W_{adh} evaluated in this manner is of the order of final droplet jumping KE (typically $\sim 1 \times 10^{-19}$ J or lower), and both of these are observed to be small compared to the energy budget and viscous dissipation terms ($\approx 5 \times 10^{-18}$ J).

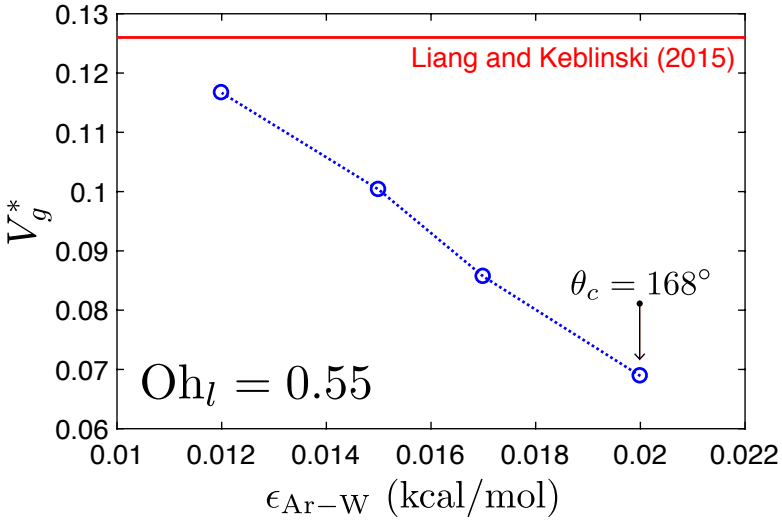

Figure 5.4: The effect of adhesion on jumping speed for coalescing argon droplets ($R = 13.3$ nm). The results of Liang and Keblinski (2015) seems reproducible at lower $\varepsilon_{\mathrm{Ar-W}}$. For argon droplets, $\varepsilon_{\mathrm{Ar-W}} = 0.02$ kcal/mol is used in order to avoid complications like premature lift-off due to increased thermal fluctuations.

It is further observed that smaller droplets lose contact with the wall at low values of ε, due to increased effects of thermal fluctuations. Since nanodroplets smaller than those investigated in previous studies are considered here, a system-specific single value of ε between wall and the fluid is used: $\varepsilon_{\mathrm{mW-W}} = 0.01$ kcal/mol and $\varepsilon_{\mathrm{Ar-W}} = 0.02$ kcal/mol. Furthermore, W_{adh} is assumed to be independent of the outer conditions, as no discernible changes in the coalescing droplet geometry is observed during the process (see Figs. 5.9 below).

From MD simulations, $\Delta T_g \approx \Delta T_v$ (see Figure 5.5(a)), indicating that the internal viscous dissipation during the coalescence of nanodroplets is not drastically affected by the presence of

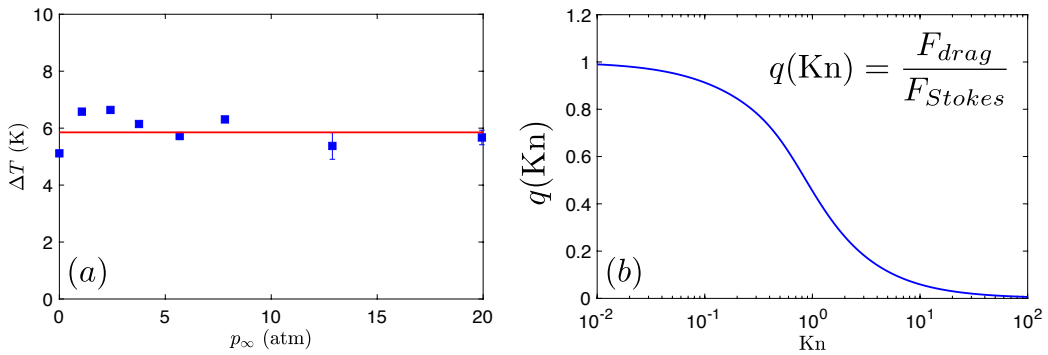

Figure 5.5: (a) Temperature rise during coalescence of two water nanodroplets with $R = 5.1$ nm as a function of ambient pressure. ΔT is observed to be independent of p_∞. (b) Variation of drag on small spheres for a wide range of Kn as suggested in Phillips (1975).

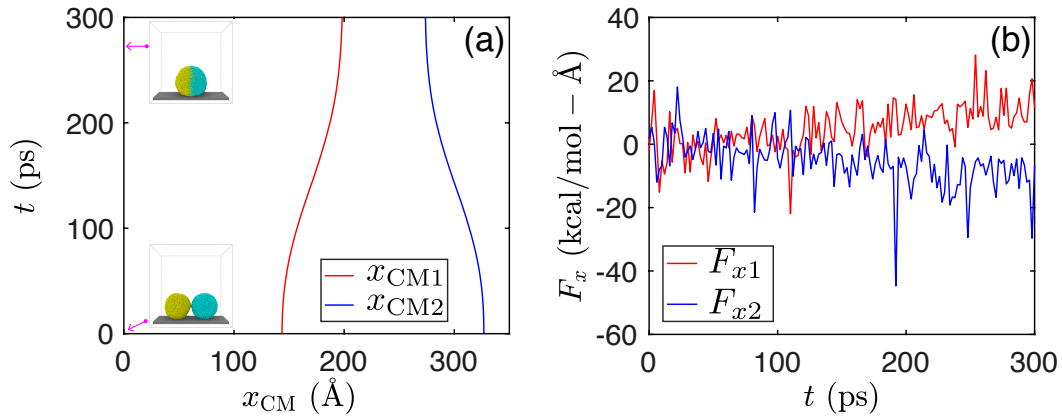

Figure 5.6: (a) Motion of the droplet centres-of-mass during coalescence. (b) The *total force* on each droplet along their line-of-approach (x) direction from the gas molecules during coalescence determined from MD.

a gaseous medium outside, i.e. heat transfer from the liquid to the outer gas phase is negligible over the time-scale of the process.

Drag on coalescing droplets

In order to solve Eq. (5.6) for V_g, a good way of estimating the contribution of W_{drag} is required. Like pressure, shear stress and temperature, a 'man-made' parameter like W_{drag} must also have a microscopic description. In other words, evaluating forces directly from the simulation and multiplying it with corresponding displacements is the most obvious and the first option to quantify W_{drag} through a particle-based simulation tool like MD. Fig. 5.6(a) shows the motion of centres-of-mass of both droplets and Fig. 5.6(b) shows the *total force* from the gas along their line-of-approach (x) experienced by each of the droplets. Coalescence of droplets with $R = 7.2$ nm at the lowest Knudsen number simulated is considered for good statistics. Even for a system with relatively low Kn, direct force evaluations from MD is very noisy as shown in the figure. Nevertheless, it is interesting to note that the total force F_x on each droplet is directed in such a way that it aids the coalescence process. For quantifying the drag, the motion of both droplets in the other two directions must also be considered. The forces in y and z directions are similarly anticipated to be noisy. Since the other systems studied here have larger Kn than this particular case, the noises in those cases are expected to be worse, because the dynamics are faster, and we need to resolve the forces over a much shorter period of time. Consequently, direct force evaluations from MD cannot be relied on, while determining work done against drag. A way around this problem is to execute many realisations of any particular case considered here and obtain an ensemble average of these forces and centre-of-mass displacements. Limited by the computational resources available, this is not a practical solution to this problem. Furthermore, even if successful, this method will only be able to validate the droplet jumping speeds observed

at a few values of Knudsen numbers. Consequently, a curve fitting will have to be done in any case in order to obtain a continuous function depicting the droplet jumping speeds for a range of Kn that is of engineering relevance.

Another way of estimating W_{drag} during coalescence is by explicitly determining the total stress causing drag over the entire surface and summing the work done against it over the time scale of coalescence. However, evaluating local stress tensors on the droplet surface in nanoscale systems is highly challenging because (a) thermal fluctuations are strong, (b) there can be slip and Knudsen layers near the interfaces and (c) the process happens very rapidly. In what follows, a crude estimate of W_{drag} is attempted, which captures some of the underlying physics.

For a small, rigid and spherical particle of radius a (representing the droplet), moving through a highly viscous (μ_g) and infinitely large medium with a relative speed v at low particle Reynolds number, the Stokes drag on it is given by

$$F_{Stokes} = 6\pi\mu_g a v, \tag{5.7}$$

which is accurate only when the Knudsen number (based on particle radius) is small. In the coalescence-induced jumping problem, the drag will be different from the above expression due to three reasons: (a) because of the rarefaction in the surrounding gas resulting in finite non-zero particle Kn, (b) due to the influence of the wall under both droplets making the medium not infinitely large and (c) due to the complex flow geometry during the coalescence process. In what follows, each of these problems is separately analysed in detail and the significance of 'reduction factors' in modifying Stokes drag relevant to engineering applications is demonstrated.

(a) *Modification due to finite non-zero* Kn— In this case, the slip between the particle surface and the ambient medium must be accounted for while evaluating the drag force. There have been many attempts to incorporate slip at interfaces into the Stokes-flow analysis and one of the most successful ones for determining the drag force on small spheres moving through a gas, without any restrictions on Kn, is by Warren F. Phillips (Phillips, 1975). His approximate theoretical expression gives

$$F_{drag} = F_{Stokes} q(\text{Kn}) = 6\pi\mu_g a v \left(1 - \frac{15\text{Kn} - 15.42\text{Kn}^2 + 54\text{Kn}^3}{15 + 12\text{Kn} + 18\text{Kn}^2 + 54\text{Kn}^3}\right), \tag{5.8}$$

where q is a reduction factor incorporating the effects of gas rarefaction on a moving spherical particle in an infinite medium. Figure 5.5(b) shows how the drag force on a small sphere gets modified for a wide range of Kn (Phillips, 1975). Complete accommodation between water droplets and nitrogen molecules is assumed here. The above equation is derived by assuming that the mean speed is much less than the thermal speed of particles in the surrounding medium, which is the case when the final droplet jumps off the superlyophobic surface.

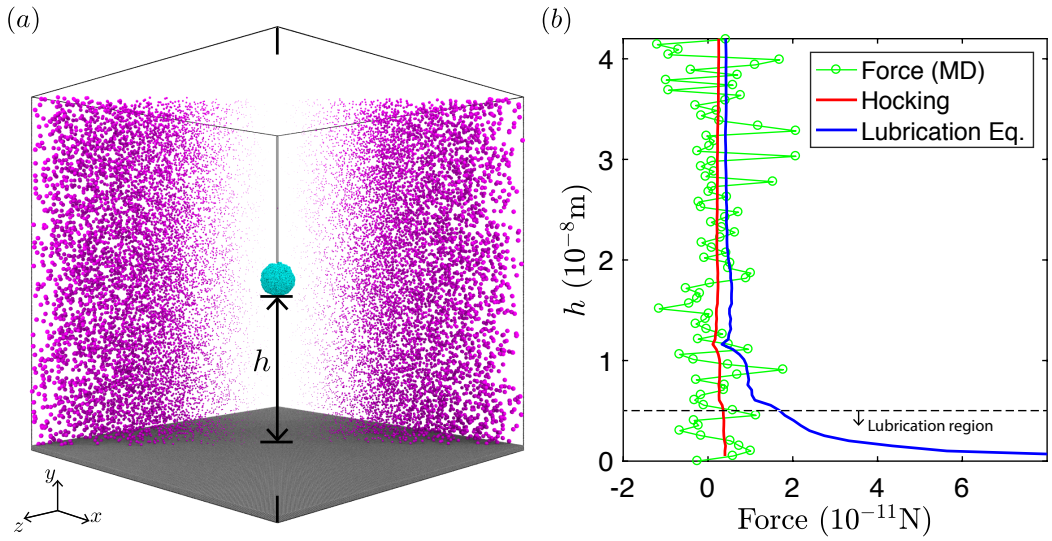

Figure 5.7: (a) Slice of the MD domain used in this section to study drag on a spherical nanodroplet approaching a wall (water droplet of $R = 5.1$ nm in nitrogen atmosphere at Kn = 3.7). (b) Comparison of drag obtained from MD simulations with Hocking drag and drag derived from lubrication approximation. Force is calculated using the instantaneous speed of the sphere at each vertical location. While the latter diverges for the droplet near the wall, Hocking's expression seems to better capture the physics even for such nanoscale systems.

(b) *Modification due to the presence of wall (sphere approaching a wall)*— When a particle approaches a wall, the traditional lubrication approximation predicts that the opposing force is inversely proportional to the gap (h) between the particle and the wall, i.e.

$$F_{Lubrication} = F_{Stokes}\phi_L = 6\pi\mu_g a v\left(\frac{a}{h}\right), \tag{5.9}$$

for large values of ϕ_L. This would mean that a contact is impossible in finite time.

Hocking (Hocking, 1973) used Maxwell's slip boundary condition to quantify the resisting force between approaching surfaces and found that the force depended only logarithmically on the gap width between the surfaces, in which case a contact can be achieved in finite time:

$$F_{Hocking} = F_{Stokes}\phi_H = 6\pi\mu_g a v\left(\frac{2a}{h\eta^2}[(1+\eta)\log(1+\eta)-\eta]\right);\ \eta \equiv 6\lambda/h. \tag{5.10}$$

A separate set of MD simulations are performed in order to compare the force experienced by a droplet moving towards a wall with that predicted by the Hocking and lubrication expressions for the resisting force. Figure 5.7(a) shows the MD geometry used for this separate analysis and in Figure 5.7(b), the actual force is compared with Eqs. (5.9) and (5.10). The system consists of a water droplet of $R = 5.1$ nm placed in a nitrogen atmosphere at $p_\infty = 3.75$ atm at $T = 300$ K. The system is equilibrated for a long time (~ 5 ns) and an impact speed of 20 m/s (of the

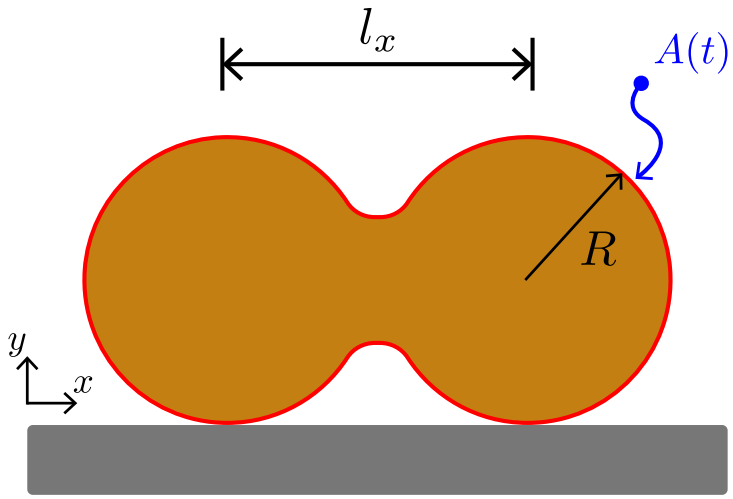

Figure 5.8: Schematic of droplet coalescence for determining the work done against drag.

order of maximum jumping speed observed in the MD simulations) is given to the droplet in the direction towards the wall; the droplet starts from a height of 50 nm above the wall. For the droplet near the wall, the force on it in a direction normal to the wall due to all surrounding gas molecules as a function of the gap width h is explicitly measured. While the traditional analysis based on lubrication approximation wildly over-predicts the opposing force in the lubrication region ($h < 5$ nm), the reduction factor ϕ_H enables Hocking's expression to follow the variation of the force measured for nanoscale droplets in MD.

The above two expressions are derived for a simpler flow geometry than what we have when two droplets coalesce and jump. Consequently, it may not be appropriate to use any of them, even Hocking's expression, in determining the effect of wall on the drag on the droplets as they merge. Nevertheless, the discussion presented in this section demonstrates that depending on the problem at hand, some reduction factor (ϕ or q) modifies the Stokes expression for drag on a spherical particle to account for slip at interfaces caused by kinetic gas effects; an exact theoretical expression without experimental fitting is not always available, even for some simple systems.

(c) *Modification due to complex flow geometry*— In order to evaluate the total work done against drag during the coalescence process, the drag is decomposed into two components: the first being the drag on the droplets because of their motion towards each other in the direction parallel to the underlying wall as they coalesce ($W_{\parallel}$) and the second is due to their combined motion in the direction normal to the wall ($W_{\perp}$). Next, some assumptions about how to model these two phases of the process are made in a manner that captures the main physics but remains as simple as possible to work its way into an analytical equation.

For evaluating $W_{\parallel}$, the droplets' instantaneous total surface area $A(t)$ is equated to that of two

full spheres moving in an ambient medium of viscosity μ_g, each with a speed relative to the ambient medium given by half the instantaneous speed of approach of the droplets: $V_x(t) = dl_x/dt$ (see Figure 5.8). In moving both droplets towards each other by a distance dx parallel to the wall, the infinitesimal amount of work done against the drag will be:

$$dW_{\parallel} = 2\left(6\pi\mu_g a(t)\frac{V_x(t)}{2}q(\mathrm{Kn})\right)\frac{dx}{2}, \tag{5.11}$$

where $a(t) = \sqrt{A(t)/8\pi}$ is the radius of two full spheres as described above. Here, Eq. (5.8) is used, since the coalescence happens in a finite non-zero Kn atmosphere.

Similarly, in order to evaluate $W_{\perp}$, the instantaneous total surface area is equated to a single sphere of the same area moving normal to the wall with a speed given by the instantaneous speed of coalescing droplets in the same direction, which gives

$$dW_{\perp} = \left(6\pi\mu_g\sqrt{2}a(t)|V_y(t)|q(\mathrm{Kn})\right)|dy|. \tag{5.12}$$

Therefore, the total work done against drag during coalescence (W_{drag}) can be obtained by summing all the infinitesimal amounts of both contributions from the beginning of coalescence until it ends, multiplied by an unknown reduction factor ψ that is introduced here in order to accommodate the effects of a complex deforming liquid body and any possible influence of the underlying wall on drag that is not considered in this simplified analysis. Obtaining an analytical expression for ψ will be difficult and so, it will determined by curve fitting.

In Figure 5.9, the time evolution of the scaled total surface area and the approach speed are shown for $R = 5.1$ nm droplets for two different Knudsen numbers. $\mathrm{Kn} \to \infty$ denotes simulations in near-vacuum. The dynamics is nearly unaffected by the presence of an ambient gaseous medium (also seen in Fig. 5.5) and the coalescence process at such high Oh_l is 'smooth', as there are no obvious oscillations in any of the measured quantities or in the droplet geometry. In the figure, $A(t)$ is determined in MD simulations using a method described in Chapter 1.

Figure 5.10 shows how the centre-of-mass speed in the direction normal to the wall changes due to rarefaction as coalescence proceeds for $R = 7.2$ nm droplets for two different Knudsen numbers. The major change in the dynamics occurs only towards the end of the simulation, where droplets have already merged and the final droplet is about to lift-off from the surface. In all cases, the drag is evaluated by using $V_y(t)$ corresponding to the vacuum case. This will make all parameters used to evaluate drag identical among all cases of Kn for any particular size (or Oh_l), except ψ. Hence, there is only one fitting parameter in the entire analysis: ψ.

Equating Eq. (5.4) to Eq. (5.6) by setting $\Delta T_g \approx \Delta T_v$, the energy balance will then reduce to

$$m_d V_g^2 = m_d V_v^2 - W_{\mathrm{drag}}. \tag{5.13}$$

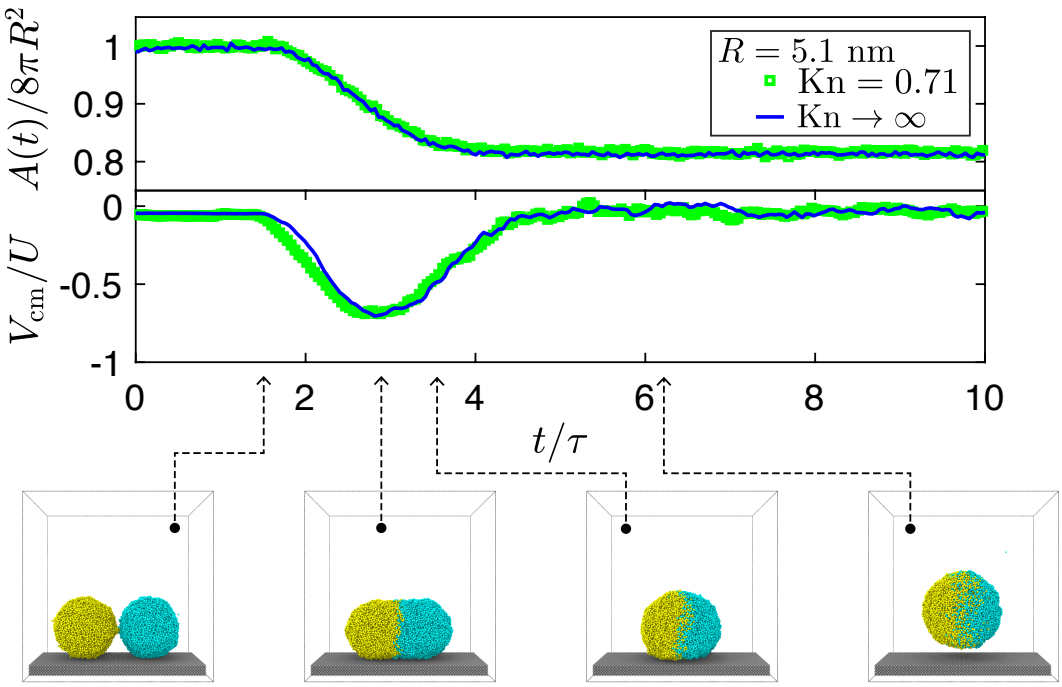

Figure 5.9: The time evolution of scaled total surface area and approach speed of the droplets during coalescence of two $R = 5.1$ nm ($\mathrm{Oh}_l = 0.55$) droplets. The invariace of both $A(t)$ and $V_{\rm cm}$ with respect to Kn shows that the geometry of the coalescing droplets is independent of Kn. This further implies that $W_{\rm adh}$ is independent of outer conditions.

Dividing both sides by $m_d U^2$ and subsequent modification gives,

$$V_g^* = \sqrt{V_v^{*2} - \frac{W_{\rm drag}}{m_d U^2}} = \sqrt{V_v^{*2} - \frac{\psi \sum (dW_\perp + dW_\parallel)}{m_d U^2}}. \tag{5.14}$$

In the above equation, the summation is performed over the timescale of coalescence. It must be noted that although the above equation provides reasonable insights about the process, it requires the knowledge of V_v^* to obtain V_g^*. The average values of vacuum-limit MD data are used to estimate V_v^*, since thermal fluctuations are important at this scale (see below).

In Fig. 5.11, the scaled jumping speed as a function of Kn obtained from MD simulations is shown for two systems: $R = 7.2$ nm ($\mathrm{Oh}_l = 0.45$) and $R = 5.1$ nm ($\mathrm{Oh}_l = 0.55$). For both cases, the data is fitted to Eq. (5.14) with only ψ as the fitting parameter. There is characteristic change in the jumping speed at $\mathrm{Kn} = 1$, which is also indicative of the crucial role played by the ambient rarefied gas in the overall dynamics. In Fig. 5.11(a), an extrapolation of the fit to our Eq. (5.14) predicts non-zero jumping speed for a wider range of Kn (down to $\mathrm{Kn} = 0.035$) as compared to Fig. 5.11(b). At 300 K, nitrogen approaches super-critical behaviour near 30 atm, and this restricts us from simulating lower Kn. For both cases, the value of ψ which maximised the coefficient of determination of the fit is chosen to plot the red lines in Fig. 5.11.

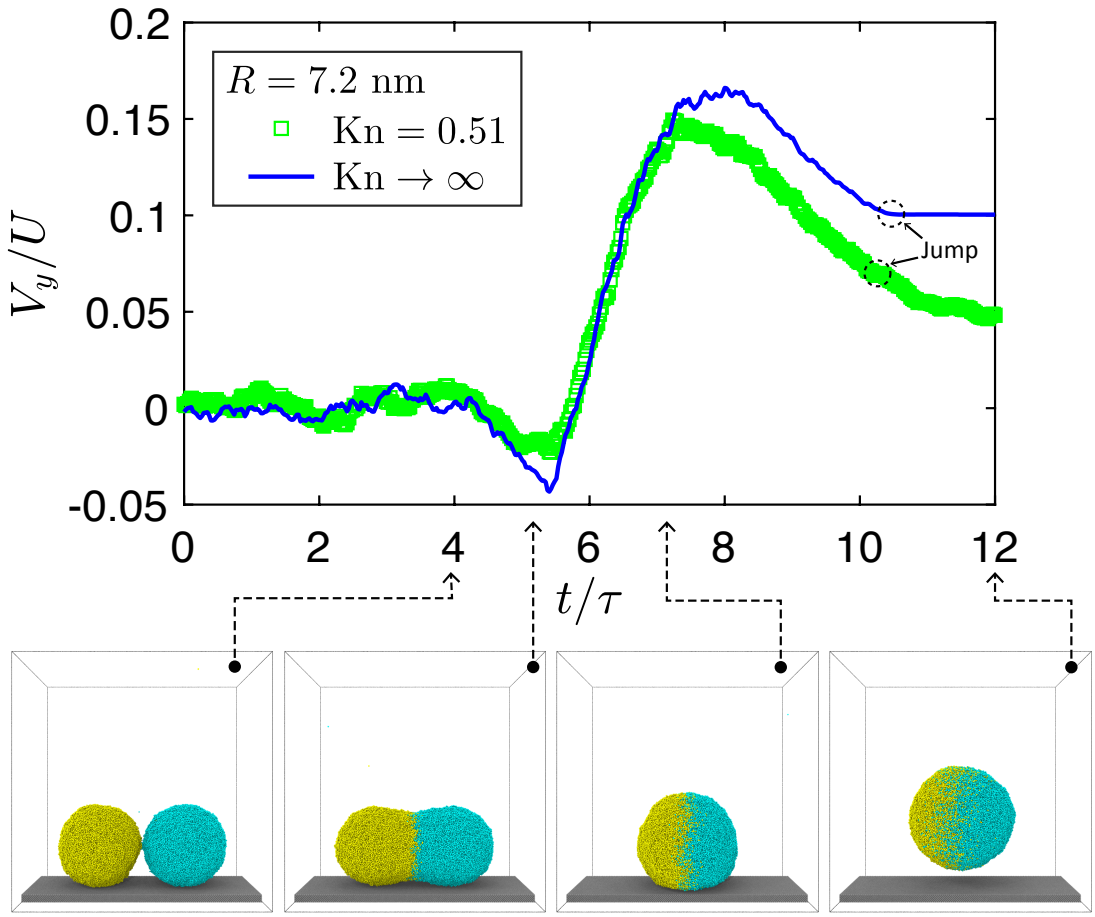

Figure 5.10: Time evolution of centre-of-mass speed of the droplets ($R = 7.2$ nm; $\mathrm{Oh}_l = 0.45$) in the direction normal to the wall. Presence of an outer fluid changes the behaviour of V_y only towards the end of the process. Simulation snapshots show only the coalescence in vacuum (Kn $\to \infty$).

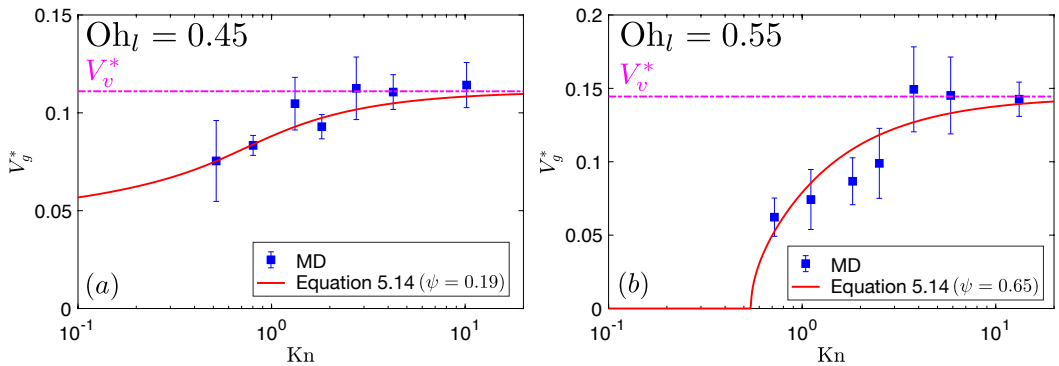

Figure 5.11: V_g^* as a function of ambient gas Kn for (b) $\mathrm{Oh}_l = 0.45$ and (c) $\mathrm{Oh}_l = 0.55$. At large Kn, the jumping speed increases and approaches its vacuum limit. The decrease in V_g^* at low Kn is due to the increase in drag from the surrounding gas.

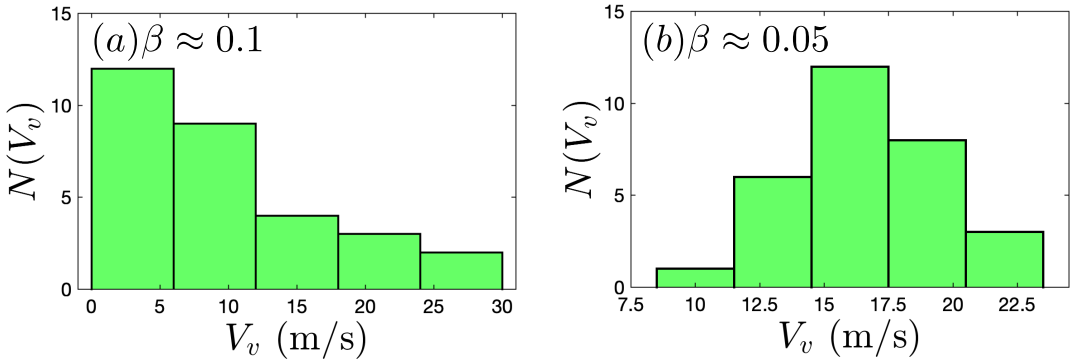

Figure 5.12: Distribution of coalescence-induced jumping speeds in vacuum for (a) $R = 3.1$ nm and (b) $R = 5.1$ nm droplets, showing how the contribution of thermal motion of the liquid molecules to the jumping speed differs with the thermal fluctuation number β. For droplets with larger β, the pronounced influence of thermal fluctuations renders the distribution to be significantly skewed and wider.

5.4 Stochastic nature of jumping speed

An interesting observation from these simulations is that just like the droplet coalescence in Chapter 3, and the droplet spreading in Chapter 4, thermal-capillary waves play a role here as well. Similar but independent realisations of the same two droplets are observed to jump with various jumping speeds, suggesting that a unique value for jumping speed is not possible for nanodroplets. In stark contrast to the traditional notion, where similar initial conditions for a particular droplet size predict a similar value for jumping speed, the presence of thermal motion of liquid molecules brings in a statistical nature to the jumping speed.

For nanodroplets, a *thermal-fluctuation number* is proposed as being the ratio of amplitude of interfacial thermal fluctuations to the droplet radius: $\beta \equiv \sqrt{k_B T/\gamma R^2}$. For a given liquid-vapour interface, β will be larger for smaller droplets. This means that the effect of thermal-capillary waves on the jumping dynamics will be more on droplets with a larger value of β. Figs. 5.12(a) and 5.12(b) show the distribution of coalescence-induced jumping speeds in vacuum for two droplets with $R = 3.1$ nm ($\beta \approx 0.1$) and $R = 5.1$ nm ($\beta \approx 0.05$) respectively. The distributions are obtained by performing 30 MD realisations, each of independent initial conditions. For a droplet with larger value of β, the influence of thermal-capillary waves makes the jumping speed distribution to be significantly wide. The skewness of the distribution in Fig. 5.12(a) is explained below.

A single nanodroplet naturally bounces up and down on a superlyophobic surface, due to thermal fluctuations of the constituent molecules (see Fig. 5.13). This effect is more predominant for smaller droplets, as the amplitude of surface fluctuations are $\sim$ 1 nm. When two such droplets approach each other, their centres-of-mass can be at different heights, as seen in Figs. 5.14(a), 5.14(b) and corresponding simulation snapshots. In Case A, by the time the bridge hits

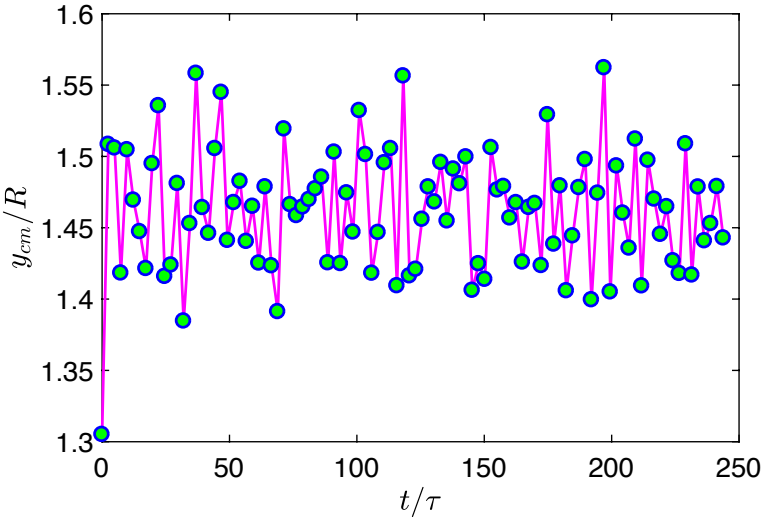

Figure 5.13: The y coordinate of centre-of-mass of a $R = 3.1$ nm nanodroplet on a superlyophobic surface. Here, $\tau = \tau_i$ is the inertial-capillary time scale and R is estimated from the equimolar line from a time-averaged density profile of a droplet. The value of $y_{cm}/R > 1$ is due to the finite thickness of the water-vapour interface and the way R is defined. Oscillations in y_{cm}/R is caused by thermal fluctuations.

the surface, one of the droplets (yellow) has its centre-of-mass above the other droplet. Such an asymmetry in the coalescence will always slow down the jumping process as it is this impact of the bridge normal to the surface that provides the reaction force necessary for the final droplet to jump. Conversely in Case B, the centres-of-mass align and the impact of the bridge is normal to the wall such that the final droplet is able to lift off from the surface. Since in most of the times, the bouncing of the droplets will make the coalescence proceed asymmetrically (similar to Case A), the skewness of the distribution shown in Fig. 5.12(a) is expected. Such significant skewness is not observed for larger droplets, where β is relatively smaller (Fig. 5.12(b)), suggesting the diminishing significance of interfacial thermal fluctuations on the jumping of large droplets. As shown in Figs. 5.14(a) and 5.14(b), the jumping speed in two realisations of the same system of two nanodroplets can differ by as much as 27 m/s. The energy which could have been used for jumping in Case A is converted into viscous dissipation, but this is hard to distinguish in a temperature-time profile, because of the large value of c_p of water model used.

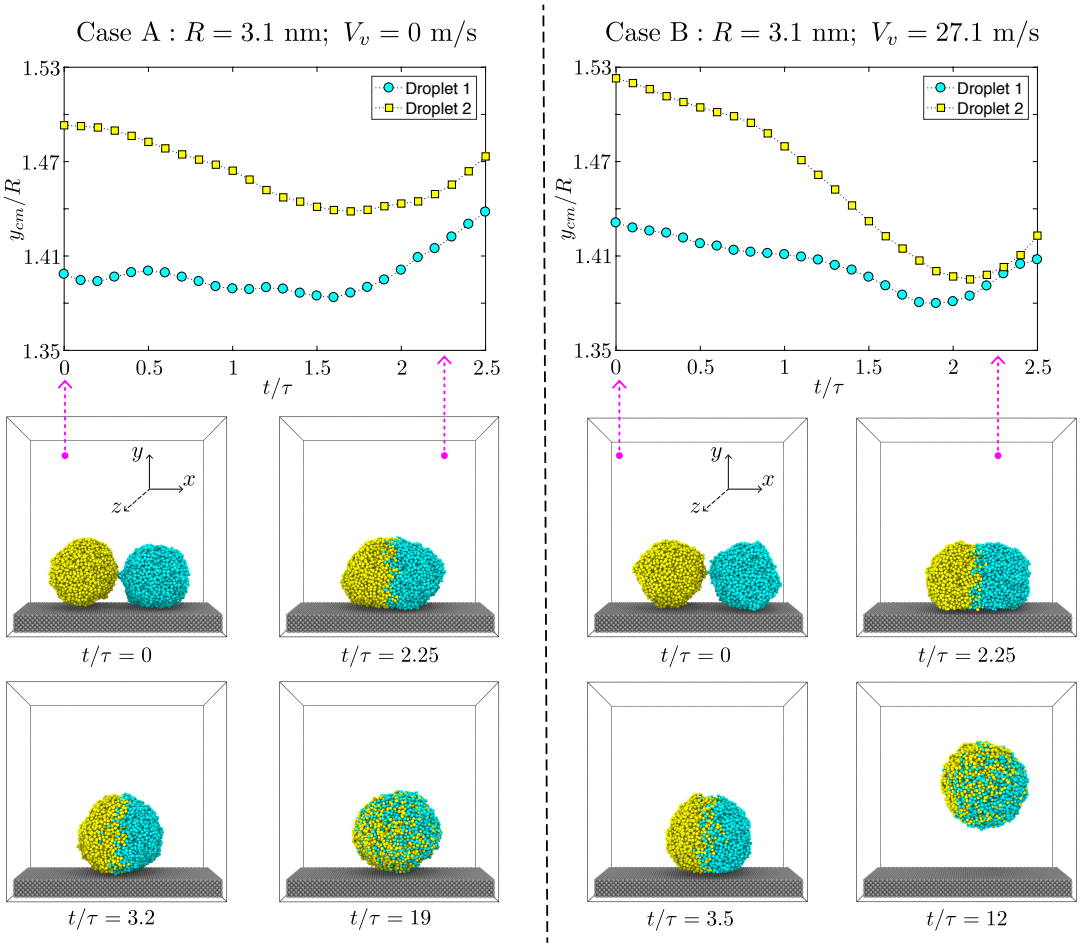

Figure 5.14: Position of y coordinate (normal to the wall) of the centre-of-mass of each droplet on the superlyophobic surface right after they establish the first contact until the bridge hits the underlying surface. Corresponding simulation snapshots show (a) $V_v = 0$ m/s when the bridge grows in a direction widely different from y, and (b) V_v is non-zero when the bridge grows in the direction normal to the wall. Here, $\tau = \tau_i$ is the inertial-capillary time scale.

5.5 Discussion and outlook

These results show that the process governing nanodroplet jumping is defined not just by Oh_l (which quantifies the viscous dissipation within the droplet) but also by two other dimensionless numbers that represent the non-continuum molecular physics: Kn and β. Kn has an effect on reducing the drag due to the rarefied atmosphere, while β depends only on droplet size and can exist at any Kn; its influence is on making the jumping speed have a wide statistical spread.

In Figure 5.15, V_g^* as a function of Oh_l is compared between MD and VoF simulations. For $\mathrm{Oh}_l > 0.1$, which is of interest to nanodroplets technologies, continuum VoF simulations predict a monotonic decrease of V_g^*. A part of this is verified in recent experiments (Enright *et al.*, 2014), and a cut-off Ohnesorge number (Oh_{lc}) is identified that depends on the viscosity ratio between the two phases (μ_g/μ_l; see inset of Figure 5.15). Here, Oh_{lc} is defined as the minimum

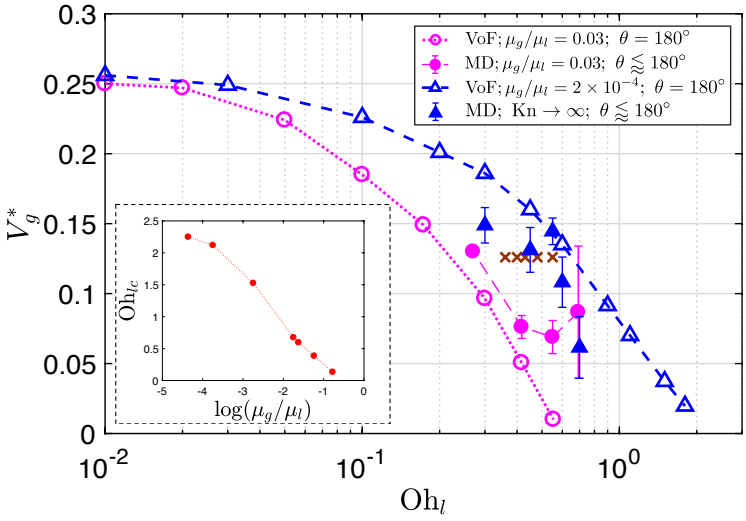

Figure 5.15: Scaled jumping speed (V_g^*) as a function of Oh_l comparing different computational methods. Brown '$\times$' symbols represent results from Liang and Keblinski (2015). For systems where the dynamics is predominantly controlled by liquid properties, the scaled jumping speed decreases monotonically with Oh_l due to increased viscous dissipation. This is exhibited by both MD in vacuum ($\mathrm{Kn} \to \infty$) and VoF simulations with small μ_g/μ_l. For *large enough* droplets coalescing in an outer fluid, MD and corresponding VoF predictions agree well ($\mu_g/\mu_l = 0.03$ case). Deviations are observed as the size is decreased (Oh_l increased), due to nanoscale effects, which are not incorporated in continuum simulations. Inset shows Oh_{lc} appears to saturate to a maximum value of 2.5 as $\mu_g/\mu_l \to 0$.

Oh_l at which the VoF simulations predict no jumping occurs. If thermal fluctuations were absent, MD simulations with $\mathrm{Kn} \to \infty$ are considered equivalent to VoF simulations in the limit $\mu_g/\mu_l \to 0$. In such cases, where the dynamics is governed by the coalescing liquid, the decrease of V_v^* with Oh_l is in accordance with the traditional understanding.

In the presence of an outer fluid, the final droplet jumps at a lower speed compared to its vacuum limit, which happens because of an additional dissipation mechanism present in the system, to the internal viscous losses. In such cases, the scaled jumping speed decreases monotonically with decreasing Kn, which is quantified by Eq. (5.14). The results presented here and that of Liang and Keblinski (2015) show a clear deviation from the predictions of VoF simulations with identical viscosity ratio as Oh_l is increased. In their work, Liang and Keblinski hinted at the possible influence of fluid slip effects on the jumping speed, but did not quantify it. Based on the results presented earlier, it can be inferred that V_g^* is larger than expected because the drag on the droplets is not as severe as what is predicted by VoF simulations, which do not account for slip at various interfaces and other rarefaction effects. This reduction in drag is relatively higher for smaller droplets as their Kn is larger by definition, while keeping λ constant (coalescence of argon droplets in vapour at a certain condition, for example). As shown in Fig. 5.5(a), the difference in data between Liang and Keblinski (2015) and the results in Figure 5.15, is mainly

due to the higher adhesion between the surface and droplets.

Besides the effect of ambient gas, the influence of interfacial thermal fluctuations is also overlooked in the literature, even in molecular simulations of nanodroplets (Gao *et al.*, 2018; Sheng *et al.*, 2017) where, as revealed here, its impact is non-negligible. For instance, the extreme normalised jumping speed shown in Figure 5.14 correspond to $V_v^* \approx 0.2$, which is nearly as high as its maximum limit that is only expected for microscale droplets (Mouterde *et al.*, 2017; Enright *et al.*, 2014) (i.e. where Oh_l is small and there are negligible gravitational effects). These MD simulations reveal the importance of thermal fluctuations on nanodroplet jumping, i.e. such behaviour of nanodroplets is only stochastic.

Although MD simulations capture the full picture of droplet coalescence, its extreme computational expense puts a cap on the maximum droplet size that can be simulated. A generalized continuum framework incorporating slip at various interfaces and thermal fluctuations can be expected to reproduce the MD results and modelling droplet jumping using such a method seems like a promising way forward.

Chapter 6

Conclusions and outlook

This thesis investigated the effects of interfacial thermal fluctuations and intermolecular interactions on the dynamics of coalescing, spreading and jumping nanodroplets. The manifestation of these nanoscale molecular effects at a larger scale is uncovered for the first time using unconventionally-large and computationally-expensive molecular dynamics (MD) simulations, their impact quantified using collective statistics of engaging molecules, and their characteristics explained using predictive theoretical analyses. The influence of other non-continuum effects such as extreme gas rarefaction and atomic structure of boundary walls are also studied in the process. Such processes that involve droplet-droplet and droplet-surface interactions find numerous fascinating applications in nature (Wisdom *et al.*, 2013; Agasthya *et al.*, 2019), engineering (Miljkovic *et al.*, 2013), medical sciences (Komatsu *et al.*, 1997) and in our daily lives (Kumar *et al.*, 1996).

The primary outcome of this study and a foundational theme in each of the three main chapters (3 – 5) is that it reveals the radical significance of interfacial thermal fluctuations in the beginning of droplet coalescence and spreading, which are assumed insignificant in previous work. The traditional mathematical models host a singularity in the beginning of these processes, where measurable quantities like local velocity and stress diverge. Such unphysical features arise due to the continuum assumption that is the foundation of these models. Through MD simulations, it is shown that the interfacial thermal fluctuations, assisted by intermolecular interactions, reach across the intervening gap between droplets (in case of coalescence), and droplet/substrate (in case of spreading) to form and develop a capillary bridge in the initial stages of the processes. This manner of capillary bridge evolution continues until the bridge radius reaches a size dependent thermal length scale ($l_T \sim \sqrt{R}$). Interestingly, the high-aspect ratio geometry in the initial stages between a droplet and another droplet (or a substrate) enables such nanoscale molecular effects to be manifested at even micrometre length scales. The study also points to a possibility that the 'thermal regime' of droplet coalescence and 'thermal-vdW regime' of droplet spreading are just two special cases of a general interface evolution mechanism relevant to many natural and industrial applications, which have so far avoided rigorous analysis due to the presence of a singularity in their mathematical formulations. Furthermore, the rarefaction in the surrounding gas medium is found to have only a minimal effect on the growth of the capillary bridge in the initial dynamics.

On superlyophobic surfaces, interfacial thermal fluctuations have an added effect on nanodroplet jumping dynamics, i.e. to render the jumping speed to be statistically distributed; traditional theories predict the jumping speed as a single-valued function of droplet size. The effect is more drastic as the size of coalescing droplets is decreased, where the jumping speed distribution becomes increasingly skewed and wider; meaning there is no unique jumping speed. The lift off of these droplets can happen anywhere between both extremes: they can jump with very high or moderate speeds, or do not jump at all. During coalescence-induced jumping of nanodroplets, the outer gas rarefaction has an influence on the dynamics. Drag increases as surrounding gas pressure increases, but not as much as one expects from standard continuum theory. In fact, the drag on nanodroplets is lower than expected because of rarefaction effects, which enables the nanodroplets to jump.

In summary, this thesis has shined a light on the importance of the molecular physics when considering multiphase/multiscale problems that employ droplets. In particular, interfacial thermal fluctuations or thermal capillary waves, intermolecular interactions and non-equilibrium gas effects play a significant role in the coalescence, wetting and coalescence induced jumping of nanodroplets, i.e. when the dominant length scale of the system being studied becomes comparable to the thermal fluctuation amplitude $\sqrt{k_B T/\gamma}$.

6.1 Future work

From a modelling perspective, performing molecular simulations are computationally expensive as it models every single molecule in a system. This correspondingly puts a cap on the largest length scale ($\sim$ 100 nm) and the longest time scale ($\sim$ 100 ns) that can be achieved in MD simulations. Even though the power of computers are increasing every year, it may not be a viable option to keep resorting to MD simulations. A better alternative is to incorporate the molecular effects such as interfacial thermal fluctuations and intermolecular interactions into continuum approaches. While these have been introduced into continuum frameworks separately (Zhao *et al.*, 2019a; Zhang *et al.*, 2019; Prevost and Gallez, 1986; Vrij and Overbeek, 1968; Vrij, 1966), a complete continuum picture simultaneously addressing both effects is lacking in the literature. Perhaps the best candidate available in the literature of continuum frameworks for incorporating these nanoscale effects may be the interface formation/disappearance model of droplet spreading/coalescence (Shikhmurzaev, 1993, 1997; Sprittles and Shikhmurzaev, 2012, 2014a), as it has some similarity with what is observed in the initial stages of these processes in MD simulations. A multiscale simulation technique of droplet coalescence, like what has been already developed for droplet spreading problem (Zhang *et al.*, 2017), is also worth looking into, as it can simulate coalescence of much larger droplets incorporating the nanoscale effects.

From an experimental point of view, attempts to observe the nanoscale effects uncovered in the

present thesis can shed light on previously unexplored realms of nanoscale interfacial fluid flow. This can be challenging as the length scales associated with these processes for pure liquids are $\sim 1-10$ nm, and the smallest length scale that is accessed in experiments related to interfacial thermal fluctuations and coalescence are $\sim 1\mu$m (Paulsen *et al.*, 2012; Aarts *et al.*, 2004). Particularly in Aarts *et al.* (2004), where they experimentally observed interfacial thermal fluctuations, an ultra-low surface tension mixture was used. As discussed in Chapter 1, lower γ will result in simultaneous enhancement of the associated length scales and slowing down of the dynamics. Perhaps, the adhesion of confronting interfaces during the growth of the bridge in the initial stages of droplet coalescence/spreading that removes a mathematical singularity can be observed in theory-driven experiments that use these unique fluids. These type of experiments can also help develop novel engineering surfaces with maximum throughput (e.g. in surface coating technologies) and introduce unconventional techniques to find solutions to many problems in industry (e.g. coalescence-induced jumping of nanodroplets has the potential to selectively self-clean engineering surfaces or form part of a thermodynamic cycle in next generation microprocessor cooling membranes).

Singularities in fluid mechanics are not uncommon. They are broadly classified into mathematical and physical singularities (Moffatt, 2019). Common examples include flow around sharp corners joining solid and porous walls (Nitsche and Bernal, 2018), cusp singularity at fluid/fluid interface (Jeong and Moffatt, 1992), tip singularity during freezing of water droplets placed on a supercooled surface (Marin *et al.*, 2014; Enriquez *et al.*, 2012) and diverging evaporation rate (the so-called d^2 law) of free droplets, where d is their diameter. Some of these problems have been resolved by accounting for various nanoscale phenomena in their numerical analyses – for example, the singularity in droplet evaporation has been resolved recently by incorporating a temperature-jump boundary condition derived from kinetic theory of gas and compared to MD simulations (Rana *et al.*, 2019). Many similar problems await solution in the scientific literature. Resolving some of these problems using MD may provide us with a better picture of the wide class of interface evolution phenomena that forms the basis of many natural multiscale processes and engineering applications.

Appendix A

Thermal fluctuations on a thin cylindrical liquid surface

The following derivation is due to Dr. Mykyta V. Chubynsky.[1] In this Appendix, we derive the mean-square displacement of the surface of a short cylinder due to thermal fluctuations. This result is needed to obtain the value of the cut-off length B_0 from MD simulations, and is also used to derive the width of the distribution of coalescence onset locations.

Consider an incompressible liquid cylinder of radius R. Periodic boundary conditions with period L are assumed along the axis of the cylinder. Our consideration of thermal fluctuations of its surface uses an approach similar to that of Sides *et al.* (1999) for a planar surface, where the fluctuations are expanded in eigenmodes and the equipartition theorem is utilized. However, there are two important differences. First, while in Sides *et al.* (1999) the sum over the modes is replaced with an integral, which is valid for a surface with similar dimensions in the two directions, we retain the sum and analyze carefully under what conditions the replacement is possible. Second, in the case of a curved surface, special care needs to be taken to ensure that the eigenmodes preserve the volume.

In cylindrical coordinates, the shape of the surface of the cylinder is described by a function $r(z,\phi,t)$, where z is the coordinate along the axis ($0 \le z \le L$), ϕ is the azimuthal angle ($0 \le \phi \le 2\pi$), r is the radial distance of the surface from the axis, and t is the time. The surface area of the periodically repeated section of the cylinder is

$$A(t) = \int_0^L dz \int_0^{2\pi} d\phi \left(r^2 \left[1 + \left(\frac{\partial r}{\partial z} \right)^2 \right] + \left(\frac{\partial r}{\partial \phi} \right)^2 \right)^{1/2}, \tag{A.1}$$

and the volume is

$$V(t) = \frac{1}{2} \int_0^L dz \int_0^{2\pi} d\phi \, r^2. \tag{A.2}$$

We express the radial distance as

$$r(z,\phi,t) = R + \zeta(z,\phi,t), \tag{A.3}$$

1. Research Associate, University of Warwick

and assume that the deviation ζ from the cylindrical shape is small ($\zeta \ll R$).

In the linear approximation, free oscillations of the cylinder can be expanded into eigenmodes:

$$\begin{aligned}\zeta(z,\phi,t) \approx & \sum_{n_z=1}^{\infty}\sum_{n_\phi=1}^{\infty}\zeta^{(1)}_{n_z n_\phi} + \sum_{n_z=1}^{\infty}\sum_{n_\phi=0}^{\infty}\zeta^{(2)}_{n_z n_\phi} \\ & + \sum_{n_z=0}^{\infty}\sum_{n_\phi=1}^{\infty}\zeta^{(3)}_{n_z n_\phi} + \sum_{n_z=0}^{\infty}\sum_{n_\phi=0}^{\infty}{}'\zeta^{(4)}_{n_z n_\phi},\end{aligned} \tag{A.4}$$

where

$$\zeta^{(1)}_{n_z n_\phi}(z,\phi,t) = a^{(1)}_{n_z n_\phi}\sin\frac{2\pi n_z z}{L}\sin n_\phi\phi, \tag{A.5}$$

$$\zeta^{(2)}_{n_z n_\phi}(z,\phi,t) = a^{(2)}_{n_z n_\phi}\sin\frac{2\pi n_z z}{L}\cos n_\phi\phi, \tag{A.6}$$

$$\zeta^{(3)}_{n_z n_\phi}(z,\phi,t) = a^{(3)}_{n_z n_\phi}\cos\frac{2\pi n_z z}{L}\sin n_\phi\phi, \tag{A.7}$$

$$\zeta^{(4)}_{n_z n_\phi}(z,\phi,t) = a^{(4)}_{n_z n_\phi}\cos\frac{2\pi n_z z}{L}\cos n_\phi\phi, \tag{A.8}$$

the coefficients $a^{(j)}_{n_z n_\phi}$ are time-dependent, and the prime in the last sum excludes the term with $n_z = n_\phi = 0$ as it corresponds to the uniform expansion or contraction of the cylinder and so does not preserve the volume.

When thermal fluctuations are considered, the coefficients a vary randomly in time and are uncorrelated, so

$$\langle a^{(i)}_{m_z m_\phi} a^{(j)}_{n_z n_\phi}\rangle \sim \delta_{m_z n_z}\delta_{m_\phi n_\phi}\delta_{ij}, \tag{A.9}$$

where $\langle\ldots\rangle$ denotes the time average and δ_{kl} is the Kronecker delta. However, it is important to note that perturbations of the form in Eqs. (A.5)–(A.8) do not preserve the volume exactly, with deviations quadratic in a. To ensure volume preservation, we replace Eq. (A.5) with

$$\begin{aligned}\zeta^{(1,2,3,4)}_{n_z n_\phi}(z,\phi,t) = & \; a^{(1,2,3,4)}_{n_z n_\phi}\sin\frac{2\pi n_z z}{L}\sin n_\phi\phi \\ & -\Delta_{n_z n_\phi}(a^{(1,2,3,4)}_{n_z n_\phi}),\end{aligned} \tag{A.10}$$

and similarly for Eqs. (A.6)–(A.8), where the Δ terms do not depend on z or ϕ and so correspond to uniform contraction (or expansion). By substituting these expressions into Eq. (A.3), expanding Eq. (A.2) to quadratic order in a and linear in Δ, and requiring that the volume remain equal to that of the unperturbed cylinder (i.e. $\pi R^2 L$), we obtain

$$\Delta_{n_z n_\phi}(a) = \begin{cases}\frac{a^2}{8R}, & n_z \neq 0 \text{ and } n_\phi \neq 0, \\ \frac{a^2}{4R}, & n_z = 0 \text{ or } n_\phi = 0.\end{cases} \tag{A.11}$$

While the Δ terms are quadratic in a and so at first sight seem negligible, this is not so, since

the area change is quadratic in a, but linear in Δ.

Combining Eqs. (A.3), (A.4), (A.10) and (A.11), we can find the area change due to surface fluctuations using Eq. (A.1), expanding it to quadratic order in a and subtracting the area of the unperturbed cylinder (i.e. $2\pi RL$). We find that the contributions of different modes to the area change are additive, and are given by

$$\Delta A^{(j)}_{n_z n_\phi} = \begin{cases} \left(\frac{\pi^3 R n_z^2}{L} + \frac{\pi L(n_\phi^2-1)}{4R}\right)\left(a^{(j)}_{n_z n_\phi}\right)^2, & n_z \neq 0,\ n_\phi \neq 0, \\ \frac{\pi L(n_\phi^2-1)}{2R}\left(a^{(j)}_{n_z n_\phi}\right)^2, & n_z = 0, \\ \left(\frac{2\pi^3 R n_z^2}{L} - \frac{\pi L}{2R}\right)\left(a^{(j)}_{n_z n_\phi}\right)^2, & n_\phi = 0. \end{cases} \tag{A.12}$$

Equation (A.12) has two notable features. First, $\Delta A^{(j)}_{01} = 0$. This is expected, since the corresponding modes (there are two of them, $\zeta^{(3)}_{01}$ and $\zeta^{(4)}_{01}$) are pure translations in the directions transverse to the axis of the cylinder and so do not deform it. These modes need to be subtracted when calculating the displacement of the surface, so the corresponding terms should be deleted from Eq. (A.4). Second, $\Delta A^{(j)}_{10} < 0$ when $L > 2\pi R$, so the corresponding deformation decreases the surface energy. This is, of course, the well-known Plateau-Rayleigh instability (Eggers and Villermaux, 2008). When it is present, the deviation from the cylindrical shape can become arbitrarily large; we restrict ourselves to the case when the instability does not arise (as is indeed true for our quasi-2D MD systems). It is worth noting that neither of these important features is reproduced when the Δ term in Eq. (A.10) is not included.

Surface energy changes associated with the modes can be obtained by multiplying Eq. (A.12) by the surface tension γ. By equipartition, these energy changes are, on average, $k_B T/2$, which gives

$$\left\langle \left(a^{(j)}_{n_z n_\phi}\right)^2 \right\rangle = \begin{cases} \frac{2k_B T/(\pi\gamma)}{\frac{L}{R}(n_\phi^2-1)+\frac{4\pi^2 R}{L}n_z^2}, & n_z \neq 0,\ n_\phi \neq 0, \\ \frac{k_B T/(\pi\gamma)}{\frac{L}{R}(n_\phi^2-1)}, & n_z = 0, \\ \frac{k_B T/(\pi\gamma)}{\frac{4\pi^2 R}{L}n_z^2-\frac{L}{R}}, & n_\phi = 0. \end{cases} \tag{A.13}$$

Then, according to Eq. (A.4) with the $n_z = 0$, $n_\phi = 1$ terms removed, taking into account Eq. (A.9) gives,

$$\begin{aligned} \langle \zeta^2 \rangle \;=\; & \sum_{n_z=1}^{N_z}\sum_{n_\phi=1}^{N_\phi} \frac{2k_B T/(\pi\gamma)}{\frac{L}{R}(n_\phi^2-1)+\frac{4\pi^2 R}{L}n_z^2} \\ & + \sum_{n_z=1}^{N_z} \frac{k_B T/(\pi\gamma)}{\frac{4\pi^2 R}{L}n_z^2 - \frac{L}{R}} + \sum_{n_\phi=2}^{N_\phi} \frac{k_B T/(\pi\gamma)}{\frac{L}{R}(n_\phi^2-1)}. \end{aligned} \tag{A.14}$$

The result is independent of z and ϕ, which is expected, since all points on the surface are equivalent. Note that the upper summation limits have been made finite by introducing cutoffs

N_z and N_ϕ. These cutoffs are important, because without at least one of them Eq. (A.14) would diverge. They are determined by the fact that below a certain length B_0, continuum fluid dynamics equations (on which the consideration here is based) cease to be valid. This length scale is typically comparable to the molecular size. The cutoffs then approximately correspond to the perturbations with wavelengths equal to this length scale, i.e.

$$N_z \approx \frac{L}{B_0}, \tag{A.15}$$

$$N_\phi \approx \frac{2\pi R}{B_0}. \tag{A.16}$$

Further progress can be made by assuming that the period in the axial direction L is much smaller than the radius R. We will also assume that B_0 is sufficiently small that $N_\phi \gg 1$. Then, since the last sum in Eq. (A.14) converges as $N_\phi \to \infty$, we can safely write

$$\sum_{n_\phi=2}^{N_\phi} \frac{k_B T/(\pi\gamma)}{\frac{L}{R}(n_\phi^2-1)} \approx \sum_{n_\phi=2}^{\infty} \frac{k_B T/(\pi\gamma)}{\frac{L}{R}(n_\phi^2-1)} = \frac{3k_B T R}{4\pi\gamma L}, \tag{A.17}$$

where the exact numerical value $\sum_{n=2}^{\infty} 1/(n^2-1) = 3/4$ has been used. The second sum

$$\begin{aligned} \sum_{n_z=1}^{N_z} \frac{k_B T/(\pi\gamma)}{\frac{4\pi^2 R}{L} n_z^2 - \frac{L}{R}} &\approx \frac{k_B T L}{4\pi^3 \gamma R} \sum_{n_z=1}^{N_z} \frac{1}{n_z^2} \\ &< \frac{k_B T L}{4\pi^3 \gamma R} \sum_{n_z=1}^{\infty} \frac{1}{n_z^2} = \frac{k_B T L}{24\pi\gamma R}, \end{aligned} \tag{A.18}$$

which is much smaller than Eq. (A.17) and therefore negligible. Finally, considering the double sum, since changing n_ϕ by one makes a change in the expression under the sum that is small compared to the expression itself, the sum over n_ϕ can be replaced by an integral:

$$\begin{aligned} &\sum_{n_z=1}^{N_z} \sum_{n_\phi=1}^{N_\phi} \frac{2k_B T/(\pi\gamma)}{\frac{L}{R}(n_\phi^2-1) + \frac{4\pi^2 R}{L} n_z^2} \\ &\qquad \approx \sum_{n_z=1}^{N_z} \int_{n_\phi=0}^{\infty} \frac{2k_B T/(\pi\gamma)}{\frac{L}{R} n_\phi^2 + \frac{4\pi^2 R}{L} n_z^2} dn_\phi \\ &\qquad = \frac{k_B T}{2\pi\gamma} \sum_{n_z=1}^{N_z} \frac{1}{n_z}. \end{aligned} \tag{A.19}$$

Then

$$\langle \zeta^2 \rangle \approx \frac{k_B T}{2\pi\gamma} \left[\frac{3R}{2L} + \sum_{n_z=1}^{N_z} \frac{1}{n_z} \right]. \tag{A.20}$$

The sum over n_z diverges in the limit $N_z \to \infty$, so N_z should be kept finite. If $N_z \gg 1$, then

$\sum_{n_z=1}^{N_z} 1/n_z \approx \ln N_z \approx \ln(L/B_0)$, and the final result is

$$\langle \zeta^2 \rangle \approx \frac{k_B T}{2\pi\gamma} \left[\frac{3R}{2L} + \ln \frac{L}{B_0} \right]. \tag{A.21}$$

Appendix B

Sample LAMMPS code for two TIP4P/2005 droplets coalescing in nitrogen

```
############################################################
# Water Droplets Coalescing in N2
############################################################
log             log.coalesce # log file to view output later
units           real # Use real units. See LAMMPS website
dimension       3 # 3D geometry
boundary        p p p # Periodic boundary conditions in all directions
neighbor        2.0 bin # Skin distance of 0.2 nm
neigh_ modify   every 1 delay 5 check yes # Modify neighbour list
processors      8 6 12 # Processors in three directions
read_ data      data.coalesce # Read data file
################################## INTERACTION PARAMETERS

# Define groups based on atom types and IDs
group   nitrogen type 3
group   hydrogen type 2
group   oxygen type 1
group   water union hydrogen oxygen
group   Drop1 id 1:582615
group   Drop2 id 582616:1165230

# Pair coefficients
pair_ style     hybrid lj/cut/tip4p/long 1 2 1 1 0.1546 13.0 12.6 lj/cut 9.375 # TIP4P/2005
kspace_ style   pppm/tip4p 1.0e-6 # Long-range interaction calculations using PPPM
pair_ modify    shift yes mix arithmetic # Cross-species interactions using LB rule
```

```
pair_ coeff    1 1 lj/cut/tip4p/long 0.1852 3.1589 # O-O
pair_ coeff    * 2 lj/cut/tip4p/long 0.0 0.0 # H-H
pair_ coeff    3 3 lj/cut 0.189 3.75 9.375 # N2-N2
pair_ coeff    2 3 lj/cut 0.0000 0.0 # N2-H
pair_ coeff    1 3 lj/cut 0.130 3.24 # N2-O

# Bond and angle parameters. Energy values are redundant because of SHAKE algorithm
bond_ style    harmonic
bond_ coeff    1 1000.00 0.9572
angle_ style   harmonic
angle_ coeff   1 100.0 104.52

################################## RUN PARAMETERS

# Compute species temperatures and number of neighbours
compute    nTemp Nitrogen temp
compute    d1Temp Drop1 temp/com
compute    d2Temp Drop2 temp/com
compute    coord oxygen coord/atom 13.0 1

# Pressure evaluation in whole Nitrogen
variable   dVol equal 3.1415*200*200*43 # Volume of one drop
compute    peratom Nitrogen stress/atom NULL
compute    p Nitrogen reduce sum c_ peratom[1] c_ peratom[2] c_ peratom[3]
variable   nPress equal -(c_ p[1]+c_ p[2]+c_ p[3])/(3*(vol-2*$dVol))

fix    SHAKE Water shake 0.0001 20 0 b 1 a 1 # SHAKE algorithm to make water molecules rigid
fix    NVE all nve # Perform simulation in a micro-canonical ensemble

# Output to log file
thermo_ style    custom step temp c_ d1Temp c_ d2Temp c_ nTemp v_ nPress pe etotal
thermo           200 # Output every 200 time steps
timestep         2.0 # Time step size in femto-seconds

# Impact velocity to droplets towards each other
velocity   Drop1 set 1e-5 NULL NULL sum yes units box
velocity   Drop2 set -1e-5 NULL NULL sum yes units box

# Output files for post-processing
dump   1 all custom 1000 R20P15.lammpstrj id type x y z
dump   2 oxygen custom 100 R20P15_ oxygen.dat id x y z vx vy vz c_ coord
dump   3 Nitrogen custom 100 R20P15_ nitrogen.dat id x y z vx vy vz
restart    50000 rst.R20P15
run        500000
```

Appendix C

Location of first contact between coalescing nanodroplets

The following derivation is due to Dr. Mykyta V. Chubynsky. [1] The purpose of this Appendix is to derive an expression for the finite extent within which the first contact between coalescing droplets (both 3D spherical and quasi-2D cylindrical) can happen.

The location at which two nanodroplets meet is a stochastic process; they do not always meet at the line of approach. Determining this distribution of onset locations theoretically is a complex problem, since it will need to take into account the thermal fluctuations on the surface and deserves separate consideration in this appendix. Scaling estimates of the size of the coalescence onset region will be proposed here, by comparing the surface fluctuations in the region to the variation of the mean distance between the surfaces within that region due to their curvature.

C.1 Spherical droplets (3D)

Consider two spherical droplets of radius R approaching each other along the line connecting their centres-of-mass (Fig. C.1). The coalescence is most likely to be initiated on the line of approach. However, when surface fluctuations are accounted for, there is a possibility that a point B on the surface of one droplets off the line of approach "overtakes" the more favourable point A on that line to initiate off-center coalescence. Suppose the distance between points A and B is $x \ll R$. Then the distance between the mean profiles at B is larger than that at A by

$$2Y(x) = 2(R - \sqrt{R^2 - x^2}) \approx x^2/R. \tag{C.1}$$

Let the deviations of the profile of one of the droplets at a given instant of time at A and B be ζ_A and ζ_B, respectively. It is reasonable to expect that the probability of coalescence at B is

1. Research Associate, University of Warwick

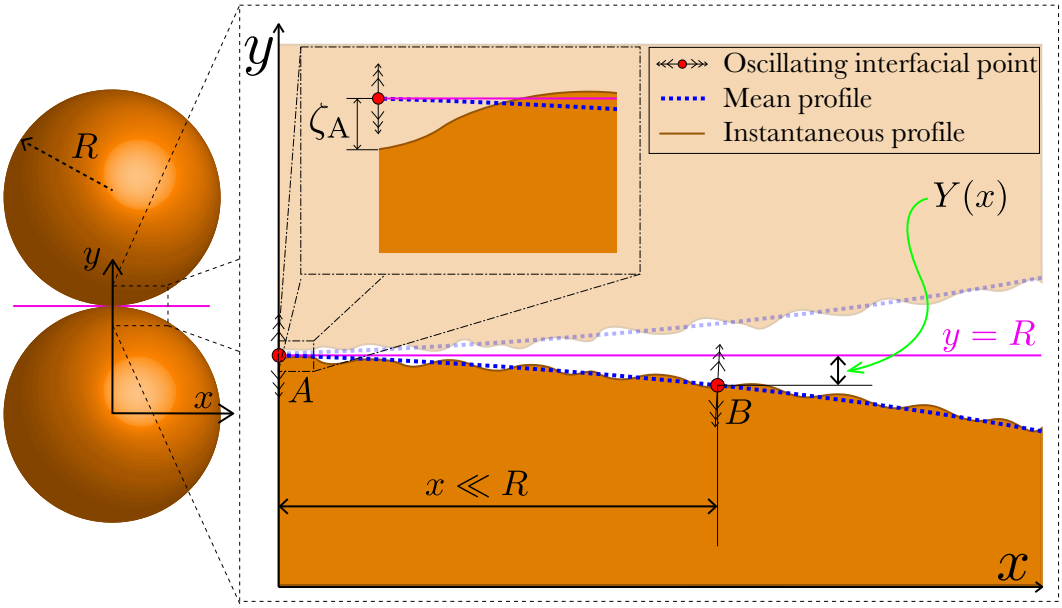

Figure C.1: Geometry of the coalescence onset problem for two 3D spherical droplets.

significant (comparable to that at A) if $\zeta_B - \zeta_A$ is likely to exceed $Y(x)$, or, in other words,

$$\left\langle (\zeta_B - \zeta_A)^2 \right\rangle \gtrsim Y^2(x) \approx \frac{x^4}{4R^2}. \tag{C.2}$$

The relative fluctuation $\zeta_B - \zeta_A$ is expected to be of the same order of magnitude as the typical fluctuations within a patch of size x, which, according to Eq. (3.1) and accompanying considerations, gives

$$\left\langle (\zeta_B - \zeta_A)^2 \right\rangle \approx \frac{k_B T}{2\pi\gamma} \ln\left(\frac{x}{B_0}\right). \tag{C.3}$$

The width of the distribution of coalescence onset locations, l_c, will be approximately equal to the value of x at which the left- and right-hand sides of Eq. (C.2) are equal, i.e.

$$\frac{k_B T}{2\pi\gamma} \ln\left(\frac{l_c}{B_0}\right) \approx \frac{l_c^4}{4R^2}, \tag{C.4}$$

so,

$$l_c \approx \left[\frac{2k_B T}{\pi\gamma} \ln\left(\frac{l_c}{B_0}\right)\right]^{1/4} R^{1/2}. \tag{C.5}$$

This is a transcendental equation that does not have a closed-form solution. However, in practice the logarithmic factor raised to a small power is of order unity, so for an order-of-magnitude estimate, it, along with the factor $(2/\pi)^{1/4}$, can be omitted, giving

$$l_c \approx \left(\frac{k_B T}{\gamma}\right)^{1/4} R^{1/2}. \tag{C.6}$$

C.2 Cylindrical droplets (quasi-2D)

For cylindrical droplets of axial length L, we use a similar approach. However, a complication arises that instead of a single point A at which the mean profile of the droplet is closest to that of the other droplet, there is now a line of such points. If point A is chosen arbitrarily on that line and point B on a line at distance x from the first line, the result for $\left\langle(\zeta_B - \zeta_A)^2\right\rangle$ will depend on where exactly A and B are chosen with respect to each other: the closer the points, the smaller that expression is. It can then be argued that choosing A as close to B as possible (i.e., at distance x) is reasonable, since in order for coalescence to be initiated at B, the gap between the droplets at *all* possible A needs to be larger. The result will then depend on the relation between x and L. If $x < L$, then, similar to the spherical case, the relative displacement $\zeta_B - \zeta_A$ is of the same order of magnitude as typical displacements in a patch of size x in both dimensions. If, however, $x > L$, then the patch is still of size x in the azimuthal direction, but cannot exceed L in the axial direction. For such an asymmetric patch, we use our quasi-2D expression (Eq. (3.3)) replacing R with $x/(2\pi)$. Then, arguing as before,

$$\frac{l_c^4}{4R^2} \approx \begin{cases} \frac{k_BT}{2\pi\gamma}\ln\left(\frac{l_c}{B_0}\right), & l_c < L, \\ \frac{k_BT}{2\pi\gamma}\left[\frac{3l_c}{4\pi L} + \ln\left(\frac{L}{B_0}\right)\right], & l_c > L. \end{cases} \tag{C.7}$$

Neglecting the logarithmic factor and term, and the numerical factors, gives

$$l_c \approx \begin{cases} \left(\frac{k_BT}{\gamma}\right)^{1/4} R^{1/2}, & l_c < L, \\ \left(\frac{k_BT}{\gamma L}\right)^{1/3} R^{2/3}, & l_c > L, \end{cases} \tag{C.8}$$

or

$$l_c \approx \begin{cases} \left(\frac{k_BT}{\gamma}\right)^{1/4} R^{1/2}, & R < L^2\left(\frac{\gamma}{k_BT}\right)^{1/2}, \\ \left(\frac{k_BT}{\gamma L}\right)^{1/3} R^{2/3}, & R > L^2\left(\frac{\gamma}{k_BT}\right)^{1/2}. \end{cases} \tag{C.9}$$

For the systems studied here, $L^2\left(\frac{\gamma}{k_BT}\right)^{1/2} \approx 73$ nm and they correspond to the top line of Eq. (C.9), which is the same expression as Eq. (C.6). For the three cylindrical droplets studied, $R =$ 11.1 nm, 20.1 nm and 58.5 nm, these correspond to $l_c =$1.7 nm, 2.2 nm and 3.8 nm, respectively.

Based on the above analysis, when two droplets of different radii coalesce, we expect no qualitative change in the results found in the current work. The effect of different radii may appear in two ways: 1) the droplets will now have different thermal fluctuation amplitudes, and 2) the gap thickness profile between the droplets will be modified, as this depends on the mean curvature between the droplets. For a realistic 3D system, the fluctuation amplitude depends only weakly on droplet sizes, so size will have a negligible effect on the overall process. As for

the gap thickness, its effect is that the coalescence will correspond to that of two droplets of the same curvature, equal to the mean curvature of the actual droplets.

Appendix D

Linear scaling of l_T on impact velocity

The following derivation is due to Dr. James E. Sprittles.[1] The purpose of this Appendix is to show that when droplets impact with each other, the extent of the thermal regime (l_T) scales linearly with the approach speed V_r.

Imagine a sphere falling through a plane at speed V_r and crossing an imaginary plane located at $z = 0$. When the point on the bottom part of the sphere hits the plane, it's height with respect to the plane is zero. As the sphere continues to pass through the plane, the height between the bottom point and the fixed plane becomes $z = -V_r t$. The peripheral point on the sphere that crosses the plane at this moment is given as $l = \sqrt{2RV_r t}$. This is obtained by noting that the contact line is a height $\sim l^2/(2R)$ above the base.

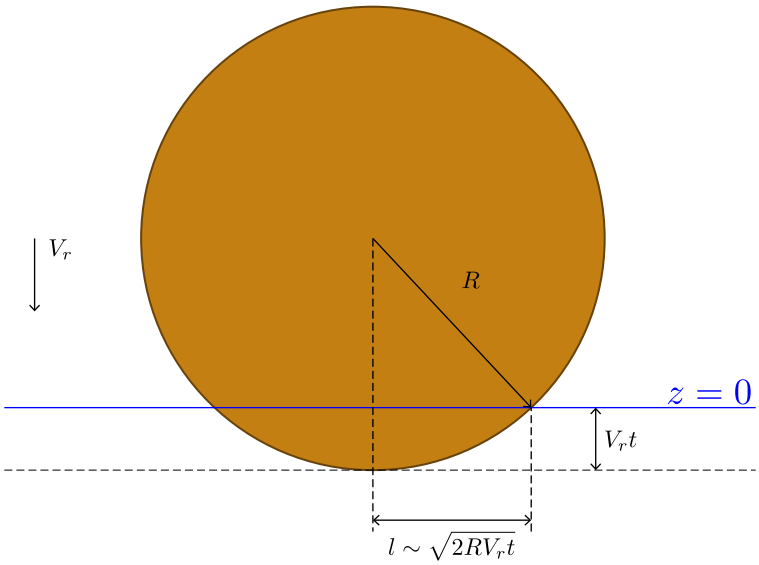

Figure D.1: Geometry of the problem where a sphere falls through a plane.

If the falling sphere were a droplet impacting on a surface (or two droplets impacting each

1. Associate Professor, University of Warwick

other), the speed at which the peripheral point (contact line) advances side ways is given by:

$$dl/dt \equiv V_g = \sqrt{\frac{RV_r}{2t}}, \tag{D.1}$$

This 'geometric mode' of bridge growth continues until the effect of surface tension kicks in and drives the coalescence process, which results in the usual hydrodynamic regime. Let us assume that the speed associated with this hydrodynamic mode is

$$V_h = C\frac{\gamma}{\mu}, \tag{D.2}$$

for some constant C. The crossover would happen when $V_g \sim V_h$, i.e. the geometric mode slows down enough for the hydrodynamic mode to take over. At this point

$$l = RV_r\frac{\mu}{\gamma}, \tag{D.3}$$

Therefore, this model predicts that the hydrodynamic mode will kick in at a length scale which varies linearly with approach speed V_r. Note that this approach does not predict a non-zero value of l_T as $V_r \to 0$. This clearly implies that the finite extent of thermal regime when approach speed is zero is a nanoscale effect.

Appendix E

Sample LAMMPS code for *m*W droplet spreading on a wall

```
############################################################
# Water Droplet Spreading
############################################################
log             log.spread # log file to view output later
units           real # Use real units. See LAMMPS website
dimension       3 # 3D geometry
boundary        p p p # Periodic boundary conditions in all directions
neighbor        2.0 bin # Skin distance of 0.2 nm
neigh_ modify   every 1 delay 5 check yes # Modify neighbour list
processors      8 6 12 # Processors in three directions
read_ data      data.spread # Read data file
################################## INTERACTION PARAMETERS

# Define groups based on atom types
group   Twall type 3
group   Bwall type 2
group   water type 1
group   wall union Bwall Twall
group   move union Twall water

# Pair coefficients
pair_ style     hybrid lj/cut 13.0 sw # LJ and mW potential
pair_ modify    shift yes

pair_ coeff     * * sw mW.sw Si NULL NULL # water-water
pair_ coeff     2* *3 lj/cut 15.975 2.471 # wall-wall
pair_ coeff     1 2*3 lj/cut 0.25 3.16 # water-wall
################################## RUN PARAMETERS

# Make bottom layers fixed and apply thermostat to the top few layers of the wall
```

```
fix             1 Bwall setforce 0.0 0.0 0.0
velocity        Twall create 300.0 34277 mom yes
fix             TWmom Twall momentum 2 linear 1 1 1
compute         Stemp Twall temp/com
fix             3 Twall temp/berendsen 300.0 300.0 100.0
fix_ modify     3 temp Stemp

# Compute temperature and potential energy of water molecules
compute     wtemp water temp/com
compute     wpe water pe/atom

# Output to log file
fix             5 move nve
timestep        10.0
thermo_ style   custom step temp c_ Stemp c_ wtemp pe etotal
thermo          200

# Impact velocity to droplet towards wall
velocity    water set -1e-5 NULL NULL sum yes units box

# Output files for post-processing
dump    1 all custom 5000 Spread.lammpstrj id type x y z
dump    2 water custom 100 water.lammpstrj id x y z c_ wpe
restart 50000 rst.Spread
run     500000
```

Appendix F

Relevance of van der Waals interactions between the droplets

The following derivation is due to Dr. Mykyta V. Chubynsky.[1] In our theoretical consideration, we have assumed that the average shapes of the droplets remain spherical as they approach each other, and the fluctuations of the surfaces of the two droplets are independent of each other and of the distance between them. In reality, droplets in proximity to each other interact. First, they may interact hydrodynamically via the medium in which they move. In our simulation setup, however, the medium is the droplets' own vapor and has a very low density, so that interaction is clearly negligible. A more interesting effect is the van der Waals (vdW) interactions between the molecules belonging to different droplets. These interactions change the average shape of the droplets as they approach each other and also correlate the fluctuations of their surfaces and modify their spectrum. The most dramatic manifestation of the latter effect is an instability, in which fluctuations grow exponentially until the droplets touch.

Based on the fact that our simulation results generally agree with our theory and, in particular, there is no evidence of either a significant shape change or an instability, we have concluded that these effects probably do not play an important role under the conditions of our simulations. This is particularly interesting in view of the fact that it is the vdW-driven instability that is considered in many works (see, e.g., Ref. Chesters (1991)) as giving rise to coalescence between the droplets. In fact, there is no contradiction, since our work differs from these previous ones in two respects: first, we simulate much smaller, nanoscale droplets, and second, as mentioned above, our simulations are carried out essentially in vacuum, which, by eliminating hydrodynamic interactions, affects the shape of the droplets and thus the effect of vdW interactions as well. The purpose of this section is to consider the role of these two factors. We take vdW interactions into account by introducing the disjoining pressure contribution to the normal stress at the boundary i.e

$$p_{\mathrm{vdW}} = -\frac{A_H}{48\pi H^3}, \tag{F.1}$$

1. Research Associate, University of Warwick

where A_H is the material-dependent Hamaker constant, and H is one-half the separation between the surfaces.

We start by considering two very large volumes of liquid, separated by a vacuum gap between two planar parallel surfaces. Ignoring first the interactions between the surfaces, we assume that their thermal fluctuations are not large enough to bridge the gap (thus, strictly speaking, the surfaces cannot be infinitely large, since the fluctuations diverge as the size of the surface grows; however, this divergence is only logarithmic, so we will assume that the surfaces are infinite for all other intents and purposes). Nevertheless, when the interactions are "switched on", this system will still be unstable: the fluctuations with wavelengths above a critical one, λ_c, will grow exponentially. This critical wavelength corresponds to the surface perturbation mode for which the local changes in the disjoining pressure are exactly compensated by those in the Laplace pressure, which gives

$$k_c = 2\pi/\lambda_c = \left(\frac{a_H}{\gamma}\right)^{1/2}, \tag{F.2}$$

where

$$a_H = \frac{A_H}{16\pi H^4} \tag{F.3}$$

For large H, the growth rates σ_k [defined so that the corresponding mode grows as $\exp(\sigma_k t)$] are so small that this growth may not matter for practical purposes. A general expression for the growth rate exists Lucassen *et al.* (1970), but it is more convenient to use much simpler ones valid in the two limits, inertial and viscous, in both cases assuming $kH \ll 1$, and interpolate between them.

For small wavenumbers k, the growth rate is limited by the liquid inertia and is given by

$$\sigma_k = \left[\frac{(a_H - \gamma k^2)k}{\rho}\right]^{1/2}, \tag{F.4}$$

where ρ is the liquid density. For large k, it is limited by the viscosity μ and is

$$\sigma_k = \frac{a_H - \gamma k^2}{2\mu k}. \tag{F.5}$$

Both expressions vanish above k_c. Since σ_k grows as $k^{1/2}$ for small k and decreases to zero as $k \to k_c$, there is always a maximum, either at k at which Eq. (F.4) has a maximum ($k^i_{\max}$), or at the crossover k_x where Eqs. (F.4) and (F.5) are equal, whichever of the two values of k is smaller. The maximum of Eq. (F.4) is at

$$k^i_{\max} = \left(\frac{a_H}{3\gamma}\right)^{1/2}, \tag{F.6}$$

while the crossover is the solution of

$$\frac{4\mu^2}{\rho}k_x^3+\gamma k_x^2=a_H, \tag{F.7}$$

which is

$$k_x\approx\begin{cases}\left(\frac{\rho a_H}{4\mu^2}\right)^{1/3}, & a_H>\frac{\rho^2\gamma^3}{16\mu^4},\\ \left(\frac{a_H}{\gamma}\right)^{1/2}, & a_H<\frac{\rho^2\gamma^3}{16\mu^4}.\end{cases} \tag{F.8}$$

The second line of this gives $k_x\approx k_c>k_{\max}^i$ and therefore is irrelevant. Then the value $k_{\max}$ at which the maximum rate is reached is either Eq. (F.6) or the top line of Eq. (F.8), i.e.

$$k_{\max}\approx\begin{cases}\left(\frac{\rho a_H}{4\mu^2}\right)^{1/3}, & a_H>\frac{27\rho^2\gamma^3}{16\mu^4},\\ \left(\frac{a_H}{3\gamma}\right)^{1/2}, & a_H<\frac{27\rho^2\gamma^3}{16\mu^4}.\end{cases} \tag{F.9}$$

The corresponding maximum growth rate is

$$\sigma_{\max}\approx\begin{cases}\left(\frac{a_H^2}{2\mu\rho}\right)^{1/3}, & a_H>\frac{27\rho^2\gamma^3}{16\mu^4},\\ \left(\frac{4a_H^3}{27\gamma\rho^2}\right)^{1/4}, & a_H<\frac{27\rho^2\gamma^3}{16\mu^4}.\end{cases} \tag{F.10}$$

There is a discontinuity, since an exact expression is used in the bottom line, but an approximate one in the top line, but it is relatively small and insignificant for our purposes. Note also that given Eq. (F.3), $\sigma_{\max}$ increases very rapidly when H decreases ($\propto H^{-8/3}$ in one regime and $\propto H^{-3}$ in the other). Individual modes grow quite rapidly, too: neglecting the γk^2 terms, the growth is $\propto H^{-2}$ in the inertial regime and $\propto H^{-4}$ in the viscous one.

Suppose now that the two liquid volumes approach each other with relative speed $2v$ so that H decreases linearly in time as H_0-vt. Even with vdW interactions "switched off", the surfaces would touch before $H=0$ due to fluctuations. Suppose this typically happens when $H=H_{\min}$. Then the question is whether the growth of the fluctuations due to the instability is significant before $H=H_{\min}$. We can still estimate the growth using Eqs. (F.4) and (F.5), keeping in mind that σ_k is now time-dependent. For the amplitude of a mode with wavenumber k we can write

$$a_k(t)\sim\exp\left(\int_0^t\sigma_k(t')dt'\right). \tag{F.11}$$

Because of the fast growth of σ_k with decreasing H, the value of σ_k at $H_{\min}$ dominates and the modes with the most growth are those with $k=k_{\max}(H_{\min})$. These modes grow by a factor

$$F_{\max}\simeq\exp[\sigma_{\max}(H_{\min})\Delta t], \tag{F.12}$$

where Δt is the effective time interval during which the growth rate is close to maximal and is

$$\Delta t = \alpha H_{\min}/v, \tag{F.13}$$

with α a numerical factor of order (but likely somewhat below) unity, e.g., $\alpha = 1/(\beta - 1)$ for $\sigma_k(t) \propto (H_0/v - t)^{-\beta}$. Then, finally, the instability is not significant if

$$\sigma_{\max}(H_{\min})\Delta t < 1, \tag{F.14}$$

and significant otherwise.

The answer to the question above about significance of the instability depends on $H_{\min}$. For a rough estimate, we choose $H_{\min} = 1$ nm, which is the typical size of fluctuations of drop surfaces. Then for water ($\gamma = 65$ mN/m, $\mu = 10^{-3}$ Pa s, $\rho = 10^3$ kg/m^3, $A_H = 3.7 \times 10^{-20}$ J) we find that this corresponds to the top lines of Eqs. (F.9) and (F.10) (though close to the boundary between the regimes) and then $k_{\max} \approx 6 \times 10^7$ m^{-1}, $\sigma_{\max} \approx 6 \times 10^9$ s^{-1}. Then, according to Eq. (F.14) and assuming $\alpha = 1$, the instability is insignificant for $v > 6$ m/s, a moderate speed relevant experimentally, and the threshold may be even lower if $\alpha < 1$.

Are the above results relevant to spherical droplets of a finite size? The vacuum gap between the droplets is finite in extent and its width varies with the distance from the axis. This changes the surface modes and their spectrum. However, near the axis the gap width can be considered roughly constant. We define the "flat part" of the gap as that part of it where its width does not exceed $1 + s$ times the width on the axis, where $s \sim 1$. Then, assuming that H is much smaller than the radius of the droplet R, the radius of this "flat part" is

$$r_f \approx (2sRH)^{1/2}. \tag{F.15}$$

There will be modes oscillating many times within the "flat part"; these modes will have a well-defined wavenumber and for them the previous results obtained above for a flat infinite gap should remain valid. On the other hand, modes with wavelength above $\approx 4r_f$ (or $k < k_{\min} \approx \pi/(2r_f)$) do not exist. Then, if $k_{\min} < k_{\max}$ [Eq. (F.9)], the above results for the maximum growth rate (as well as those for significance of the instability) should remain valid; if, however, $k_{\min} > k_{\max}$, then the growth should be slower, being determined by the "flat-gap" rate for $k_{\min}$, rather than $k_{\max}$ (this rate may, in fact, be negative). The condition $k_{\min} < k_{\max}$ gives

$$\frac{\pi}{2r_f} < k_{\max}, \tag{F.16}$$

or

$$R > \frac{\pi^2}{8sHk_{\max}^2}. \tag{F.17}$$

For water and $H_{\min} = 1$ nm, we have obtained $k_{\max} \approx 6 \times 10^7$ m^{-1}, which, assuming $s = 1$,

gives $R \gtrsim 300$ nm. Thus, our estimates should be roughly valid for macroscopic (e.g., mm-sized) droplets; however, for smaller droplets, like those used in our simulations, the rate should be slower and therefore even for slower approach speeds there should be no significant vdW effect, in agreement with our simulation results.

Another effect of vdW interactions that we have ignored so far is their influence on the average shape of the droplets. Since the disjoining pressure depends on the distance between the surfaces, its contribution is not constant on a spherical surface, which gives rise to pressure gradients. This creates flows that distort the surface. The process is similar to that giving rise to the instabilities that we have considered above, but with a specific length scale on the order of r_f (the size of the region on the surface where the interaction is the strongest). It is reasonable to assume then that the time scale of the process is similar to that for development of the instability with $k = k_{\min}$ (except perhaps with $\gamma \approx 0$, as the pressure gradient is created by vdW forces and is not initially counterbalanced by the Laplace pressure). This time scale is normally either comparable to or longer than the shortest time scale of the instability development and so this distortion process is never more important.

This explains how our results are different from what is commonly found in the literature where the effect of the vdW instability is dominant. In part, the difference does indeed arise from the fact that the growth rate is smaller for drops of nanometer size. However, a more important factor is that when drops collide in a medium, a thin film between them exists for a relatively long time (milliseconds for mm-sized drops), which is more than sufficient for the instability to develop, even if the growth rate is smaller than the value of $\sigma_{\max}$ quoted here due to the film being thicker than 1 nm.

The discussion above indicates that the biggest contribution of vdW interactions between the droplets arises within a short interval immediately preceding coalescence, of duration less than the time it takes the droplets to move a distance equal to the size of the fluctuations. Given that this size is somewhat below 1 nm for our droplets, the cut-off of 1.3 nm in our molecular dynamics simulations appears adequate.

Appendix G

VoF simulation details for coalescence-induced jumping of nanodroplets

VoF simulations in this work were conducted by Dr Ryan Enright [1] as part of a collaborative project with industry. The VoF results from this Appendix are used only in Fig. 5.15 to show where the MD results lie in terms of the overall macroscopic picture.

Numerical simulations.—To study droplet coalescence and subsequent jumping on an ideal superlyophobic surface, we simulate the case of symmetric binary coalescence using the volume-of-fluid (VoF) approach with custom user-defined function for automated mesh adaption in order to well resolve the liquid/gas interface implemented in a finite-volume solver (Fluent v17.0, Ansys Inc.).

A uniform structured grid is used as the parent mesh. Three levels of adaption (cell splitting) are allowed providing for a minimum cell volume (V_{min}) in the interface region with characteristic length ($V_{min}^{1/3}$) of 1.9% the initial droplet radius, R. To simulate an ideal, non-wetting surface, the droplet wetting wall is assigned a single valued contact angle of $\theta_c = 180°$. Due to symmetry, only one quarter of the domain is simulated with dimensions of $3R \times 3R \times 5R$. The simulation domain is bounded by two symmetry planes dissecting the droplets where, by definition, the contact angle is constant at $\pi/2$; two boundaries specified with a shear-stress free condition (on the gas); the droplet wetting wall specified as no-slip (which still permits contact line motion, due to the 180° contact angle) and a single valued contact angle (contact angle hysteresis neglected); and an outlet vent, with backflow direction specified from neighbouring cell, opposite to the droplet wetting wall.

The droplet volume is patched into the simulation domain with a geometry corresponding to the droplets just in contact. The limited grid resolution led to an initial bridge radius of $\approx 0.1R$ that initiated the start of coalescence at $t = 0$. The properties of the liquid droplet, the surrounding gas and the interface between them are nominally those of water and humid air at

1. Senior Member of Technical Staff, Nokia Bell Labs, Ireland

room temperature (argon and argon vapor at 85 K), which corresponds to a nominal viscosity ratio, density ratio and surface tension of $\mu_l/\mu_g = 56$ (40) and $\rho_l/\rho_g = 815$ (307), $\gamma = 65.4$ (8.3) mN/m respectively. To simulate other viscosity ratios, the gas side viscosity is modified accordingly. The density ratio is kept fixed at the nominal base value for each simulation.

Discretization for pressure, momentum and volume fraction is done with the PRESTO!, QUICK and Geo-Reconstruct algorithms, respectively. The PISO algorithm is used for pressure-velocity coupling. The CSF model is used to capture the contribution of surface tension to the normal stress on the interface (Hirt and Nichols, 1981). The VoF implementation is intrinsically volume conserving (Brackbill *et al.*, 1992). This is confirmed for all simulations by tracking the volume of the droplet phase during the simulations. The liquid-vapor interface is implicitly represented by the VoF function, which varies rapidly over a short distance, approximately the mesh cell size. This abrupt change of the VoF function creates errors in calculating the normal vectors and the curvature of the interface used to evaluate the interfacial forces. These errors induce non-physical parasitic currents in the interfacial region, e.g. spurious velocities. Good results in reducing spurious velocities are obtained by using Fluent's native smoothing function. One fully-weighted cycle of smoothing at each iteration is found to be suitable for the simulations. Under-smoothing, by reducing the weighting for a single smoothing cycle, led to noisy results and, in some cases, droplets that would begin accelerating after contact with the surface had been lost. Over-smoothing should also be avoided as this unphysically reduces the local curvature of the bridging region leading to a reduction in the simulated jumping speed. Adaptive time stepping was used to control the progression of the simulation. An initial period of 10 constant time steps ($t/\tau \leq 1 \times 10^{-2}$) was followed by varying time steps maintaining the global Courant number of 0.5. At the same time, the mesh was adapted every 10 time steps. This ensured that the interface never left the region of highest refinement during the simulation.

Determination of jumping speed from simulations.— Droplet jumping speeds are determined from simulations by calculating the mass-averaged droplet velocity when the droplet lost contact with the surface. It should be noted that, during the coalescence process, the droplet typically loses contact with the substrate twice. The first instance occurs during the initial bridge development where the entrainment liquid from the droplet bulk into the developing bridge region results in loss of contact with the substrate. As the liquid bridge expands, it eventually impacts the substrate leading to a substantial increase in the wetted area of liquid on the substrate. The point of departure was found to correlate well with normal force on the wall reaching a local negative maximum. An alternative definition of the jumping speed could be determined as when the droplet lost viscous communication with the wall after the local negative maximum normal force on the wall marked by a decay to zero transient force on the wall. This definition coincides with the observed start of a smooth linear decay in droplet velocity due primarily to drag with the surrounding fluid. The two definitions of jumping speed converge as the viscosity ratio approaches zero.

References

Aarts, D. G. A. L., Schmidt, M., and Lekkerkerker, H. N. W. Direct visual observation of thermal capillary waves. *Science*, 304(5672):847–850, 2004.

Aarts, D. G. A. L., Lekkerkerker, H. N. W., Guo, H., Wegdam, G. H., and Bonn, D. Hydrodynamics of droplet coalescence. *Phys. Rev. Lett.*, 95:164503, 2005.

Abascal, J. L. and Vega, C. A general purpose model for the condensed phases of water: TIP4P/2005. *J. Chem. Phys.*, 123(23):234505, 2005.

Agasthya, L., Picardo, J. R., Ravichandran, S., Govindarajan, R., and Ray, S. S. Understanding droplet collisions through a model flow: Insights from a burgers vortex. *Phys. Rev. E*, 99: 063107, 2019.

Allen, M. P. and Tildesley, D. J. *Computer Simulation of Liquids*. Oxford University Press, New York, 2 edition, 2017.

Berendsen, H. J. C., Grigera, J. R., and Straatsma, T. P. The missing term in effective pair potentials. *J. Phys. Chem.*, 91(24):6269–6271, 1987.

Bertrand, E., Blake, T. D., and De Coninck, J. Influence of solid–liquid interactions on dynamic wetting: a molecular dynamics study. *J. Phys. Condens. Matter*, 21(46):464124, 2009.

Bird, J. C., Mandre, S., and Stone, H. A. Short-time dynamics of partial wetting. *Phys. Rev. Lett.*, 100:234501, 2008.

Bird, J. C., Ristenpart, W. D., Belmonte, A., and Stone, H. A. Critical angle for electrically driven coalescence of two conical droplets. *Phys. Rev. Lett.*, 103:164502, 2009.

Blake, T. D. and De Coninck, J. Dynamics of wetting and Kramers' theory. *Eur. Phys. J. Special Topics*, 197(1):249–264, 2011.

Blake, T. D., Clarke, A., De Coninck, J., and de Ruijter, M. J. Contact angle relaxation during droplet spreading: Comparison between molecular kinetic theory and molecular dynamics. *Langmuir*, 13(7):2164–2166, 1997.

Blake, T. and De Coninck, J. The influence of solid-liquid interactions on dynamic wetting. *Adv. Colloid Interface Sci.*, 96(1-3):21–36, 2002.

Blake, T. and Haynes, J. Kinetics of liquid-liquid displacement. *J. Colloid Interface Sci.*, 30 (3):421 – 423, 1969.

Bohn, H. F. and Federle, W. Insect aquaplaning: Nepenthes pitcher plants capture prey with the peristome, a fully wettable water-lubricated anisotropic surface. *Proc. Natl. Acad. Sci. U.S.A*, 101(39):14138–14143, 2004.

Boneberg, J., Habenicht, A., Benner, D., Leiderer, P., Trautvetter, M., Pfahler, C., Plettl, A., and Ziemann, P. Jumping nanodroplets: a new route towards metallic nano-particles. *Appl. Phys. A*, 93(2):415–419, 2008.

Bonn, D., Eggers, J., Indekeu, J., Meunier, J., and Rolley, E. Wetting and spreading. *Rev. Mod. Phys.*, 81:739–805, 2009.

Boreyko, J. B. and Chen, C. H. Self-propelled dropwise condensate on superhydrophobic surfaces. *Phys. Rev. Lett.*, 103(18):2–5, 2009.

Boreyko, J. B. and Collier, C. P. Delayed frost growth on jumping-drop superhydrophobic surfaces. *ACS Nano*, 7(2):1618–1627, 2013.

Boreyko, J. B., Zhao, Y., and Chen, C.-H. Planar jumping-drop thermal diodes. *Appl. Phys. Lett.*, 99(23):234105, 2011.

Brackbill, J., Kothe, D., and Zemach, C. A continuum method for modeling surface tension. *J. Comput. Phys.*, 100(2):335 – 354, 1992.

Brinker, C. J., Lu, Y., Sellinger, A., and Fan, H. Evaporation-induced self-assembly: Nanostructures made easy. *Adv. Mater*, 11(7):579–585, 1999.

Burton, J. C. and Taborek, P. Role of dimensionality and axisymmetry in fluid pinch-off and coalescence. *Phys. Rev. Lett.*, 98:224502, 2007.

Camisasca, G., Pathak, H., Wikfeldt, K. T., and Pettersson, L. G. M. Radial distribution functions of water: Models vs experiments. *J. Chem. Phys.*, 151(4):044502, 2019.

Case, S. C. Coalescence of low-viscosity fluids in air. *Phys. Rev. E*, 79:026307, 2009.

Case, S. C. and Nagel, S. R. Coalescence in low-viscosity liquids. *Phys. Rev. Lett.*, 100: 084503, 2008.

Cha, H., Xu, C., Sotelo, J., Chun, J. M., Yokoyama, Y., Enright, R., and Miljkovic, N. Coalescence-induced nanodroplet jumping. *Phys. Rev. Fluids*, 1:064102, 2016.

Chen, N., Kuhl, T., Tadmor, R., Lin, Q., and Israelachvili, J. Large deformations during the coalescence of fluid interfaces. *Phys. Rev. Lett.*, 92:024501, 2004.

Chen, S., Wang, J., Ma, T., and Chen, D. Molecular dynamics simulations of wetting behavior of water droplets on polytetrafluorethylene surfaces. *J. Chem. Phys.*, 140(11):114704, 2014.

Chesters, A. K. The modelling of coalescence processes in fluid-liquid dispersions: A review of current understanding. *Chem. Eng. Res. Des.*, 69A:259–270, 1991.

Chireux, V., Protat, M., Risso, F., Ondarçuhu, T., and Tordjeman, P. Jump-to-contact instability: The nanoscale mechanism of droplet coalescence in air. *Phys. Rev. Fluids*, 3:102001, 2018.

Cormier, S. L., McGraw, J. D., Salez, T., Raphaël, E., and Dalnoki-Veress, K. Beyond tanner's law: Crossover between spreading regimes of a viscous droplet on an identical film. *Phys. Rev. Lett.*, 109:154501, 2012.

Cox, R. G. The dynamics of the spreading of liquids on a solid surface. part 1. viscous flow. *J. Fluid Mech.*, 168:169–194, 1986.

de Gans, B.-J., Duineveld, P., and Schubert, U. Inkjet printing of polymers: State of the art and future developments. *Adv. Mater*, 16(3):203–213, 2004.

de Gennes, P. G. Wetting: statics and dynamics. *Rev. Mod. Phys.*, 57:827–863, 1985.

de Ruijter, M. J., Blake, T. D., and De Coninck, J. Dynamic wetting studied by molecular modeling simulations of droplet spreading. *Langmuir*, 15(22):7836–7847, 1999.

Dhabal, D., Chakravarty, C., Molinero, V., and Kashyap, H. K. Comparison of liquid-state anomalies in stillinger-weber models of water, silicon, and germanium. *J. Chem. Phys.*, 145 (21):214502, 2016.

Dimitrakopoulos, P. and Higdon, J. J. L. On the gravitational displacement of three-dimensional fluid droplets from inclined solid surfaces. *J. Fluid Mech.*, 395:181–209, 1999.

Dror, R. O., Dirks, R. M., Grossman, J., Xu, H., and Shaw, D. E. Biomolecular simulation: A computational microscope for molecular biology. *Annu. Rev. Biophys.*, 41(1):429–452, 2012.

Duchemin, L., Eggers, J., and Josserand, C. Inviscid coalescence of drops. *J. Fluid Mech.*, 487: 167–178, 2003.

Dussan, E. B. On the spreading of liquids on solid surfaces: Static and dynamic contact lines. *Annu. Rev. Fluid Mech*, 11(1):371–400, 1979.

Dussan V., E. B. and Davis, S. H. On the motion of a fluid-fluid interface along a solid surface. *J. Fluid Mech.*, 65(1):71–95, 1974.

Duvivier, D., Blake, T. D., and De Coninck, J. Toward a predictive theory of wetting dynamics. *Langmuir*, 29(32):10132–10140, 2013.

Eggers, J. and Villermaux, E. Physics of liquid jets. *Rep. Prog. Phys.*, 71(3):036601, 2008.

Eggers, J., Lister, J. R., and Stone, H. A. Coalescence of liquid drops. *J. Fluid Mech.*, 401: 293–310, 1999.

Eiswirth, R. T., Bart, H.-J., Ganguli, A. A., and Kenig, E. Y. Experimental and numerical investigation of binary coalescence: Liquid bridge building and internal flow fields. *Phys. Fluids*, 24(6):062108, 2012.

Enright, R., Miljkovic, N., Al-Obeidi, A., Thompson, C. V., and Wang, E. N. Condensation on superhydrophobic surfaces: the role of local energy barriers and structure length scale. *Langmuir*, 28(40):14424–32, 2012.

Enright, R., Miljkovic, N., Dou, N., Nam, Y., and Wang, E. N. Condensation on Superhydrophobic Copper Oxide Nanostructures. *J. Heat Transfer*, 135(9):091304, 2013.

Enright, R., Miljkovic, N., Sprittles, J., Nolan, K., Mitchell, R., and Wang, E. N. How Coalescing Droplets Jump. *ACS Nano*, 8(10):10352–10362, 2014.

Enriquez, O. R., Marin, A. G., Winkels, K. G., and Snoeijer, J. H. Freezing singularities in water drops. *Phys. Fluids*, 24(9):091102, 2012.

Farokhirad, S., Morris, J. F., and Lee, T. Coalescence-induced jumping of droplet: Inertia and viscosity effects. *Phys. Fluids*, 27(10):102102, 2015.

Gao, S., Liao, Q., Liu, W., and Liu, Z. Coalescence-induced jumping of nanodroplets on textured surfaces. *J. Phys. Chem. Lett.*, 9(1):13–18, 2018.

Gillespie, T. and Rideal, E. K. The coalescence of drops at an oil-water interface. *Trans. Faraday Soc.*, 52:173–183, 1956.

Hennequin, Y., Aarts, D. G. A. L., van der Wiel, J. H., Wegdam, G., Eggers, J., Lekkerkerker, H. N. W., and Bonn, D. Drop formation by thermal fluctuations at an ultralow surface tension. *Phys. Rev. Lett.*, 97:244502, 2006.

Hirt, C. and Nichols, B. Volume of fluid (vof) method for the dynamics of free boundaries. *J. Comput. Phys.*, 39(1):201 – 225, 1981.

Hocking, L. M. The effect of slip on the motion of a sphere close to a wall and of two adjacent spheres. *J. Eng. Math*, 7(3):207–221, 1973.

Hocking, L. M. A moving fluid interface on a rough surface. *J. Fluid Mech.*, 76(4):801–817, 1976.

Hockney, R. W. and Eastwood, J. W. *Computer Simulation Using Particles*. CRC Press, 1988.

Hopper, R. W. Coalescence of two equal cylinders: Exact results for creeping viscous plane flow driven by capillarity. *J. Am. Ceram. Soc*, 67(12):262–264, 1984.

Hopper, R. W. Plane stokes flow driven by capillarity on a free surface. *J. Fluid Mech.*, 213: 349–375, 1990.

Huh, C. and Mason, S. Effects of surface roughness on wetting (theoretical). *J. Colloid Interface Sci.*, 60(1):11 – 38, 1977.

Huh, C. and Scriven, L. Hydrodynamic model of steady movement of a solid/liquid/fluid contact line. *J. Colloid Interface Sci.*, 35(1):85 – 101, 1971.

Jeong, J.-T. and Moffatt, H. K. Free-surface cusps associated with flow at low reynolds number. *J. Fluid Mech*, 241:1–22, 1992.

Jorgensen, W. L., Chandrasekhar, J., Madura, J. D., Impey, R. W., and Klein, M. L. Comparison of simple potential functions for simulating liquid water. *J. Chem. Phys.*, 79(2):926–935, 1983.

Kim, H.-Y., Lee, H. J., and Kang, B. H. Sliding of liquid drops down an inclined solid surface. *J. Colloid Interface Sci.*, 247(2):372 – 380, 2002.

Komatsu, H., Okada, S., and Handa, T. Suppressive effects of salts on droplet coalescence in a commercially available fat emulsion during freezing for storage. *J. Pharm. Sci*, 86(4):497 – 502, 1997.

Kovetz, A. and Olund, B. The effect of coalescence and condensation on rain formation in a cloud of finite vertical extent. *J. Atmos. Sci.*, 26(5):1060–1065, 1969.

Kumar, S., Narsimhan, G., and Ramkrishna, D. Coalescence in Creaming Emulsions. Existence of a Pure Coalescence Zone. *Ind. Eng. Chem. Res.*, 35(9):3155–3162, 1996.

Liang, Z. and Keblinski, P. Coalescence-induced jumping of nanoscale droplets on superhydrophobic surfaces. *Appl. Phys. Lett.*, 107(14):0–5, 2015.

Liu, F., Ghigliotti, G., Feng, J. J., and Chen, C.-H. Numerical simulations of self-propelled jumping upon drop coalescence on non-wetting surfaces. *J. Fluid Mech.*, 752:39–65, 2014.

Lucassen, J., van den Tempel, M., Vrij, A., and Hesselink, F. T. Waves in thin liquid films. i. the different modes of vibration. *Proc. K. Ned. Akad. Wet. Ser. B Phys. Sci.*, 73:109–123, 1970.

Lukyanov, A. V. and Likhtman, A. E. Dynamic contact angle at the nanoscale: A unified view. *ACS Nano*, 10(6):6045–6053, 2016.

Lv, C., Hao, P., Yao, Z., and Niu, F. Departure of condensation droplets on superhydrophobic surfaces. *Langmuir*, 31(8):2414–2420, 2015.

Ma, Z., Gamage, R. P., Rathnaweera, T., and Kong, L. Review of application of molecular dynamic simulations in geological high-level radioactive waste disposal. *Appl. Clay Sci.*, 168:436 – 449, 2019.

Manor, O., Vakarelski, I. U., Tang, X., O'Shea, S. J., Stevens, G. W., Grieser, F., Dagastine, R. R., and Chan, D. Y. C. Hydrodynamic boundary conditions and dynamic forces between bubbles and surfaces. *Phys. Rev. Lett.*, 101:024501, 2008.

Marin, A. G., Enriquez, O. R., Brunet, P., Colinet, P., and Snoeijer, J. H. Universality of tip singularity formation in freezing water drops. *Phys. Rev. Lett.*, 113:054301, 2014.

Menchaca-Rocha, A., Martínez-Dávalos, A., Núñez, R., Popinet, S., and Zaleski, S. Coalescence of liquid drops by surface tension. *Phys. Rev. E*, 63(4):046309, 2001.

Miljkovic, N., Enright, R., and Wang, E. N. Effect of Droplet Morphology on Growth Dynamics and Heat Transfer during Condensation on Superhydrophobic Nanostructured Surfaces. *ACS Nano*, 6(2):1776–1785, 2012.

Miljkovic, N., Enright, R., Nam, Y., Lopez, K., Dou, N., Sack, J., and Wang, E. N. Jumping-droplet-enhanced condensation on scalable superhydrophobic nanostructured surfaces. *Nano Lett.*, 13(1):179–187, 2013.

Miljkovic, N., Preston, D. J., Enright, R., and Wang, E. N. Jumping-droplet electrostatic energy harvesting. *Appl. Phys. Lett.*, 105(1):013111, 2014.

Mockenhaupt, B., Ensikat, H.-J., Spaeth, M., and Barthlott, W. Superhydrophobicity of biological and technical surfaces under moisture condensation: Stability in relation to surface structure. *Langmuir*, 24(23):13591–13597, 2008.

Moffatt, H. K. Singularities in fluid mechanics. *Phys. Rev. Fluids*, 4:110502, 2019.

Molinero, V. and Moore, E. B. Water modeled as an intermediate element between carbon and silicon. *J. Phys. Chem. B*, 113(13):4008–4016, 2009.

Mouterde, T., Nguyen, T.-V., Takahashi, H., Clanet, C., Shimoyama, I., and Quéré, D. How merging droplets jump off a superhydrophobic surface: Measurements and model. *Phys. Rev. Fluids*, 2:112001, 2017.

Nam, Y., Kim, H., and Shin, S. Energy and hydrodynamic analyses of coalescence-induced jumping droplets. *Appl. Phys. Lett.*, 103(16):161601, 2013.

Nitsche, L. C. and Bernal, B. A. Stokes flow singularity at a corner joining solid and porous walls at arbitrary angle. *J. Eng. Math*, 108(1):1–23, 2018.

O'neill, G. A. and Westwater, J. Dropwise condensation of steam on electroplated silver surfaces. *Int. J. Heat Mass Transf.*, 27(9):1539 – 1549, 1984.

Paulsen, J. D., Burton, J. C., and Nagel, S. R. Viscous to inertial crossover in liquid drop coalescence. *Phys. Rev. Lett.*, 106(11):114501, 2011.

Paulsen, J. D., Burton, J. C., Nagel, S. R., Appathurai, S., Harris, M. T., and Basaran, O. A. The inexorable resistance of inertia determines the initial regime of drop coalescence. *Proc. Natl. Acad. Sci. U. S. A.*, 109(18):6857–6861, 2012.

Peng, B., Wang, S., Lan, Z., Xu, W., Wen, R., and Ma, X. Analysis of droplet jumping phenomenon with lattice boltzmann simulation of droplet coalescence. *Appl. Phys. Lett.*, 102(15):151601, 2013.

Perumanath, S., Borg, M. K., Chubynsky, M. V., Sprittles, J. E., and Reese, J. M. Droplet coalescence is initiated by thermal motion. *Phys. Rev. Lett.*, 122:104501, 2019.

Phillips, W. F. Drag on a small sphere moving through a gas. *Phys. Fluids*, 18(9):1089–1093, 1975.

Plimpton, S. Fast Parallel Algorithms for Short - Range Molecular Dynamics. *J. Comput. Phys.*, 117:1–19, 1995.

Pothier, J. C. and Lewis, L. J. Molecular-dynamics study of the viscous to inertial crossover in nanodroplet coalescence. *Phys. Rev. B*, 85(11):115447, 2012.

Prevost, M. and Gallez, D. Nonlinear rupture of thin free liquid films. *J. Chem. Phys.*, 84(7): 4043–4048, 1986.

Qian, J. and Gao, H. Scaling effects of wet adhesion in biological attachment systems. *Acta Biomater.*, 2(1):51–58, 2006.

Qin, X., Yuan, Q., Zhao, Y., Xie, S., and Liu, Z. Measurement of the rate of water translocation through carbon nanotubes. *Nano Lett.*, 11(5):2173–2177, 2011.

Ramisetti, S. B., Borg, M. K., Lockerby, D. A., and Reese, J. M. Liquid slip over gas nanofilms. *Phys. Rev. Fluids*, 2:084003, 2017.

Rana, A. S., Lockerby, D. A., and Sprittles, J. E. Lifetime of a nanodroplet: Kinetic effects and regime transitions. *Phys. Rev. Lett.*, 123:154501, 2019.

Rapaport, D. C. *The Art of Molecular Dynamics Simulation*. Cambridge University Press, 2 edition, 2004.

Ristenpart, W. D., McCalla, P. M., Roy, R. V., and Stone, H. A. Coalescence of spreading droplets on a wettable substrate. *Phys. Rev. Lett.*, 97:064501, 2006.

Ristenpart, W. D., Bird, J. C., Belmonte, a., Dollar, F., and Stone, H. A. Non-coalescence of oppositely charged drops. *Nature*, 461(7262):377–380, 2009.

Rose, J. W. Dropwise condensation theory and experiment: A review. *Proc. Inst. Mech. Eng. A*, 216(2):115–128, 2002.

Rose, J. On the mechanism of dropwise condensation. *Int. J. Heat Mass Transf.*, 10(6):755 – 762, 1967.

Rowlinson, J. S. and Widom, B. *Molecular Theory of Capillarity*. Clarendon Press, Oxford, 1982.

Schlesinger, D., Wikfeldt, K. T., Skinner, L. B., Benmore, C. J., Nilsson, A., and Pettersson, L. G. M. The temperature dependence of intermediate range oxygen-oxygen correlations in liquid water. *J. Chem. Phys.*, 145(8):084503, 2016.

Sheng, Q., Sun, J., Wang, W., Wang, H. S., and Bailey, C. G. How solid surface free energy determines coalescence-induced nanodroplet jumping: A molecular dynamics investigation. *J. Appl. Phys.*, 122(24):245301, 2017.

Shikhmurzaev, Y. The moving contact line on a smooth solid surface. *Int. J. Multiph. Flow*, 19 (4):589 – 610, 1993.

Shikhmurzaev, Y. D. Moving contact lines in liquid/liquid/solid systems. *J. Fluid Mech.*, 334: 211–249, 1997.

Sides, S. W., Grest, G. S., and Lacasse, M.-D. Capillary waves at liquid-vapor interfaces: A molecular dynamics simulation. *Phys. Rev. E*, 60:6708–6713, 1999.

Simpkins, P. and Kuck, V. On air entrainment in coatings. *J. Colloid Interface Sci.*, 263(2):562 – 571, 2003.

Sprittles, J. E. and Shikhmurzaev, Y. D. Coalescence of liquid drops: Different models versus experiment. *Phys. Fluids*, 24(12):122105, 2012.

Sprittles, J. E. and Shikhmurzaev, Y. D. A parametric study of the coalescence of liquid drops in a viscous gas. *J. Fluid Mech.*, 753:279–306, 2014a.

Sprittles, J. E. and Shikhmurzaev, Y. D. Dynamics of liquid drops coalescing in the inertial regime. *Phys. Rev. E*, 89:063008, 2014b.

Sprittles, J. E. and Shikhmurzaev, Y. D. The coalescence of liquid drops in a viscous fluid: interface formation model. *J. Fluid Mech.*, 751:480–499, 2014c.

Thompson, P. A. and Robbins, M. O. Simulations of contact-line motion: Slip and the dynamic contact angle. *Phys. Rev. Lett.*, 63:766–769, 1989.

Thoroddsen, S. T. and Takehara, K. The coalescence cascade of a drop. *Phys. Fluids*, 12(6): 1265–1267, 2000.

Thoroddsen, S. T., Takehara, K., and Etoh, T. G. The coalescence speed of a pendent and a sessile drop. *J. Fluid Mech.*, 527:85–114, 2005.

v. Smoluchowski, M. Molekular-kinetische theorie der opaleszenz von gasen im kritischen zustande, sowie einiger verwandter erscheinungen. *Ann. Phys. (Leipzig)*, 330(2):205–226, 1908.

Vahabi, H., Wang, W., Mabry, J. M., and Kota, A. K. Coalescence-induced jumping of droplets on superomniphobic surfaces with macrotexture. *Sci. Adv.*, 4(11), 2018.

Vakarelski, I. U., Chan, D. Y. C., Nonoguchi, T., Shinto, H., and Higashitani, K. Assembly of gold nanoparticles into microwire networks induced by drying liquid bridges. *Phys. Rev. Lett.*, 102:058303, 2009.

Vakarelski, I. U., Manica, R., Tang, X., O'Shea, S. J., Stevens, G. W., Grieser, F., Dagastine, R. R., and Chan, D. Y. C. Dynamic interactions between microbubbles in water. *Proc. Natl. Acad. Sci. U. S. A.*, 107(25):11177–11182, 2010.

van Casteren, A. and Codd, J. R. Foot morphology and substrate adhesion in the Madagascan hissing cockroach, Gromphadorhina portentosa. *J. Insect Sci.*, 10(1), 2010.

Vega, C. and de Miguel, E. Surface tension of the most popular models of water by using the test-area simulation method. *J. Chem. Phys.*, 126(15):154707, 2007.

Voinov, O. V. Hydrodynamics of wetting. *Fluid Dyn.*, 11(5):714–721, 1977.

Vrij, A. Possible mechanism for the spontaneous rupture of thin, free liquid films. *Discuss. Faraday Soc.*, 42:23–33, 1966.

Vrij, A. and Overbeek, J. T. G. Rupture of thin liquid films due to spontaneous fluctuations in thickness. *J. Am. Chem. Soc*, 90(12):3074–3078, 1968.

Wang, F.-C., Yang, F., and Zhao, Y.-P. Size effect on the coalescence-induced self-propelled droplet. *Appl. Phys. Lett.*, 98(5):053112, 2011.

Wang, G. J., Damone, A., Benfenati, F., Poesio, P., Beretta, G. P., and Hadjiconstantinou, N. G. Physics of nanoscale immiscible fluid displacement. *Phys. Rev. Fluids*, 4:124203, 2019.

Wang, K., Liang, Q., Jiang, R., Zheng, Y., Lan, Z., and Ma, X. Self-enhancement of droplet jumping velocity: the interaction of liquid bridge and surface texture. *RSC Adv.*, 6:99314–99321, 2016.

Watson, J. A., Cribb, B. W., Hu, H. M., and Watson, G. S. A dual layer hair array of the brown lacewing: Repelling water at different length scales. *Biophys. J.*, 100(4):1149–1155, 2011.

Werner, A., Schmid, F., Müller, M., and Binder, K. "intrinsic" profiles and capillary waves at homopolymer interfaces: A monte carlo study. *Phys. Rev. E*, 59:728–738, 1999.

Winkels, K. G., Weijs, J. H., Eddi, A., and Snoeijer, J. H. Initial spreading of low-viscosity drops on partially wetting surfaces. *Phys. Rev. E*, 85:055301, 2012.

Wisdom, K. M., Watson, J. A., Qu, X., Liu, F., Watson, G. S., and Chen, C.-H. Self-cleaning of superhydrophobic surfaces by self-propelled jumping condensate. *Proc. Natl. Acad. Sci. U. S. A.*, 110(20):7992–7, 2013.

Wu, M., Cubaud, T., and Ho, C.-M. Scaling law in liquid drop coalescence driven by surface tension. *Phys. Fluids*, 16(7):L51–L54, 2004.

Xu, L., Zhu, H., Ozkan, H. E., Bagley, W. E., and Krause, C. R. Droplet evaporation and spread on waxy and hairy leaves associated with type and concentration of adjuvants. *Pest Manag. Sci.*, 67(7):842–851, 2011.

Zhang, J., Borg, M. K., and Reese, J. M. Multiscale simulation of dynamic wetting. *Int. J. Heat Mass Transf.*, 115:886 – 896, 2017.

Zhang, Q., He, M., Chen, J., Wang, J., Song, Y., and Jiang, L. Anti-icing surfaces based on enhanced self-propelled jumping of condensed water microdroplets. *Chem. Commun.*, 49: 4516–4518, 2013.

Zhang, Y., Sprittles, J. E., and Lockerby, D. A. Molecular simulation of thin liquid films: Thermal fluctuations and instability. *Phys. Rev. E*, 100:023108, 2019.

Zhao, C., Sprittles, J. E., and Lockerby, D. A. Revisiting the rayleigh-plateau instability for the nanoscale. *J. Fluid Mech.*, 861:R3, 2019a.

Zhao, C.-L., Zhao, D.-X., Bei, C.-C., Meng, X.-N., Li, S., and Yang, Z.-Z. Seven-site effective pair potential for simulating liquid water. *J. Phys. Chem. B*, 123(21):4594–4603, 2019b.

Zimmerli, U., Gonnet, P. G., Walther, J. H., and Koumoutsakos, P. Curvature induced l-defects in water conduction in carbon nanotubes. *Nano Lett.*, 5(6):1017–1022, 2005.